

https://dspace.org/

Structured light in atmospheric turbulencea guide to its digital implementation tutorial

Cade Peters; Vasilios Cocotos; Andrew Forbes

OPTICAL SOC AMER
https://hdl.handle.net/10539/45636
WOS

Downloaded from a DSpace repository. https://dspace.org/

Advances in Optics and Photonics

Structured light in atmospheric turbulence—a guide to its digital implementation: tutorial

CADE PETERS, VASILIOS COCOTOS, AND ANDREW FORBES*

School of Physics, University of the Witwatersrand, Private Bag 3, Wits 2050, South Africa
**andrew.forbes@wits.ac.za*

Received August 7, 2024; revised January 15, 2025; accepted January 27, 2025; published 12 March 2025

Structured light has gained prominence of late, offering a modern toolkit for controlling all of light's degrees of freedom and facilitating many applications. A highly topical application is the long distance free-space delivery of structured light, essential in classical and quantum communication, remote sensing, and energy transport. Unfortunately atmospheric turbulence tends to distort the structure of light, negating many of the benefits. For this reason, laboratory studies of structured light in simulated atmospheric turbulence are highly desirable in order to study and mitigate these deleterious effects. Here, we outline how to get started with simulating atmospheric turbulence in the laboratory, from single-phase-screen approximations of weak turbulence to experimentally simulating long path strong turbulent conditions. Core to our approach is the use of modern digital tools in the form of digital micro-mirror devices and liquid crystal spatial light modulators, allowing fast, efficient, and realistic conditions to be realized in the laboratory. We show how to create and pass structured light through the simulated medium and outline the toolkit available for fast probing of the medium. We highlight all the potential pitfalls and common errors in this topical field, providing the code to circumvent them for immediate implementation. Finally, we show how the tutorial can be extended to the quantum regime, as well as general studies of complex light in complex media. This tutorial will be beneficial to both a beginner audience wishing to get started, as well as experienced researchers who wish to unravel the nuances of this approach. © 2025 Optica Publishing Group. All rights, including for text and data mining (TDM), Artificial Intelligence (AI) training, and similar technologies, are reserved.

https://doi.org/10.1364/AOP.538883

1. Introduction 115
2. Statistical Model of Turbulence 116
3. Quantifying Atmospheric Turbulence 117
4. Modeling Atmospheric Turbulence 121
   4.1. Phase and Refractive Index Statistics 121
   4.2. Simulating Propagation Through a Turbulence Medium 123

4.3. Modeling a Thick Atmospheric Medium . . . 125
4.4. Determining the Number of Phase Screens . . . 128
5. Generating Turbulence Phase Screens . . . 130
5.1. Fourier Phase Screens . . . 130
5.1a. Subharmonic Sampling . . . 132
5.2. Noll Phase Screens . . . 135
6. Structuring Light with Computer-Generated Holograms . . . 139
6.1. Paraxial Spatial Modes of Light . . . 141
6.2. Divergence and Scaling of Paraxial Beams . . . 142
6.3. Beam Shaping with an LCoS-SLM . . . 143
6.4. Beam Shaping with a DMD . . . 144
7. Experimental Implementation . . . 144
7.1. Fresnel Scaling . . . 146
7.2. Experimental Setup . . . 147
7.3. Experimentally Simulating a Thick Atmospheric Medium . . . 150
8. Time-Varying Turbulence . . . 155
9. Eigenmodes of Atmospheric Turbulence . . . 156
9.1. Mathematically Defining Eigenmodes of Turbulence . . . 157
9.2. Numerical Simulations . . . 159
10. Extension to Other Media and Regimes . . . 162
10.1. General Complex Light in Random Media . . . 162
10.2. Underwater Wireless Optical Communication . . . 164
10.3. Machine Learning . . . 167
10.4. Quantum Implementation . . . 168
11. Discussion and Concluding Remarks . . . 170
Appendix A. Derivation of the Kolmogorov Power Laws . . . 170
Appendix B. Statistics for Random Processes . . . 172
Acknowledgments . . . 174
Disclosures . . . 174
Data availability . . . 174
References . . . 174

Structured light in atmospheric turbulence—a guide to its digital implementation: tutorial

CADE PETERS, VASILIOS COCOTOS, AND ANDREW FORBES

1. INTRODUCTION

Structured light [1] refers to the ability to control light in all its various degrees of freedom, and to harness that control for improved performance in applications by tailoring light for a purpose [2]. Notable examples include seeing smaller and with better resolution in imaging, focusing tighter, larger bandwidths in optical communication, greater security and information capacity in quantum information processing and communication, and metrology beyond simple fringes (see the many excellent reviews [3–8] for more details). Its explosive trajectory has seen the emergence of a large and active community that is pushing the boundaries with structured light.

A highly topical area of interest is free-space optical communication (FSOC), remote sensing, energy transport, and long-distance space-to-ground links, all benefiting from the use of structured light [9]. A particularly well-studied mode is structured light carrying orbital angular momentum (OAM) [10], extending to quantum light [11,12]. The vast majority of studies aim to unravel the impact of atmospheric turbulence on structured light, with modern questions including which modes are stable in the atmosphere and which are not? Is OAM conserved in the atmosphere? What is the effect of atmospheric turbulence on the fidelity of the modal spectrum? How can one correct spatial mode distortions? Can machine learning be used to recognize distorted modes? Consequently, the intersection of structured light and atmospheric turbulence for free-space spatial mode transport is of paramount interest to a very large community, returning in excess of 15,000 published works in just the last few years.

Because real-world atmospheric studies are costly, time consuming, and lack controlled conditions (you cannot turn the atmosphere on and off), few studies with structured light have tackled the problem [13–17], and instead it is instructive to do the bulk of the investigation in the laboratory with experimentally simulated turbulence. Examples of this include structured light passed over physical systems, such as heater plates [18,19] and hot air chambers [20] and even natural convection in water [21]. More recently, the improved performance of digital micro-mirror devices (DMDs) [22,23] and liquid crystal spatial light modulators (SLMs) [24] has opened up the possibility of simulating real-world conditions with very high accuracy, and even at speeds to realistically mimic fast-changing atmospheric conditions. Despite this, the correct implementation of the theory of structured light and that of atmospheric turbulence can be daunting. The pitfalls include missing frequency components of the phase screens, incorrect aberration scaling, incorrect calibration and hologram execution, incorrect Fresnel scaling for long path turbulence, inappropriate turbulence strength for single phase screens, and lack of control of the size of the structured light modes under study.

In this tutorial we unpack how to get started with a modern digital toolkit for experimentally simulating the interaction of structured light in atmospheric turbulence in the laboratory. We begin with the basic theory, outlined in a salient fashion to be at once

both complete and instructive. We go on to show how to immediately use it for the construction of computer-generated holograms that simulate atmospheric conditions, and we show how to test whether the implementation is correct. We cover points seldom outlined in technical works, including how to execute time-varying turbulence and how to include long-path and strong turbulence correctly. Throughout the tutorial we highlight the approach with the use of structured light, and provide the code for all examples shown in the text. This is the review that we wish had existed prior to unpacking this ourselves, and as such we believe it will be useful to both newcomers to the field and experts alike.

2. STATISTICAL MODEL OF TURBULENCE

Understanding the motion of particles in a gas would typically be a calculation in fluid mechanics. In such cases, one would aim to study the Navier–Stokes equations which govern most interactions in fluid flow. The movement of gases in the atmosphere create a highly turbulent medium with parameters that makes these equations famously difficult to solve. To overcome this, Andrey Kolmogorov (in the 1940s) proposed a statistical model for the velocity fluctuations of turbulent flow [25,26] which was later extended to temperature fluctuations by Oboukhov [27] and Corrsin [28]. Kolmogorov's theory makes use of dimensional arguments, along with assumptions of isotropy and homogeneity, to model the cascade of energy in a turbulent medium and determine the analytical form of several statistical quantities related to the turbulent flow [29]. A derivation of these laws is provided in Appendix A. In short, it assumes that the velocity of a particle in a turbulent medium may be treated as a Gaussian random variable, and the various statistical properties of the velocity (and, hence, the Gaussian distribution from which it is sampled) can be derived using these scaling laws and dimensional arguments. One of the most important statistical properties for our purposes is called the structure function $D_v(r)$ and for Kolmogorov's model is given by [30],

$$D_v(r) = \begin{cases} C_v^2 r^{2/3}, & \text{for } L_0 > r > l_0, \\ C_v^2 l_0^{-4/3} r^2, & \text{for } l_0 > r, \end{cases} \tag{2.1}$$

where C_v^2 is known as the velocity structure constant, L_0 is the outer scale and l_0 is the inner scale. The domain of the structure function is simply the spatial coordinate $r \in \{0, \infty\}$ as the assumption of isotropy removes any directional dependence. We see a natural extension of this theory to the temperature fluctuations in the medium [27,28],

$$D_T(r) = \begin{cases} C_T^2 r^{2/3}, & \text{for } L_0 > r > l_0, \\ C_T^2 l_0^{-4/3} r^2, & \text{for } l_0 > r, \end{cases} \tag{2.2}$$

where C_T^2 is known as the temperature structure constant. We know that any temperature change in a medium will alter the optical path length traveled by light through that medium. Consequently, the turbulent temperature fluctuations create perturbations in the refractive index. Pressure fluctuations are in part also responsible for these perturbations, but for optical and near-infrared wavelength these are negligible when compared with the effects of temperature and so can be largely ignored. We cannot apply the Kolmogorov model to the refractive index directly, as Kolmogorov's model assumes the variable of interest is homogeneous, isotropic and has zero mean. We therefore must break up the refractive index into two terms,

$$n(\mathbf{r}) = n_0 + \delta n(\mathbf{r}). \tag{2.3}$$

For air, we may take the mean value of the refractive index to be $n_0 = 1$. It is reasonable to assume that the refractive index fluctuations $\delta n(\mathbf{r})$ satisfy all the necessary conditions

to be used in Kolmogorov's model and can be related to the temperature and pressure fluctuations via [31,32],

$$\delta n(\mathbf{r}) = 77.6 \times 10^{-6}(1 + 7.52 \times 10^{-3}\lambda^{-2})\frac{P(\mathbf{r})}{T(\mathbf{r})}, \tag{2.4}$$

which, for optical and near-infrared wavelengths frequently used in optical communication, simplifies to [32]

$$\delta n(\mathbf{r}) \approx 79 \times 10^{-6}\frac{P(\mathbf{r})}{T(\mathbf{r})}. \tag{2.5}$$

Since we take the pressure fluctuations to be negligible, we immediately see that the refractive index structure function will have the same form as the temperature structure function [32],

$$D_n(r) = \begin{cases} C_n^2 r^{2/3}, & \text{for } L_0 > r > l_0, \\ C_n^2 l_0^{-4/3} r^2, & \text{for } l_0 > r. \end{cases} \tag{2.6}$$

The proportionality constant C_n^2 is called the *refractive index structure constant* and is typically the quoted value when quantifying the strength of atmospheric turbulence. The larger this value, the greater the fluctuations in the refractive index, and the stronger we consider atmospheric turbulence to be. However, C_n^2 is not the most ideal way of characterizing a turbulent channel as there are additional factors that are not taken into account. More holistic ways of quantifying the effects of atmospheric turbulence will be discussed in Section 3. The value for C_n^2 is challenging to measure directly. Its value, and thus the strength of the turbulence, is experimentally measured using a variety of indirect methods [33–35]. From many of these measurements we obtain the temperature structure constant, which may be related to the refractive index structure constant as

$$C_n^2 = \left(79 \times 10^{-6}\frac{P}{T^2}\right)^2 C_T^2, \tag{2.7}$$

where C_T is the same temperature structure constant from Eq. (2.2). In addition to the structure function, there are several other useful statistical quantities for the study of turbulence. Their definitions and relations are given in Appendix B. One that we make use of frequently in this work is known as the *power spectral density* of the refractive index and for the Kolmogorov model is given by [36]

$$\Phi_n(k) = 0.033 C_n^2 \kappa^{-5/3}, \quad \frac{1}{l_0} > \kappa > \frac{1}{L_0}, \tag{2.8}$$

where κ is the one-dimensional wavenumber/spatial frequency. If we look at the power spectral density in three dimensions, κ will be raised to the power of $-11/3$. In most of our calculations from this point onward, we assume to be working in a regime that lies comfortably inside the inner scale l_0 and outer scale L_0. In other words, we let $l_0 \to 0$ and $L_0 \to \infty$. Experimental observation show that this is not always the case, but these assumptions are required to obtain closed-form expressions of later quantities using the Kolmogorov spectrum. If one needs to include effects from the inner and outer scales, alternative models need be used including the Tartarskii, the von Kárman, and modified atmospheric spectrum. [32].

3. QUANTIFYING ATMOSPHERIC TURBULENCE

As mentioned previously, the refractive index structure constant C_n^2 is not the ideal measure for characterizing a turbulent channel. First, it has dimensions of $\mathrm{m}^{-2/3}$ and, therefore, lacks an intuitive physical interpretation. This prompts the introduction of the Fried parameter, r_0. The Fried parameter has dimensions of length and corresponds to

the average distance between two points at which the refractive indices are correlated. For this reason, it is also sometimes called the *atmospheric coherence length*. For a channel with uniform C_n^2 throughout the path length, the Fried parameter is given by [37]

$$r_0 = \left(0.423k^2 \int_0^L C_n^2(z)\,\mathrm{d}z\right)^{-3/5} = \left(0.423C_n^2k^2L\right)^{-3/5}, \tag{3.1}$$

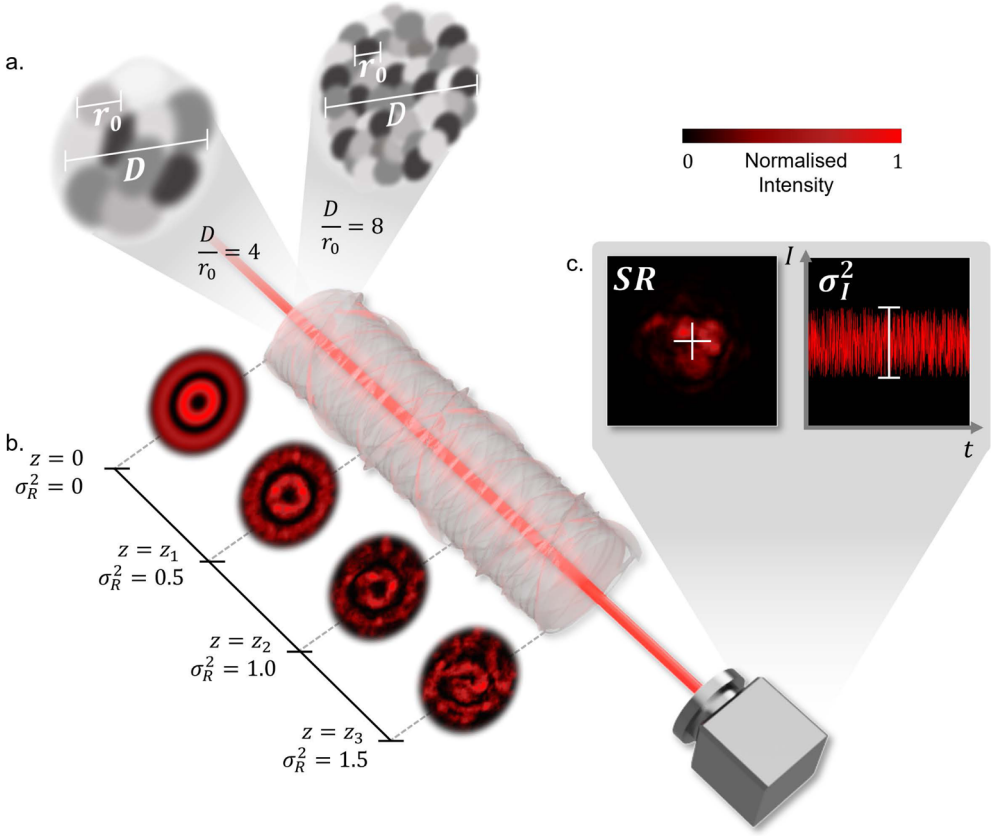
where L is the length of the channel, $k = 2\pi/\lambda$ is the wavenumber, and λ is the wavelength of the light. The assumption that the refractive index structure constant remains unchanged over the propagation path, i.e., $C_n^2(z) = C_n^2$, is valid as long as the speed at which light propagates is much faster than the time taken for distortions along the path to change. Typical turbulent channels have a coherence time of between 10 and 100 ms [38] which is more than sufficient even for paths that are several kilometers long given that the speed of light is approximately 3×10^8 m s^{-1}. A larger value for r_0 corresponds to longer correlation lengths and, thus, less-severe turbulence and weaker distortions. Smaller values of r_0 correspond to points only being correlated over short distances and, thus, more-severe turbulence and stronger induced distortions. While this quantity is more intuitive, it is important to consider it relative to the optical system we wish to characterize. Let us assume our system has an aperture of radius D, on the scale of the size of the optical beam we wish to send through the channel. If the Fried parameter is larger than the aperture of our system, $r_0 > D$, we would not expect there to be considerable induced distortions from the refractive index fluctuations as they will be minimal at this scale. If we have $D > r_0$, we would see that the fluctuations are no longer correlated within our aperture and, thus, we will observe significant distortions in our spatial profile. Consequently, not only is the correlation length of importance when characterizing the optical system, but so is the size of the optical field or beam we wish to send through the system. To deal with these scale considerations and to allow for greater ease of comparison between systems, it is typical to not only quote the Fried parameter, but also the dimensionless quantity D/r_0, which takes these scale issues into consideration. We illustrate this visually in Fig. 1(a), where we see that a channel with larger regions of phase correlation has a larger Fried parameter and, thus, a smaller value for D/r_0 while a channel with smaller correlated regions has a smaller Fried parameter and, thus, a much larger value for D/r_0.

Now that we have a more intuitive way to characterize the refractive index fluctuations in our channel, we should now consider the effects of propagation on our distorted optical field. Let us consider an optical channel with a fixed value for r_0 and D. Since the distortions are induced by the accumulation of a random phase, we see that as the beam propagates further through the channel, the spatial profile becomes increasingly aberrated. Thus, the performance and efficiency of the optical channel depends not only on the severity of the refractive index fluctuations, but also on the distance through which the beam must propagate. The use of parameters such as C_n^2, r_0, or D/r_0 are therefore not always sufficient to quantify the turbulence strength of a particular channel. This prompts the introduction of new metric: the Rytov variance σ_R^2, which is given by [32]

$$\sigma_R^2 = 2.25k^{7/6} \int_0^L C_n^2(z)(L-z)^{5/6}\,\mathrm{d}z = 1.23C_n^2k^{7/6}L^{11/6}. \tag{3.2}$$

It is physically defined as the variance of the log-normal distribution followed by the irradiance fluctuations of a plane wave that have propagated through Kolmogorov turbulence. From Eq. (3.2), we see that both the refractive index structure constant and the propagation path are included in the integrand. Consequently, both the refractive index fluctuations and the accumulated phase distortions from propagation are all

Figure 1



Metrics for turbulence. (a) The Fried parameter r_0 quantifies the strength of the refractive index fluctuations and corresponds to the average correlation length of the phase fluctuations. The smaller the Fried parameter, the stronger the distortion. The strength of the phase aberration is sometimes quoted as a dimensionless quantity relative to the aperture diameter of the channel D/r_0. (b) The effect of turbulence on the beam depends on the phase aberration and the distance propagated by the beam. This is quantified well by the Rytov variance which takes both of these aspects into account. If one measures/calculates the Rytov variance of a beam at different points along a channel, one will see that it increases the further the beam has propagated. (c) The Strehl ratio measures the on-axis intensity of a beam after it has propagated through a channel, typically using a plane wave or Gaussian beam. The scintillation index measures variance of the irradiance fluctuations after propagating through the channel, typically using a Gaussian beam for practical applications.

taken into account when characterizing the channel. A Rytov variance of $\sigma_R^2<1$ is generally considered weak turbulence whereas $\sigma_R^2>1$ would be considered to be in the strong regime. Values of $\sigma_R^2 \approx 1$ would be considered to be of a medium strength. Figure 1(b) illustrates the concept behind the Rytov variance of the channel. If we use the same channel with a constant Fried parameter r_0 and fixed aperture radius D and observe the beam as it propagates, it becomes increasingly distorted. Thus, the distances propagated is just as important when quantifying the distortion of the channel. The effective Rytov variance also increases as one moves through the channel and, thus, acts as the ideal metric to take into account the distortion from the phase aberrations as well as the propagation.

It is important to note that the Rytov variance does not take the aperture/beam size into account while the measure D/r_0 does. No single parameter can capture all the dynamics and relevant statistics of a turbulent channel and one should carefully consider the parameter of choice when simulating or reporting the results of tests or investigations of a turbulent channel. This ensures that an accurate representation of the results is presented and allows for a fair comparison with other systems and methods.

These metrics are all very valuable and allow for fair and robust characterization of a simulated channel. However, these parameters are not easy to obtain experimentally. Additional metrics have been developed which allow for rapid, real-world quantification of the turbulence strength. The first of these we look at is the Strehl ratio, SR. This is defined as the ratio of the average on-axis intensity of the beam through a turbulent channel to the on-axis intensity in the absence of turbulence. If we assume the intensity of our beam is some spatially and temporally varying function $I(x, y, z, t)$ with turbulence and $I_0(x, y, z)$ in the absence of turbulence, we may then express the Strehl ratio as [39],

$$\mathrm{SR} = \frac{\langle I(0,0,L,t)\rangle}{I_0(0,0,L)}, \tag{3.3}$$

where L is the length of the channel and $\langle\cdot\rangle$ represents the time average. In the case of a plane wave propagated to the far-field, we may relate the value of the Strehl ratio to the Fried parameter through the following approximation [32]:

$$\mathrm{SR} \approx \frac{1}{\left[1 + (D/r_0)^{5/3}\right]^{6/5}}. \tag{3.4}$$

Such a parameter is significantly easier to obtain as it can be calculated directly from intensity measurements taken through the channel. In cases where the intensity in the absence of turbulence I_0 is unknown, such as when measuring the turbulence through a real-world free space link or, in general, nonlaboratory environments, we can make use of a parameter known as the scintillation index σ_I^2. This parameter has a different analytical form for different beam types, but is measured the same way for all of them according to [39]

$$\sigma_I^2 = \frac{\langle I^2(0,0,L,t)\rangle - \langle I(0,0,L,t)\rangle^2}{\langle I(0,0,L,t)\rangle^2} = \frac{\langle I^2(0,0,L,t)\rangle}{\langle I(0,0,L,t)\rangle^2} - 1. \tag{3.5}$$

It is normally quoted for a regular Gaussian beam for ease of comparison between different free space links where parameters such as the Rytov variance, Fried parameter, or refractive index structure constant are unknown or difficult to calculate. In the regime of weak turbulence, the scintillation index of a plane wave can be taken to be approximately the same as the Rytov variance, i.e., for a plane wave where $\sigma_R^2 \ll 1$, $\sigma_R^2 \approx \sigma_I^2$. Details and discussion on the scintillation index for weak and strong fluctuations for plane waves and spherical waves can be found in Ref. [40]. Figure 1(c) illustrates the properties of the beam that the Strehl ratio and scintillation index test for. Table 1 provides a summary of the parameters discussed in this section. New studies looking specifically at structured light in turbulence have started to use new parameters, adjusted or adapted to fit the more unique properties of structured light. An example is that of a spatially varying scintillation index, which computes the scintillation index at each pixel in the detector [41]. There is no doubt that as the research into structured light continues, increasingly suitable and unique metrics will be developed to aid in quantifying the effects of different media.

The parameters used to quantify atmospheric turbulence in real-world channels can be determined either from direct measurement of the atmospheric conditions or from optical parameters obtained from probe beams. However, these are not always easy

Table 1. Summary of Turbulence Parameters[a]

Parameter	Symbol	Units	Phase	Propagation	Beam Scale	Easily Measurable
Structure constant	C_n^2	$m^{2/3}$	✓	✗	✗	✗
Fried parameter	r_0	m	✓	✗	✗	✗
Turbulence strength	D/r_0	—	✓	✗	✓	✗
Rytov variance	σ_R^2	—	✓	✓	✗	✗
Strehl ratio	SR	—	✓	✓	✗	✓
Scintillation index	σ_I^2	—	✓	✓	✗	✓

[a]A summary of the parameters used in quantifying atmospheric turbulence showing the parameters units, whether or not it takes into account the phase aberration strength, whether or not it takes into account propagation of the beam through the channel, if it considers the scale of the beam or aperture, and if it is easily measured in experiment.

to obtain. The refractive index structure constant C_n^2 is the easiest to obtain from atmospheric measurements using devices such as sonic anemometers [42,43]. Exact values are highly location specific and can vary greatly depending on factors such as altitude and temperature. Most numerical investigations choose to simulate channels with values between $C_n^2 = 1 \times 10^{-10}$ $m^{2/3}$ to $C_n^2 = 1 \times 10^{-18}$ $m^{2/3}$ [44,45]. The Fried parameter r_0 and turbulence strength D/r_0 have been taken to have values ranging from $D/r_0 = 0.02$ to $D/r_0 = 20$ in a range of numerical investigations, although more typical values range from $D/r_0 = 0.25$ to $D/r_0 = 10$ [46–50]. Tests and simulations that make use of the Rytov variance σ_R^2 have it range from $\sigma_R^2 = 0.1$ to $\sigma_R^2 = 7$ [51,52]. Although most typical short real-world free-space turbulence links (several hundred meters) have a Rytov variance below 1 [15,53].

It is worth noting that to date there has been very little work examining the agreement between numerically simulated turbulence and real-world atmospheric turbulence. This is again due to the difficulty in obtaining all the parameters that might be needed to accurately replicate the exact realization of a free space link. The vast majority of work that has sought to validate the various turbulence models has focused on predicting and measuring the refractive index structure constant C_n^2 based on various environmental parameters with some success [54–56]. Some preliminary studies have examined small artificial turbulence chambers which have showed good agreement between the theoretical and experimental irradiance fluctuations of the beam [57]. There is some work looking at real-world free-space links [58], but this aspect remains relatively unexplored. Examining these comparisons is therefore an open area of research with many unanswered questions that would be valuable for our understanding of light propagation through turbulence.

4. MODELING ATMOSPHERIC TURBULENCE

4.1. Phase and Refractive Index Statistics

With a good understanding of how to quantify turbulence, we can now start to look at some of the statistical principles underlying atmospheric turbulence. We primarily consider optical fields that propagate in the z-axis of our coordinate system. We assume that in this direction, the refractive index fluctuations $\delta n(\mathbf{r})$ are *delta correlated*. This means that we assume the refractive index fluctuations are correlated only in the transverse plane for any fixed value of z. In other words, the fluctuations in the plane (x, y, z_1) are correlated to each other but they are not correlated with any of the points in the plane (x, y, z_2). While this assumption might seem arbitrary at first, we show later that to accurately model the effects of turbulence, we only need to apply the phase aberrations at discrete distances or planes which are all separated by distances much larger that r_0. Consequently, in our practical implementation, the phase perturbation will indeed not be correlated.

We may express this delta-correlated property mathematically using the covariance function $\mathcal{B}_n(\mathbf{r})$ as

$$\mathcal{B}_n(\mathbf{r}_1 - \mathbf{r}_2) = \langle \delta n(\mathbf{r}_1)\delta n(\mathbf{r}_2)\rangle = \delta(z_1 - z_2)A_n(\boldsymbol{\rho}_1 - \boldsymbol{\rho}_2). \tag{4.1}$$

Here $\delta(\cdot)$ is the Dirac delta function, A_n is the two-dimensional covariance function for refractive index and $\boldsymbol{\rho} = (x, y)$ is the spatial coordinate in the transverse plane. This has the physical interpretation of the power spectral density being independent of the spatial frequency in the z-direction, k_z, and so we may set $k_z = 0$. We may then use Eq. (B9) to write

$$\begin{aligned}\mathcal{B}_n(\mathbf{r}_1 - \mathbf{r}_2) &= \int \Phi_n(\boldsymbol{q}, 0)e^{i\mathbf{k}\cdot(\mathbf{r}_1-\mathbf{r}_2)}\mathrm{d}^3\mathbf{k} \\ &= \int e^{ik_z(z_1-z_2)}\mathrm{d}k_z \int \Phi_n(\boldsymbol{q}, 0)e^{i\boldsymbol{q}\cdot(\boldsymbol{\rho}_1-\boldsymbol{\rho}_2)}\mathrm{d}^2\boldsymbol{q} \\ &= 2\pi\delta(z_1 - z_2) \int \Phi_n(\boldsymbol{q}, 0)e^{i\boldsymbol{q}\cdot(\boldsymbol{\rho}_1-\boldsymbol{\rho}_2)}\mathrm{d}^2\mathbf{q}.\end{aligned} \tag{4.2}$$

Comparing this result with Eq. (4.1) allows us to write

$$\begin{aligned}A_n(\mathbf{r}_1 - \mathbf{r}_2) &= 2\pi \int \Phi_n(q)e^{i\boldsymbol{q}\cdot(\boldsymbol{\rho}_1-\boldsymbol{\rho}_2)}\mathrm{d}^2\boldsymbol{q} \\ &= 2\pi \int_0^\infty \mathrm{d}q \int_0^{2\pi} \Phi_n(q)e^{iq\rho\cos(\phi)}q\,\mathrm{d}\phi,\end{aligned} \tag{4.3}$$

where $\boldsymbol{q} = (k_x, k_y)$ is the spatial frequency coordinate in the transverse plane, $q = ||\boldsymbol{q}||$ and $\rho = ||\boldsymbol{\rho}_1 - \boldsymbol{\rho}_2||$. If we compute the angular integral we obtain

$$A_n(\rho) = 4\pi^2 \int_0^\infty q\Phi_n(\nu)J_0(q\rho)\,\mathrm{d}q, \tag{4.4}$$

where $J_0(\cdot)$ is a zeroth-order Bessel function of the first kind.

We now have sufficient information on the statistical properties of the refractive index fluctuations to move onto the statistical properties of the phase perturbations in our complex light field. We need the phase's behavior as the phase is what directly appears in our description of the complex light field. We may relate the phase change of an electromagnetic wave propagating through a medium according to [59]

$$\mathrm{d}\phi = k(n\,\mathrm{d}z + z\,\mathrm{d}n). \tag{4.5}$$

We may therefore describe the total phase gained by the beam $\Theta(\boldsymbol{\rho})$ to the refractive index fluctuations along the propagation path $\delta n(\boldsymbol{\rho}, z)$ as

$$\Theta(\boldsymbol{\rho}) = k\int_{z_1}^{z_2} \delta n(\boldsymbol{\rho}, z)\,\mathrm{d}z. \tag{4.6}$$

This equation allows us to relate the phase perturbations to the refractive index fluctuations of the channel. We can then use it to relate the statistical properties of the refractive index fluctuations to the statistical properties of the phase perturbations which relate directly to our complex light field. The covariance function is given by

$$\begin{aligned}\mathcal{B}_\Theta(\rho) = \langle\Theta(\boldsymbol{\rho}')\Theta(\boldsymbol{\rho}'')\rangle &= k^2 \iint \langle \delta n(\boldsymbol{\rho}', z')\delta n(\boldsymbol{\rho}'', z'')\rangle\,\mathrm{d}z'\,\mathrm{d}z'' \\ &= k^2 \iint \delta(z' - z'')A_n(\rho)\,\mathrm{d}z'\,\mathrm{d}z'' \\ &= zk^2A_n(\rho) \\ &= 2\pi zk^2 \int \Phi_n(q)e^{i\boldsymbol{q}\cdot\boldsymbol{\rho}}\,\mathrm{d}^2\mathbf{q},\end{aligned} \tag{4.7}$$

where we have used Eq. (4.1) in the second line and Eq. (4.4) in the last line and $z = z'' - z'$. The power spectral density of the phase is then

$$\begin{aligned} \mathcal{B}_\Theta(\rho) &= \int \Phi_\Theta(\mathbf{q}) e^{i\mathbf{q}\cdot\boldsymbol{\rho}}\, \mathrm{d}^2\mathbf{q} \\ \Rightarrow \Phi_\Theta(k) &= 2\pi z k^2 \Phi_n(k) \approx 0.49 \frac{k^{-\frac{11}{3}}}{r_0^{\frac{5}{3}}}. \end{aligned} \tag{4.8}$$

From this we can also immediately obtain the structure function for the phase as

$$\mathcal{D}_\Theta(r) = \langle [\Theta(r_0) - \Theta(r)]^2 \rangle \tag{4.9}$$

$$= 2 \int \Phi_\Theta(q) \left[1 - \cos(i\mathbf{q}\cdot\mathbf{r})\right] \mathrm{d}q \approx 6.88 \left(\frac{r}{r_0}\right)^{\frac{5}{3}}. \tag{4.10}$$

The analytical form of the structure function is extremely useful as it is one of the central statistical quantities governing our theory. With it and the power spectral density, we can now accurately model the statistics of atmospheric turbulence.

4.2. Simulating Propagation Through a Turbulence Medium

We now have analytical expressions for the power spectral density and structure function for Kolmogorov turbulence. It now remains for us to find a way to model the propagation of an arbitrary light field through the perturbed media described by the statistics described previously.

We know that the electric field $\mathbf{E}(\mathbf{r}, t)$ behaves as a wave and so must satisfy the wave equation,

$$\nabla^2 \mathbf{E}(\mathbf{r}, t) - \frac{n^2}{c^2} \frac{\partial^2}{\partial t^2} \mathbf{E}(\mathbf{r}, t) = 0, \tag{4.11}$$

where $c = 1/\sqrt{\epsilon_0 \mu_0}$ is the speed of light in a vacuum. If one makes the separation of variables ansatz $\mathbf{E}(\mathbf{r}, t) = \mathbf{U}(\mathbf{r})\,\mathbf{T}(t)$, where we assume the spatial behavior of the electric field can be described separately from its temporal behavior, we then obtain the Helmholtz equation,

$$\nabla^2 U(\boldsymbol{\rho}, z) + k^2 n^2(\boldsymbol{\rho}, z) U(\boldsymbol{\rho}, z) = 0. \tag{4.12}$$

We may then make the paraxial approximation, assuming a nonmagnetic, dielectrically inhomogeneous medium, to obtain

$$2ik \frac{\partial}{\partial z} U(\boldsymbol{\rho}, z) = \nabla_\perp^2 U(\boldsymbol{\rho}, t) + 2k^2 \delta n(\boldsymbol{\rho}, z) U(\boldsymbol{\rho}, z) \tag{4.13}$$

where the refractive index fluctuations are assumed to be small, i.e., $\delta n = (n - 1) \ll 1$. We see that this equation has the form of a two-dimensional time-dependant Schrödinger equation,

$$i\hbar \frac{\partial}{\partial t} \Psi(\boldsymbol{\rho}, t) = \frac{-\hbar}{2m} \nabla_\perp^2 \Psi(\boldsymbol{\rho}, t) + V(\boldsymbol{\rho}, t) \Psi(\boldsymbol{\rho}, t). \tag{4.14}$$

In Eq. (4.14), we have a two-dimensional wave function evolving in time t which experiences a potential given by $V(\boldsymbol{\rho}, t)$. In Eq. (4.13) we have a two-dimensional complex light field evolving in propagation z which experiences an "optical potential" given by $2k^2 \delta n(\boldsymbol{\rho}, z)$. Because of this analogous mathematical structure, it is convenient to borrow the idea of a time evolution operator $e^{-iHt/\hbar}$ from quantum mechanics and apply it to our function $U(\boldsymbol{\rho}, z)$ that is evolving in propagation. By direct comparison

with the two-dimensional time-dependant Schrödinger equation (4.14), we see that the Hamiltonian for the complex light field propagating through the channel is $H = \nabla_\perp^2 + 2k^2\delta n(\mathbf{r})$. The other factors correspond as follows: $\hbar \to 2k$ and $t \to \Delta z$. The propagation evolution operator through a complex medium is then

$$\hat{T}(\Delta z) = e^{-i\left(\Delta z \nabla_\perp^2 + 2k^2 \int_{z_1}^{z_2} \delta n \, \mathrm{d}z\right)/2k} = e^{-i\frac{\Delta z}{2k}\nabla_\perp^2 - i\Theta(\boldsymbol{\rho})} \tag{4.15}$$

$$\text{where } U(\boldsymbol{\rho}, z_2) = \hat{T}(\Delta z) U(\boldsymbol{\rho}, z_1), \tag{4.16}$$

where we have used the phase-refractive index relation from Eq. (4.6). We see from Eq. (4.16) that propagation through a medium with a varying refractive index is a combination of two processes: accumulated, spatially varying phase changes caused by the medium's perturbations and expressed by the operator $2k\Theta(\boldsymbol{\rho})$, and free-space propagation expressed by the operator $\nabla_\perp^2$. In general, it cannot be assumed that these operators commute. However, it has been shown that as long as the refractive index fluctuations δn is an analytic function (i.e., it can be expressed as a Taylor series in z) then we may treat them as commutable with only a small loss in numerical accuracy [60]. This allows us to approximate Eq. (4.16) using a symmetrized split operator [61],

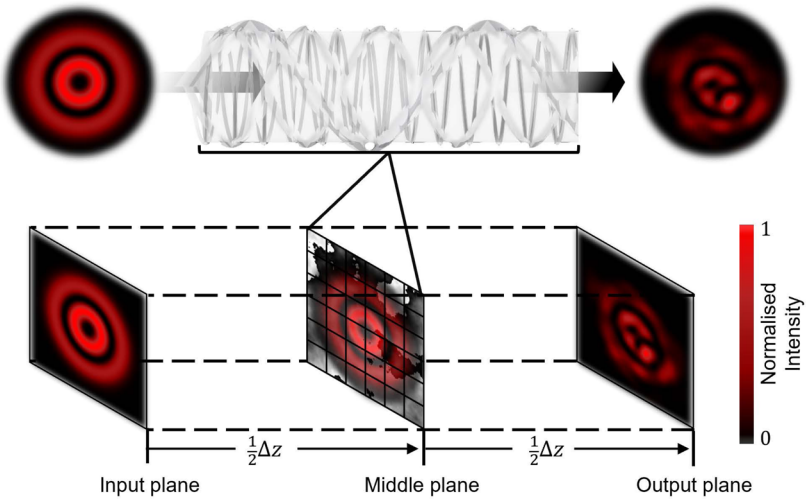
$$\begin{aligned} \hat{T}(\Delta z) = e^{-i\frac{\Delta z}{2k}\nabla_\perp^2 - i\Theta(\boldsymbol{\rho})} &\approx e^{-i\frac{\Delta z}{4k}\nabla_\perp^2} e^{-i\Theta(\boldsymbol{\rho})} e^{-i\frac{\Delta z}{4k}\nabla_\perp^2} \\ &= \hat{P}\left(\frac{1}{2}\Delta z\right) \hat{R}(z_1, z_2) \hat{P}\left(\frac{1}{2}\Delta z\right). \end{aligned} \tag{4.17}$$

We interpret this as approximating the full operator as a combination of three successive operators. The first operator $\hat{P}(\Delta z)$ represents vacuum propagation by a distance Δz. The second operator $\hat{R}(z_1, z_2)$ represents the accumulated phase perturbations obtained during propagation from the plane z_1 to plane z_2. The third is the vacuum propagation operator again. Such an approximation is accurate up to second order and is demonstrated visually in Fig. 2 for a channel of length Δz. In order to replicate a turbulent channel either numerically or experimentally, we therefore begin with some initial complex two-dimensional light field and propagate it a distance $\Delta z/2$. We then add on the accumulated perturbation phase from the entire channel as a single-phase term. This is followed up by propagating the field with this perturbation phase an additional length $\Delta z/2$ to the end of the channel.

In numerical simulation, the propagation steps can be applied through a number of well-known numerical propagation techniques. It is recommended that whatever the technique used, it can be applied to an arbitrary transverse field as we need to propagate the perturbed field in the third step. The most common method is known as *angular spectrum propagation* and detailed discussion and example MATLAB code can be found in Ref. [62]. To apply the refraction operator in numerical simulation, we simply multiply the field by the perturbation phase in the form of a turbulence phase screen; once it has been propagated halfway through the channel. The generation of turbulence phase screens is discussed in Section 5.

In experimental simulations of turbulence, nature takes care of the propagation steps if we simply allow for sufficient space between the light field generation and the detector. The perturbation phase would require an optical element capable of applying a spatially varying phase onto the incoming field. There are several static elements that can do this including turbulence phase plates and specially designed metasurfaces. However, the most flexible approach is a digital one that involves the use of liquid crystal SLMs or DMDs. Such devices are preferable as the programmed phase aberration can be changed on demand by loading a new digital hologram onto the screen. This is in contrast to the static phase of the phase plates and metasurfaces which require manual movement or replacing. The generation of SLM and DMD holograms is discussed

Figure 2



Symmetrized split-step operator. We may numerically (and experimentally) simulate the effects of atmospheric turbulence to a high degree of accuracy by making use of the symmetrized split operator approach. Here we propagate our initial optical field half the distance of the full channel $\frac{1}{2}\Delta z$. This is followed by applying a single phase "screen" to the beam representing the accumulated phase perturbations of the of the entire channel. We then propagate the beam, with this perturbation phase, the remaining length of the channel $\frac{1}{2}\Delta z$.

in Section 7 but also requires information of the perturbation phase in terms of a turbulence phase screen.

4.3. Modeling a Thick Atmospheric Medium

For many turbulent conditions the operator provided in Eq. (4.17) is more than sufficient to model atmospheric turbulence in wave optics simulations or in experiment. However, the operator is derived from the stochastic paraxial Helmholtz equation which assumes that $\delta n \ll 1$. This approximation holds only in weak turbulence ($\sigma_R^2 < 1$) where the phase perturbations are small. In the case of moderate or strong turbulence, the phase fluctuations are much more severe and, thus, the approximation of $\delta n \ll 1$ is no longer true. We thus cannot use the operator in Eq. (4.17) for moderate or strong turbulent channels.

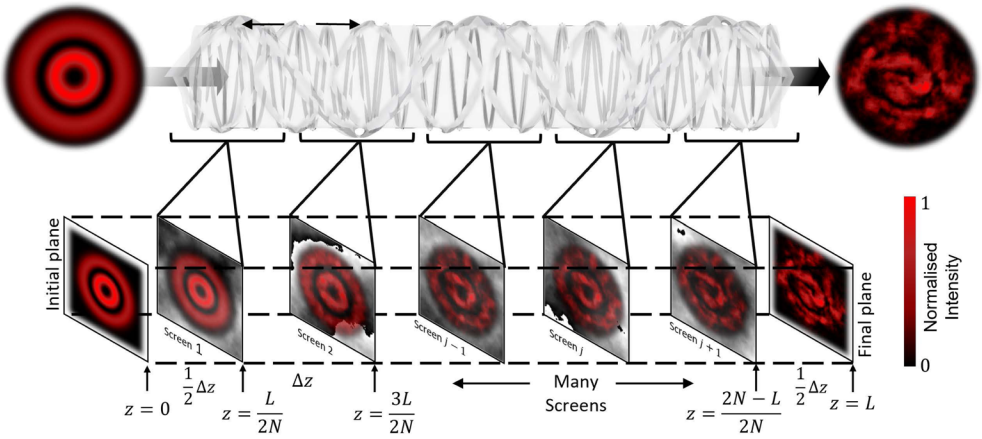
We may still overcome this limitation by making use of the split-step method. In this approach we break up our strong turbulent channel of length L into smaller segments/unit cells of length Δz. The value for Δz is chosen such that for that unit cell of the channel we are in the weak turbulence regime and we may use our operator in Eq. (4.17). We are thus taking the channel operator $\hat{T}_{\text{strong}}(L)$ and breaking it up into a sequence of N operators each representing the action of weak turbulence. We may write this as

$$\hat{T}_{\text{strong}}(L) = \hat{T}_N(\Delta z)\hat{T}_{N-1}(\Delta z)\cdots\hat{T}_2(\Delta z)\hat{T}_1(\Delta z) \quad \text{where } \hat{T}_j(\Delta z) = e^{-i\frac{\Delta z}{4k}\nabla_\perp^2} e^{-i\Theta_j(\boldsymbol{\rho})} e^{-i\frac{\Delta z}{4k}\nabla_\perp^2}. \tag{4.18}$$

We see that the only difference between each of the operators $\hat{T}_j(\Delta z)$ is the spatially varying perturbation phase $\Theta_j(\boldsymbol{\rho})$. We visually show the implementation of these operators in Fig. 3.

As illustrated in Fig. 3, we use our operator as described in Eq. (4.18). We begin with an arbitrary complex light field and propagate it half the distance of a single unit cell. A

Figure 3



Simulating thick media. Some highly aberrated, thick or extended media cannot be accurately simulated with a single symmetrized split operator. In these cases we divide the channel into smaller segments or unit cells. The length of each unit cell is chosen so that, within that segment, the symmetrized split operator is accurate. The input optical field is then exposed to repeated applications of the turbulent phase for that segment and vacuum propagation equal to the length of each unit cell. This is repeated a number of times equal to the number of segments/unit cells.

Algorithm 1. Simulating the propagation of a complex light field through a thick complex channel

Inputs: Initial complex field U, phase aberrations profile for each screen in the channel Θ_j, unit cell spacing Δz.

/* Propagate to first phase screen */

$U = \hat{P}\left(\frac{1}{2}\Delta z\right) U$

/* add phase aberration of first screen */

$U = Ue^{-i\Theta_1}$

/* Remaining unit cell action for each subsequent screen */

for $j = 1$ to N **do**

$U = \hat{P}\,(\Delta z)\, U$ /* propagate to next phase screen */

$U = Ue^{-i\Theta_j}$ /* add phase aberration */

end for

/* Propagate end of last unit cell */

$U = \hat{P}\left(\frac{1}{2}\Delta z\right) U$

Return: U

turbulence phase screen representing the action of the operator $\hat{R}(z_j, z_{j+1})$ is then added. In numerical simulation this would be done through the element-wise multiplication of a phase screen while experimentally this would be done by impinging the field onto the screen of an SLM or DMD with the phase screen hologram programmed onto it. We then propagate the beam the remaining half of the first unit cell plus the first half of the second unit cell (a distance $2 \times \frac{1}{2}\Delta z = \Delta z$) using the angular spectrum propagation technique in numerical simulation or allowing for free-space propagation in the experiment. This process is then repeated N number of times for propagation through the entire channel. For the last unit cell, we only propagate a distance $\frac{1}{2}\Delta z$ after the phase screen. The recipe has been described in Algorithm 1.

Now that we have a rigorous framework with which to simulate atmospheric turbulence both numerically and experimentally, we must now determine how to choose correct

values for the number of segments in our channel (i.e., the value for N) and the severity of the phase aberration at each segment (i.e., the value of r_0 for each turbulence phase screen). To do this, we return to our definitions for the Fried parameter, r_0, and Rytov variance, σ_R^2, in Eqs. (3.1) and (3.2), respectively. Since our method takes a continuous volume of aberrations and breaks it up into a discrete number of phase screens, we must change our integral in Eq. (3.1) into a discrete sum,

$$r_0 = \left(0.423k^2 C_n^2 \sum_{j=1}^{N} \Delta z_j\right)^{-\frac{3}{5}}, \tag{4.19}$$

where we have divided our channel into N segments and assume that our refractive index structure constant is uniform throughout the channel. This is valid as long as we assume our path is horizontal in nature; if not, the structure constant $C_n^2(z)$ must be appropriately adjusted at each step. We assume each segment is of equal length and so $\Delta z_j = \Delta z = L/N$, where L is the total path length. From this, we are able to find the Fried parameters for each of the segments $r_{0,s}$ (which are needed for generating the individual phase screens),

$$r_{0,s} = \left(0.423k^2 C_n^2 \Delta z\right)^{-\frac{3}{5}}, \tag{4.20}$$

and the Fried parameters for the entire channel r_0 (which is needed to quantify the turbulence strength of the entire channel). These are related, via Eq. (4.19), as follows:

$$\begin{aligned} r_0 &= \left(0.423k^2 C_n^2 \sum_{j=1}^{N} \Delta z\right)^{-\frac{3}{5}} = \left(\sum_{j=1}^{N} 0.423k^2 C_n^2 \Delta z\right)^{-\frac{3}{5}} \\ &= \left(\sum_{j=1}^{N} \left(\left(0.423k^2 C_n^2 \Delta z\right)^{-\frac{3}{5}}\right)^{-\frac{5}{3}}\right)^{-\frac{3}{5}} = \left(\sum_{j=1}^{N} r_{0,s}^{-\frac{5}{3}}\right)^{-\frac{3}{5}} \\ &= \left(N r_{0,s}^{-\frac{5}{3}}\right)^{-\frac{3}{5}} = N^{-\frac{3}{5}} r_{0,s}. \end{aligned} \tag{4.21}$$

One of the implications of Eq. (4.21) is that the Fried parameter of the entire channel is larger than the Fried parameters of each individual segment and screen. To obtain a discretized form of the Rytov variance, we perform a similar procedure and change the integral in Eq. (3.2) into a discrete sum,

$$\sigma_R^2 = 2.25k^{\frac{7}{6}} C_n^2 \sum_{j=1}^{N} (L - z)^{\frac{5}{6}} \Delta z. \tag{4.22}$$

If we position the screens in the center of each of the segments and ensure that each segment is of equal length, we obtain on expression for z_j,

$$z_j = \frac{L}{2N} + \frac{L(j-1)}{N}, \tag{4.23}$$

and, thus, we get the following expression for the discrete Rytov variance:

$$\sigma_R^2 = 2.25k^{\frac{7}{6}} C_n^2 L^{\frac{5}{6}} \sum_{j=1}^{N} \left[1 - \frac{1}{N}\left(j - \frac{1}{2}\right)\right]^{\frac{5}{6}} \Delta z. \tag{4.24}$$

Since we define the power spectral density of our phase screens in terms of the Fried parameter, it is useful to also express our Rytov variance in terms of the Fried

parameter of each segment so that we can more easily see the link between the two. This relationship is obtained by combining Eqs. (4.20) and (4.24) to obtain

$$\sigma_R^2 = 5.32k^{-\frac{5}{6}}L^{\frac{5}{6}}r_0^{-\frac{5}{3}}\sum_{j=1}^{N}\left[1-\frac{1}{N}\left(j-\frac{1}{2}\right)\right]^{\frac{5}{6}} = \sum_{j=1}^{N}\sigma_{R,j}^2. \tag{4.25}$$

4.4. Determining the Number of Phase Screens

A very important question to ask is how many phase screens are sufficient to accurately model the channel one is trying to simulate. Over the years, many criteria have been suggested, all of which relate to the assumption of being in the weak turbulence regime. As discussed previously, a single phase screen can only accurately model weakly aberrating channels and cannot accurately replicate the distortion induced by moderate or strong turbulence. We therefore need to choose the number of phase screens in the simulation or experiment such that each unit cell imparts the equivalent of a weak aberration while the cumulative affect of all the unit cells together imparts the desired aberration of the full channel. To enforce this weak distortion condition, initial models set a criterion requiring that the scintillation induced by a single unit cell cannot be greater than 10% of the total scintillation of the channel, i.e., $\sigma_{R,j}^2<0.1\sigma_{R,j}^2$ [63–66] while others have placed restrictions on a quantity called the log-amplitude variance (usually denoted by σ_χ^2) for which the log-amplitude variance $\sigma_{\chi,j}^2$ for a unit cell cannot be more than 20% of the total log-amplitude variance σ_χ^2 for the channel [67]. While these approaches work well as they ensure that no single screen is primarily responsible for the aberration induced by the channel, they do not directly ensure that each screen induces only a weak perturbation. This is because if the total scintillation is very high, even 10% of that scintillation might still fall outside of the weak regime. A more rigorous way of ensure only weak scintillation within each unit cell is to place restrictions on one of the quantities that describe the turbulence strength of the unit cell, independent of the total channel strength. This has been done by placing restrictions on the scintillation index of the unit cell $\sigma_{I,j}^2$ [68] and on the Rytov variance of the unit cell $\sigma_{R,j}^2$ [52,69,70]. These two quantities are similar in a lot of cases and so the criteria are equivalent. From a theoretical viewpoint however, more complex beam shapes (including even the fundamental Gaussian beam) mean that the scintillation index σ_I^2 alone is not sufficient to indicate weak scintillation and additional parameters and criteria are required. We therefore use the Rytov variance σ_R^2 to set our criteria, as it is always defined for a plane wave and has the most straightforward analytical expression.

In order to set our maximum threshold for the Rytov variance, we make use of some concepts from the Rytov approximation theory of atmospheric turbulence. A very thorough explanation of this theory can be found in Ref. [36]. To summarize, the Rytov approximation assumes only weak perturbations to the field such that the refractive index profile of the volume is given by $n^2(\mathbf{r}) \approx 1 + 2\delta n(\mathbf{r})$ so that Eq. (4.12) becomes

$$\nabla^2 U(\mathbf{r}) + k^2 U(\mathbf{r}) = 2\delta n(\mathbf{r})k^2 U(\mathbf{r}). \tag{4.26}$$

We then assume that the solution to this equation takes the form

$$U(\mathbf{r}) = U_0(\boldsymbol{\rho}, z)e^{\psi(\boldsymbol{\rho},z)}, \tag{4.27}$$

where $U_0(\boldsymbol{\rho}, z)$ is the unperturbed field, $\psi(\boldsymbol{\rho}, z)$ is the three-dimensional complex perturbation to the unperturbed field due to the refractive index variations in the medium, $\boldsymbol{\rho} = (x, y)$ is the transverse position vector, and z is the longitudinal position. Using this theory, which assumes weak, phase only fluctuations to the field, one finds

that irradiance fluctuations induced by the medium on a plane wave have a log-normal distribution [71]. The variance of this distribution depends on the strengths of the scintillation of the channel and is called the Rytov variance, σ_R^2. This theory is also what allows us to approximate the Rytov variance σ_R^2 to the scintillation index σ_I^2 in the weak fluctuation regime. We can test this approximation numerically or experimentally by using our single-phase-screen approach as seen in Fig. 4(a) by propagating a plane wave (or a suitable approximation thereof) through our simulated channel. The value of the Rytov variance σ_R^2 at which this approximation breaks down will be our threshold for the weak scintillation regime with a single screen. Simulated results for this test are shown in Fig. 4(b) for encoded Rytov variances ranging from $\sigma_R^2 = 0$ to $\sigma_R^2 = 2$. We see that the approximation holds until just after $\sigma_R^2 = 1$. Thus, for any channel with Rytov variance that satisfies $\sigma_R^2 < 1$, we can consider it to be in the weak scintillation regime and model it using only one phase screen.

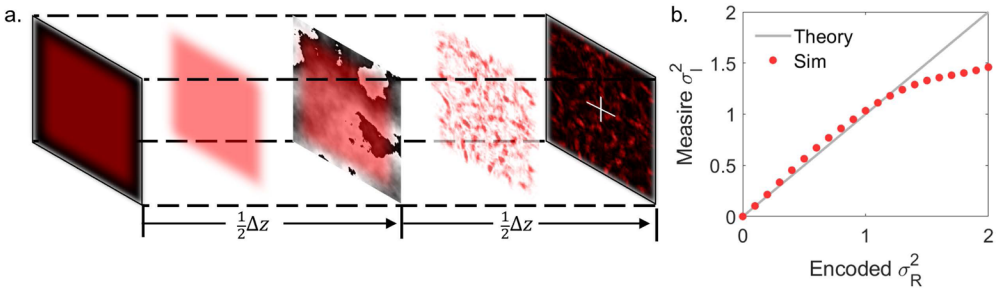
Enforcing the threshold is straightforward due to the structure of Eq. (4.25). The Rytov variance decreases as we move through one segment to the next. This implies that the closer the phase screen is to the source of the light field, the greater its contribution to the distortion of the beam at the receiver. This makes intuitive sense as the phase aberrations in earlier screens along the path will have significantly more propagation distance to manifest themselves as phase and amplitude perturbations when compared with aberrations introduced later in the propagation path. Thus, to ensure each unit cell remains in the weak turbulence regime and meets our imposed threshold of $\sigma_R^2 < 1$, we simply need to enforce the condition that the Rytov variance of the first segment $j = 1$ meets this criteria, i.e.,

$$\sigma_{R,1}^2 = 5.32 k^{-\frac{5}{6}} L^{\frac{5}{6}} r_0^{-\frac{5}{3}} \left[1 - \frac{1}{N}\left(\frac{1}{2}\right)\right]^{\frac{5}{6}} < 1. \tag{4.28}$$

We may now model a channel of any strength σ_R^2 (weak, medium, or strong) and any distance L by simply selecting an appropriate number of segments N and the appropriate Fried parameter for the phase screen in each segment, $r_{0,s}$ such that the inequality in Eq. (4.28) is satisfied. It is important to note that $\sigma_R^2 = 1$ is the maximum we wish to set for each unit cell, but the threshold can be lowered to any value below that and the approach will still be valid. This is useful if one wishes to use the same experimental setup to simulate different turbulence strengths.

It is instructive to look at a typical example of deciding what parameters to use in an experiment. Since the Fried parameter r_0 is normally the easiest and least restrictive parameter to set due to the use of digital holograms, it can be our free parameter, to be solved for given the desired Rytov variance of the channel and other laboratory parameters. Let us suppose one wishes to simulate three different turbulence strengths $\sigma_R^2 = 0.5$, 1.0, and 1.5 using a He–Ne laser (wavelength $\lambda = 633 \times 10^{-9}$ nm) and a total path length of 3 m. One then performs an iterative procedure to find the number of screens needed and the Fried parameter for the screens $r_{0,s}$. We begin by setting the Rytov variance threshold for each unit cell $\sigma_{R,\text{thresh}}^2$ and calculating the Fried parameter for each screen $r_{0,s}$ (given by Eq. (4.20)), the Rytov variance of the first screen $\sigma_{R,1}^2$, (given by Eq. (4.28)), and the Rytov variance of the channel σ_R^2 (given by Eq. (4.25)). If these parameters do meet our desired values, we then go with $N = 1$ screen and use the calculated Fried parameter. If not, then we increase the number of screens to $N = 2$ and repeat the calculation and check if the new values meet our criteria. This process is repeated, each time increasing the number of screens, until the desired criteria are met. MATLAB code for performing this procedure can be found on the Github page mentioned in Section 12. As a result, we find that with the criteria $\sigma_{R,\text{thresh}}^2 = 0.3$, 0.6, and 0.9 for the three different turbulence strengths $\sigma_R^2 = 0.5$, 1.0, and 1.5, we may use

Figure 4



Weak scintillation regime. (a) To simulate the propagation of a plane wave through a weakly turbulent channel, we begin with a square array of uniform phase and amplitude. This is propagated half the length of the channel, where it is perturbed by a phase screen representing the cumulative phase perturbation of the channel. It is then propagated to the end of the channel, where the on-axis intensity is measured. The on-axis intensity is recorded several times through various iterations of phase screens with different profiles but the same Fried parameters r_0 to calculate the scintillation index σ_I^2. (b) Plot showing the encoded Rytov variance σ_R^2 of the single-phase-screen channel and the measured scintillation index σ_I^2 of the plane wave at the output of the channel. We see that they are approximately equal up until $\sigma_R^2 = 1$. Each data point was calculated using 1000 iterations at the same Fried parameter r_0.

three screens in each case and have a unit cell Fried parameter of $r_{0,s}$ = 0.081, 0.11, and 0.16 mm, respectively.

5. GENERATING TURBULENCE PHASE SCREENS

We now know that we can model the effects of weak atmospheric turbulence ($\sigma_R^2<1$) through the applications of a spatially varying phase perturbation followed by vacuum propagation. Numerically and experimentally, this phase perturbation takes the form of a turbulence phase screen which is an array or grid with the various spatially varying phase retardance values as the elements in the array. We must now find a way to generate these phase arrays/screens so that they correctly produce the statistical effects discussed in Section 2. There are many methods used in the literature to do this. The first method, which we refer to as the Fourier phase screen method, leverages our knowledge of the perturbation's spatial frequency decomposition (the power spectral density) and the discrete Fourier transform to allow for fast and accurate generation of phase screens. The second method, which we call the Noll phase screen method, makes use of the Zernike polynomials. These polynomials form a complete and orthogonal basis over the unit circle, making them ideal to describe many kinds of phase or wavefront aberration.

5.1. Fourier Phase Screens

The Fourier phase screen method requires us to construct our phase screen in the frequency domain, not in the spatial domain [63,72,73]. We discretize the two-dimensional frequency domain into a finite number of evenly spaced spatial frequencies. We then assign each of these frequencies a complex weighting coefficient, c_{nm}, based on the properties of the turbulent channel we wish to simulated. We can then perform an inverse discrete Fourier transform to easily generate our desired phase screen. To correctly perform this procedure, we need to first determine the appropriate spacing between the discrete spatial frequencies we wish to use and how to correctly sample or choose the various complex weighting coefficient c_{nm}.

We begin by noting that any discrete two-dimensional function such as the simulated phase screen, $\Theta(x_p, y_q)$, can be written as a Fourier series expansion

$$\Theta(x_p, y_q) = \sum_n \sum_m c_{nm} e^{2\pi i \left[\frac{np}{N} + \frac{mq}{M}\right]}. \tag{5.1}$$

Here we have the discrete spatial coordinates (x_p, y_q) where p and q index each discrete pixel and have values $p = 1, \ldots, N$ and $q = 1, \ldots, M$. We also define the sample/pixel spacing in the spatial domain to be δx in the horizontal direction and δy in the vertical direction. We therefore have $x_p = p\delta x$ and $y_q = q\delta y$ with the side lengths of our phase screen being $L_x = N\delta x$ and $L_y = M\delta y$ in the horizontal and vertical directions, respectively. From Eq. (5.1), we can easily find the Fourier coefficients to be

$$c_{nm} = \frac{1}{NM} \sum_p \sum_q \Theta(x_p, y_q) e^{-2\pi i \left[\frac{np}{N} + \frac{mq}{M}\right]}. \tag{5.2}$$

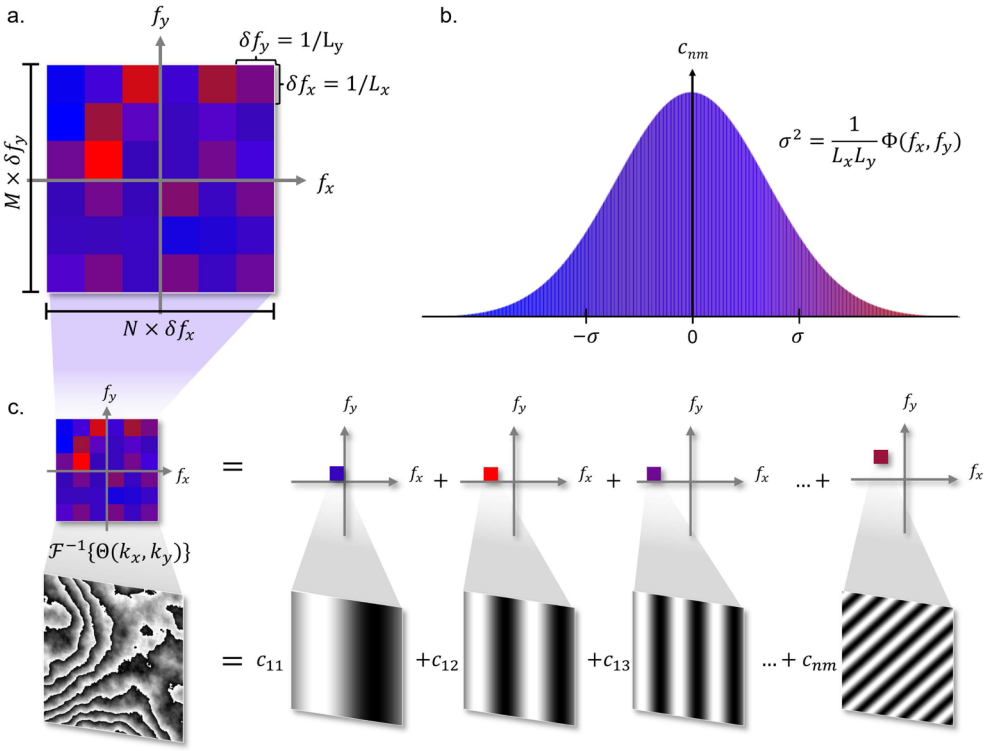
However, based on our previous discussions on the Kolmogorov model, we have no knowledge about individual realizations of turbulence and can only make statements about the statistical properties of the phase screens. In other words, we can currently only make statements about the phase perturbations on average, over many different realizations of atmospheric turbulence. To move from knowledge about the ensemble to knowledge about individual realizations, it is useful to examine how the weighting coefficients vary over all the realizations. One way to do this is to look at the variance of these coefficients, which can be computed as follows:

$$\begin{aligned} \langle |c_{nm}|^2 \rangle &= \frac{1}{N^2M^2} \sum_{pp'} \sum_{qq'} \langle \Theta(x_p, y_q)\Theta(x_{p'}, y_{q'}) \rangle e^{-2\pi i \left[\frac{n(p-p')}{N} + \frac{m(q-q')}{M}\right]} \\ &= \frac{1}{N^2M^2} \sum_{pp'} \sum_{qq'} \mathcal{B}(x_p, y_q) e^{-2\pi i \left[\frac{n(p-p')}{N} + \frac{m(q-q')}{M}\right]} \\ &= \frac{1}{L_xL_y} \Phi(f_{x,n}, f_{y,m}). \end{aligned} \tag{5.3}$$

Here $f_{x,n}$ and $f_{y,m}$ are the discrete spatial frequencies in the horizontal and vertical directions, respectively. We see from the previous description that the variance of the Fourier weighting coefficients $\langle |c_{nm}|^2 \rangle$ is directly related to the power spectral density of our phase screen. Equation (4.8) gives us an analytical expression for the Kolmogorov power spectral density. This tells us that to determine the weighting coefficients for a given realization of turbulence, we sample each value of c_{nm} from a normal distribution with mean 0 and variance $\sigma^2 = \Phi(f_{x,n}, k_{f,m})/(L_xL_y)$.

The process for generating Fourier phase screens is shown visually in Fig. 5. We begin by defining a grid/array which will represent the discrete coordinates in the Fourier/frequency domain, as shown in Fig. 5(a). The pixel size and side lengths for this grid will be $\delta f_x = 1/L_x$ and $N\delta f_x$ and $\delta f_y = 1/L_y$ and $M\delta f_y$ in the horizontal and vertical directions, respectively. Here, $N \times M$ is the resolution of the phase screen in the spatial domain we wish to generate. Each pixel in this array represents the complex weighting coefficient c_{nm} for each spatial frequency. The real and imaginary values for each c_{nm} and, thus, for each element in our array/grid can then be sampled from a normal distribution with mean 0 and variance $\sigma^2 = \Phi(f_{x,n}, k_{f,m})/(L_xL_y)$ as shown in Fig. 5(b) Such sampling can be done using the `randn()` function in MATLAB or the `numpy.random.randn` function in Python. We may finally perform an inverse Fourier transform (or inverse discrete Fourier transform since we are working with arrays) to obtain our turbulence phase screen in the spatial domain. This is shown in Fig. 5(c). This inverse Fourier transform effectively sums each of the spatial

Figure 5



Generating Fourier phase screens. (a) We begin by defining a grid/array with pixel sizes δf_x and δf_x and side lengths $N\delta f_x$ and $M\delta f_y$. (b) Each element of this array is a complex number whose real and imaginary parts are sampled from a normal distribution with a variance proportional to the power spectral density $\Phi(f_{x,n}, k_{f,m})$ and inversely proportional to the side lengths of the desired phase screen in real space $L_x L_y$. (c) An inverse discrete Fourier transform is performed on this grid to obtain the turbulence phase screen in the spatial domain. The inverse Fourier transform effectively sums all the weighted contributions of each spatial frequency in our Fourier domain to form the turbulence phase screen.

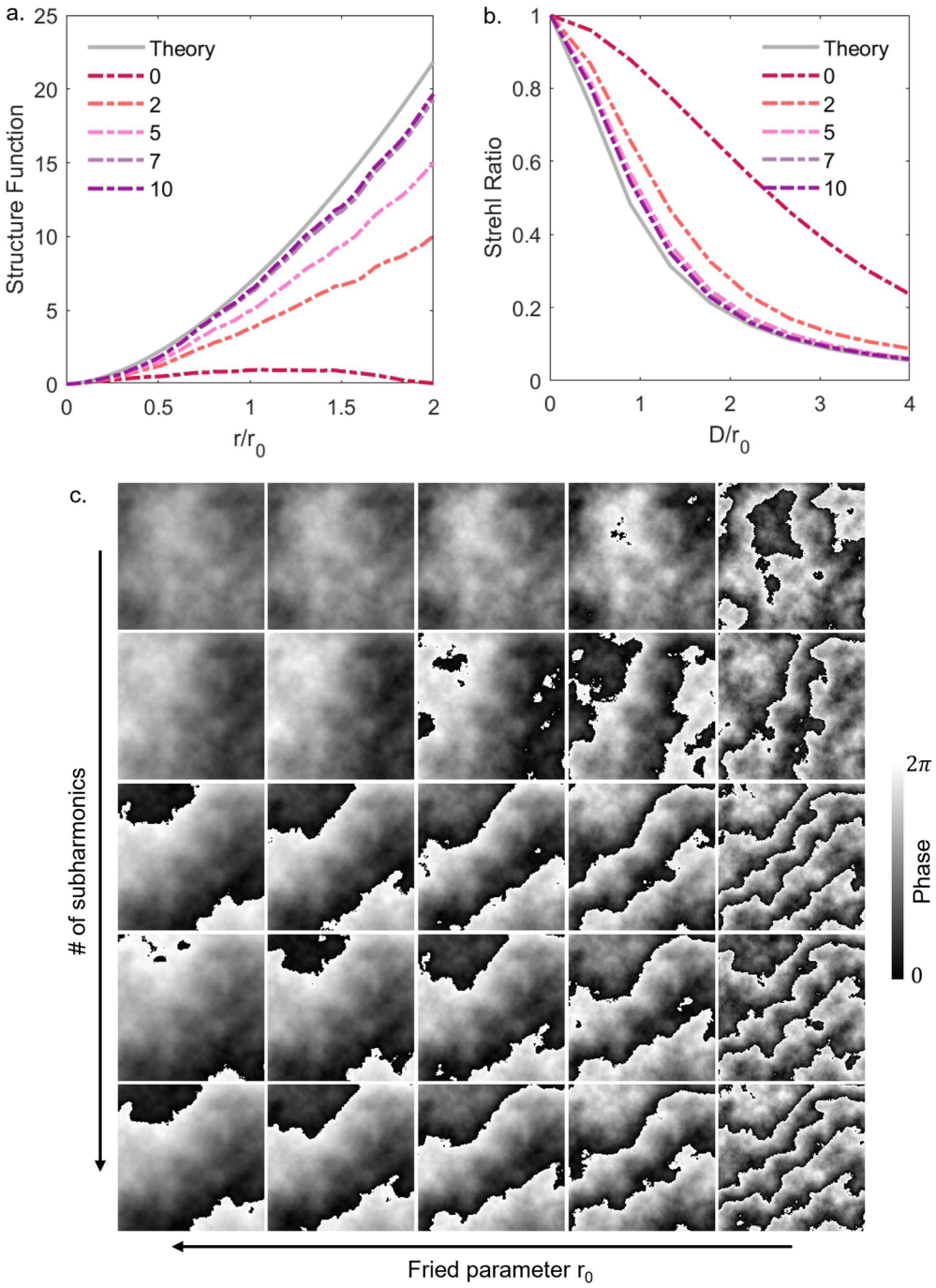
frequencies in our Fourier domain, weighted by their respective coefficient c_{nm}, to form our turbulence phase screen.

We may determine the accuracy of these phase screens in two ways: by directly calculating the structure function of the screens according to Eq. (4.9) and comparing it with Eq. (4.10) or by calculating the Strehl ratio in wave optics simulations with the screens according to Eq. (3.3) and comparing it with Eq. (3.4). The results of both these tests are shown in Figs. 6(a) and 6(b), respectively, for the 0 subharmonic case. We clearly see that for both tests, the results differ greatly from the theoretically predicted values. This can be explained by looking specifically at Fig. 6(a) and observing that the simulated value increasingly differs for longer range correlations. This means that our method of sampling spatial frequencies does not sample frequencies with sufficiently long wavelengths. To overcome this, we implement the method of subharmonics which is explained in the next section.

5.1a. Subharmonic Sampling

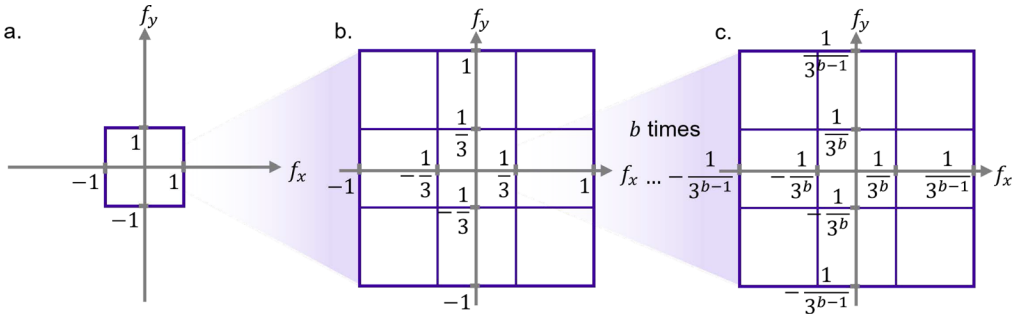
We have now discussed a well-known method of naïvely producing a turbulence phase screen using Fourier transforms. However, these screens fall short in accurately reproducing our known analytical results for atmospheric turbulence. To understand

Figure 6



Fourier phase screens. (a) The numerically calculated structure function $D_\Phi(r)$ of Fourier phase screens calculated for $0, 2, 5, 7$, and 10 subharmonics (dashed lines) compared with the analytical expression (solid line). (b) The numerically calculated Strehl ratio SR of plane waves aberrated with Fourier phase screen calculated for $0, 2, 5, 7$, and 10 subharmonics in the far-field (dashed lines) compared with the analytical expression (solid line). (c) A collage of Fourier phase screens with each row showing screens with increasing turbulence strength $D/r_0 = 2, 2.5, 3.3, 5$, and 10. Each screen has the same aperture size of $D = 1$ mm and decreasing values of r_0. The columns indicating an increasing number of subharmonics with the specific subharmonics of $0, 2, 5, 7$, and 10.

Figure 7



Subharmonic sampling. (a) We isolate a square of twice the unit side length around the origin of our phase profile in the Fourier domain. (b) We divide this small square into a 3×3 grid and use these new, small grid squares to sample smaller frequencies. (c) We can repeat this process up to an arbitrary number of subharmonics where the sizes of the grids are determined through the shown dimensions, where b is the subharmonic we are sampling.

why, we consider the form of our energy spectrum/power spectral density given by Eq. (2.8). Here, the wavenumber is raised to the power of $-11/3$. Thus, very low frequencies will have a significant contribution to the overall field. The smallest frequencies sample by our method are given by the reciprocal of our field's size in real space: $\delta f_{x,n} = 1/L_x$ and $\delta f_{y,m} = 1/L_y$. To ensure frequencies smaller than these are included in the spectrum, we employ a technique known as subharmonic sampling [72,74,75].

We begin by focusing on the region of twice the unit side length around the origin in the Fourier domain (as it contains information on the lowest frequencies) and divide it into a three-by-three grid. The sides of the central grid square are therefore located a distance of $1/3$ of the units from the origin. Figures 7(a) and 7(b) illustrate this visually. This new, smaller grid gives us access to what is called the first *subharmonic* and allows us to sample smaller frequencies and consequently more accurately construct the phase screen using the method described in the previous section. We can repeat this process, each time using the central square from the previous subharmonic to sample decreasingly lower frequencies and obtain an ever more accurate phase screen reconstruction. It is important to note that since these subharmonic grids consist of pixels that are smaller than the pixels used to sample the higher frequencies (by a factor of $1/3$ for each subharmonic), we must adjust the amplitudes of the subharmonic terms (i.e., the c_{nm} terms) by a factor of $(1/3)^b$, where b is the number of the subharmonic. We can express this subharmonic sampling as

$$\Theta_{\text{sub}}(x_p, y_q) = \sum_b \sum_n \sum_m c_{nm} e^{2\pi i \left[\frac{np}{3^b N} + \frac{mq}{3^b M}\right]}. \tag{5.4}$$

Here, the term with $n = m = 0$ is not summed over. The coefficients for the subharmonic grid are sample from a Gaussian distribution with mean zero and variance of

$$\sigma^2 = \left(\frac{1}{3^b}\right)^2 \frac{\Phi(k_n, l_m)}{L_x L_y}. \tag{5.5}$$

Once these subharmonic terms have been calculated, they can be added to the naïvely computed phase screen with only the high frequencies from our naïve approach in the

previous section. Thus, our total phase screen is given by

$$\begin{aligned}\Theta(x_p, y_q) &= \Theta_{\text{high}}(x_p, y_q) + \Theta_{\text{sub}}(x_p, y_q) \\ &= \sum_n \sum_m c_{nm} e^{2\pi i\left[\frac{np}{N} + \frac{mq}{M}\right]} + \sum_b \sum_n \sum_m c_{nm} e^{2\pi i\left[\frac{np}{3^b N} + \frac{mq}{3^b M}\right]}.\end{aligned} \tag{5.6}$$

Fourier phase screens with various turbulence strengths and various numbers of subharmonics are shown in Fig. 6(c). We note that the addition of more subharmonics creates more prominent, long-range periodic features as seen by the appearance of phase discontinuity lines spanning the length of the phase screens with larger numbers of subharmonics. We also see that stronger turbulence (characterized by a smaller Fried parameter r_0) results in phase screens with more rapidly changing phase features, corresponding to the more rapid refractive index fluctuation described in Kolmogorov's theory.

One question then remains: what is a suitable number of subharmonics to accurately recreate the effects of atmospheric turbulence? Each additional subharmonic can mean a noticeable increase in computation time when generating phase screens, but also means increased accuracy. It is therefore important to determine the appropriate number of subharmonics to sufficiently replicate the effects of turbulence while also allowing for computational efficiency. To investigate this, we can perform the same two computational tests as before: directly calculating the structure function and Strehl ratios according to Eqs. (3.3) and (4.9), respectively, and comparing the numerical results to the analytical expressions in Eqs. (3.4) and (4.10), respectively. The results are shown in Figs. 6(a) and 6(b) for subharmonics 0, 2, 5, 7, and 10. We see that with the addition of more subharmonics, the closer the numerical results for both the structure function and the Strehl ratio are to the theoretical values, validating our decision to use the subharmonic sampling method for increased accuracy. The structure function shows very little improvement after seven subharmonics whereas the Strehl ratio shows only small improvements after five subharmonics. In this work, we are interested in simulating the effects of atmospheric turbulence on light fields. Since the Strehl ratio uses results from the intensity of the aberrated light fields and is something that can be measured directly in both numerical simulations and in the laboratory, we use its findings as a guide and, unless otherwise stated, generate Fourier phase screens with five subharmonics for the remainder of this work.

5.2. Noll Phase Screens

Another method commonly used to generate turbulence phase screens makes use of Zernike polynomials. Zernike polynomials form a complete and orthogonal basis on the unit circle meaning they can be used to reconstruct virtually any phase perturbation. Each Zernike polynomial is associated with a specific type of aberration. As an example, there exists a Zernike polynomial Z_0^2 which corresponds to the defocus aberration, whereas the polynomial Z_1^1 is related to the tilt experienced by a beam. By using these polynomials to describe atmospheric turbulence, we are effectively decomposing atmospheric turbulence into a superposition of much simpler, well-known aberrations [76,77].

Zernike polynomials Z_n^m are traditionally indexed by two integers, with n primarily indexing the radial component and m indexing the azimuthal coordinate. However, such an indexing scheme makes it challenging to implement the algorithms relevant to Zernike polynomials and, for our purposes, make it challenging to construct a turbulence phase screen. Many alternative methods of indexing and ordering the Zernike polynomials have been developed to get around this. One can use any ordering scheme,

so long as one is consistent and appropriately adapts the procedure for generating turbulent phase screens to their chosen ordering scheme. For the remainder of this work, we will make use of the Noll ordering convention, established by Noll in 1976. The Noll index j of an arbitrary Zernike polynomial Z_n^m can be determined from its indices n and m via [76]

$$j := \frac{n(n+1)}{2} + |m| + \begin{cases} 0, & m>0 \wedge (n \mod 4) \in \{0,1\}, \\ 0, & m<0 \wedge (n \mod 4) \in \{2,3\}, \\ 1, & m \geq 0 \wedge (n \mod 4) \in \{2,3\}, \\ 1, & m \leq 0 \wedge (n \mod 4) \in \{0,1\}. \end{cases} \tag{5.7}$$

The analytical form for the Zernike polynomials is therefore given as follows [78]:

$$\left.\begin{aligned} Z_{\text{even j}}(r,\theta) &= \sqrt{n+1}\, R_n^m(r)\sqrt{2}\cos(m\theta), \\ Z_{\text{odd j}}(r,\theta) &= \sqrt{n+1}\, R_n^m(r)\sqrt{2}\sin(m\theta), \end{aligned}\right\} \quad m \neq 0, \\ Z_{\text{j}}(r,\theta) = \sqrt{n+1}\, R_0^m(r), \qquad m = 0, \tag{5.8}$$

where r is the radial coordinate and θ is the azimuthal coordinate. The radial component is given by

$$R_n^m(r) = \sum_{s=0}^{(n-m)/2} \frac{(-1)^s (n-s)!}{s![(n+m)/2-s]![(n-m)/2-s]!}. \tag{5.9}$$

The first 15 Zernike polynomials are shown in Fig. 8 for reference. Their unique properties of completeness and orthogonality over the unit circle allow us to expand any real, arbitrary function, such as our turbulent phase $\Theta(r,\theta)$, over this domain as a linear superposition of Zernike polynomials,

$$\Theta(r,\theta) = \sum_{j=0}^{\infty} a_j Z_j, \tag{5.10}$$

where j is the Noll index given by Eq. (5.7), Z_j is the Zernike polynomial with Noll index j, and a_j is its associated, real-valued, weighting coefficient. In practice, as we may only use a finite number of Zernike modes in our construction, we must restrict the sum up to some maximum number of modes, N_{max}.

From our previous discussions, one may further expect that the Zernike scaling coefficients a_j can be described as Gaussian random variables with zero mean, and a particular variance related to the turbulence strength and perhaps the particular mode. However, it was shown by Noll that the appearance of Zernike modes in the expansion in Eq. (5.10) and by extension the coefficients a_j are not statistically independent. It was shown that the weighting coefficients have the following covariance [76,77]:

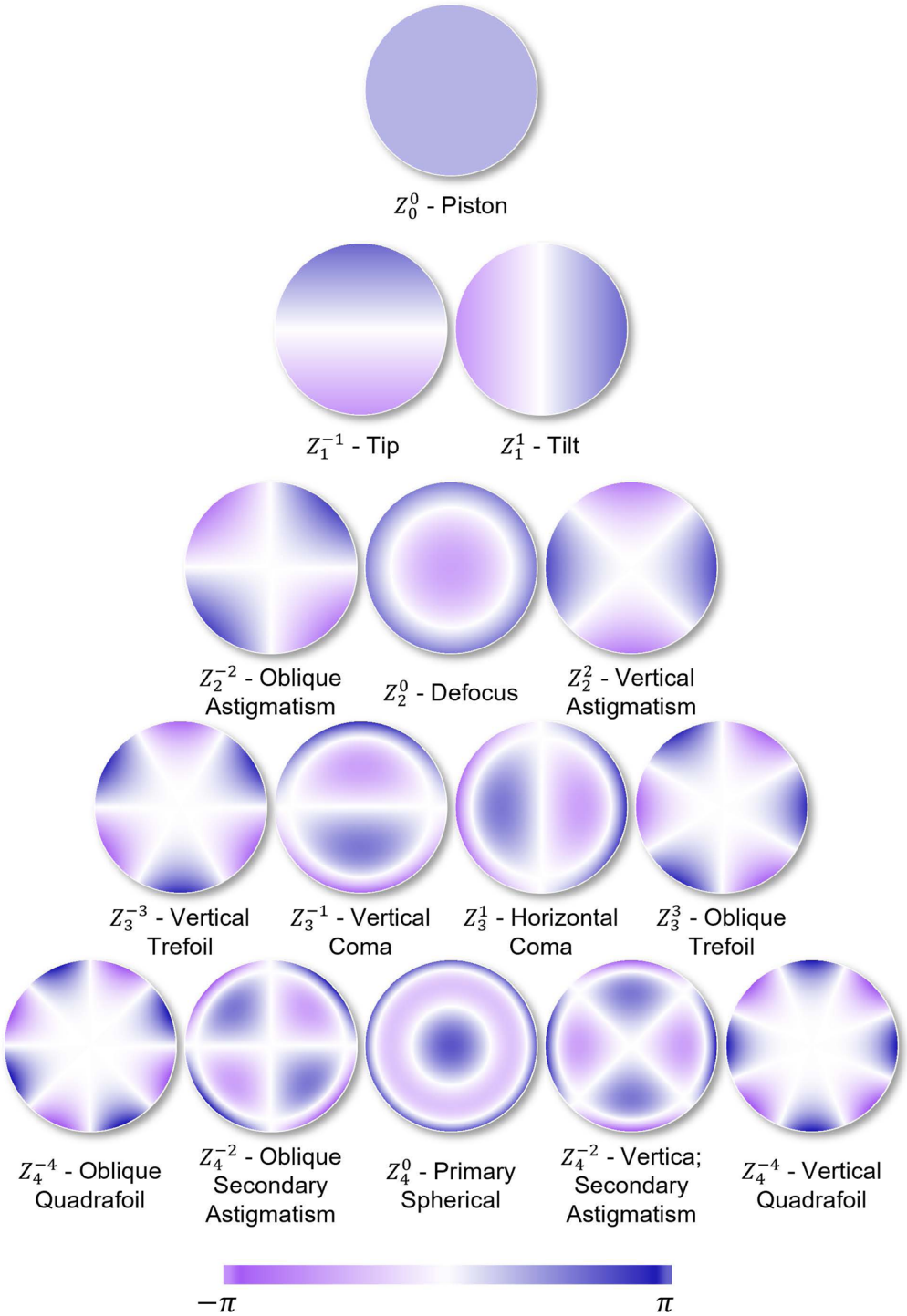
$$\langle a_j a_{j'} | = \rangle \frac{K_{mm'}\delta_{mm'}\Gamma[(n+n'-5/3)/2](D/r_0)^{5/3}}{\Gamma[(n-n'+17/3)/2]\Gamma[(n'-n+17/3)/2]\Gamma[(n+n'+23/3)/2]}, \tag{5.11}$$

where $\delta_{mm'}$ is the Kronecker delta and $K_{mm'}$ is given by

$$K_{nn'} = \frac{\Gamma(14/3)[(24/5)\Gamma(6/5)]^{5/6}[\Gamma(11/6)]^2}{2\pi}(-1)^{(n+n'-2m)/2}\sqrt{(n+1)(n'+1)}. \tag{5.12}$$

We see that this covariance is always 0 for Zernike Modes Z_n^m and $Z_{n'}^{m'}$ if we have $m \neq m'$. We therefore must find a way of relating our set of weighting coefficients a_j to some other set of variables that are statistically independent. To achieve this we

Figure 8



Zernike polynomials. An array of the 15 lowest-order Zernike polynomials and the common optical aberration that they quantify. We see that higher-order Zernike polynomials have more complex and rapidly varying features.

first express the covariance of the weighting coefficients a_j in the form of a covariance matrix as follows:

$$C = \langle \mathbf{A}\mathbf{A}^{\mathrm{T}} \rangle = \begin{bmatrix} \langle a_2 a_2^* \rangle & \cdots & \langle a_2 a_N^* \rangle \\ \vdots & \ddots & \vdots \\ \langle a_N a_2^* \rangle & \cdots & \langle a_N a_N^* \rangle \end{bmatrix}, \quad \text{where } \mathbf{A}^{\mathrm{T}} = [a_2 \; a_3 \; \cdots a_N]. \tag{5.13}$$

We have neglected the Zernike polynomial $Z_1 = Z_0^0$ as we are interested in representing the phase variations and the piston aberrations is simply the addition of a flat global phase. Figure 9(a) shows a plot of the Noll covariance matrix. We can see from its form that while it is a symmetric matrix, there are several off diagonal elements visually indicating that the Zernike weighting coefficients a_j are not independent from each other. We may perform a singular value decomposition (SVD) on C to obtain the following:

$$C = USU^{\dagger}, \tag{5.14}$$

where U is some unitary matrix and S is a matrix that is guaranteed to be diagonal. The Noll covariance matrix C is expressed in the Zernike modal basis. Because S is diagonal, we can interpret the matrices U and $U^{\dagger}$ as mapping our Noll covariance matrix C to and from a basis whose basis elements are linearly and statistically independent. In other words, if we apply the matrix $U^{\dagger}$ onto our weighting coefficients vector $\mathbf{A}$, it will map from the Zernike modal basis to another basis with different elements weighted by coefficients b_j, where each b_j is statistically independent from the others. We therefore have

$$\mathbf{B} = U^{\dagger}\mathbf{A} \quad \Leftrightarrow \quad \mathbf{A} = U\mathbf{B}, \quad \text{where } \mathbf{B}^{\mathrm{T}} = [b_2, \; b_3, \; \cdots b_N], \tag{5.15}$$

and so the covariance matrix of these b_j is

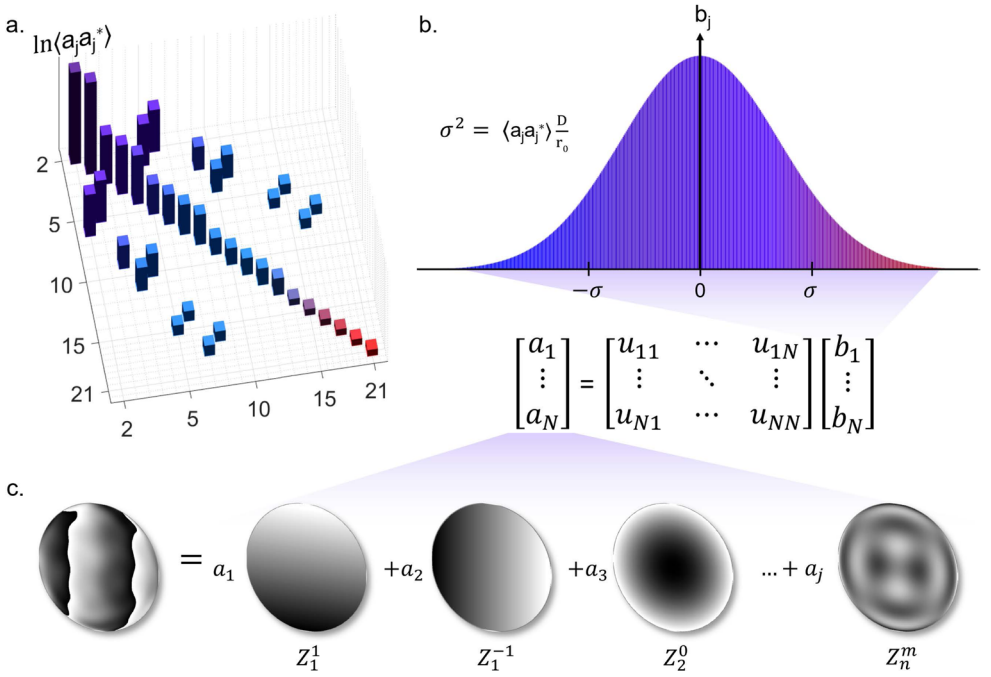
$$\langle \mathbf{B}\mathbf{B}^{\dagger} \rangle = \langle U^{\dagger}\mathbf{A}\mathbf{A}^{\dagger}U \rangle = U^{\dagger}\langle \mathbf{A}\mathbf{A}^{\dagger} \rangle U = U^{\dagger}CU = S. \tag{5.16}$$

Since S must be diagonal, the covariance matrix of the coefficients b_j is diagonal and so each b_j is statistically independent. The coefficients b_j are known as the Karhunen–Loèv coefficients and their variance is the same as the Zernike weighting coefficient a_j [77]. This can be seen in the relation in both Eqs. (5.15) and (5.16). Because they are statistically independent, we may then sample each b_j from a normal distribution of mean 0 and a variance given by the appropriate element of the Noll covariance matrix $\langle a_j a_j^* \rangle$.

Figure 9 shows the process for generating the Noll phase screens. We begin by generating the Noll covariance matrix according to Eq. (5.11) with the appropriate dimensions for the number of Zernike polynomials we wish to include in our decomposition as shown in Fig. 9(a). We then use the diagonal elements of this matrix to define the variance of the Karhunen–Loèv coefficients b_j, which we use to build our vector $\mathbf{B}$ as shown in Fig. 9(b). We then perform an SVD on the Noll covariance matrix C and multiply the unitary matrix U with the vector $\mathbf{B}$ to obtain the vector $\mathbf{A}$ according to Eq. (5.15). We subsequently use the elements of the vector $\mathbf{A}$ as the weighting coefficients for each of our Zernike polynomials. The sum of all of these Zernike polynomials multiplied by their respective weighting coefficient then gives us our turbulence phase screens as shown in Fig. 9(b).

We may determine the accuracy of our Noll phase screens in the same two ways as before: by directly calculating the structure function of the screens according to Eq. (4.9) and comparing it with Eq. (4.10) or by calculating the Strehl ratio in wave optics simulations with the screens according to Eq. (3.3) and comparing it

Figure 9



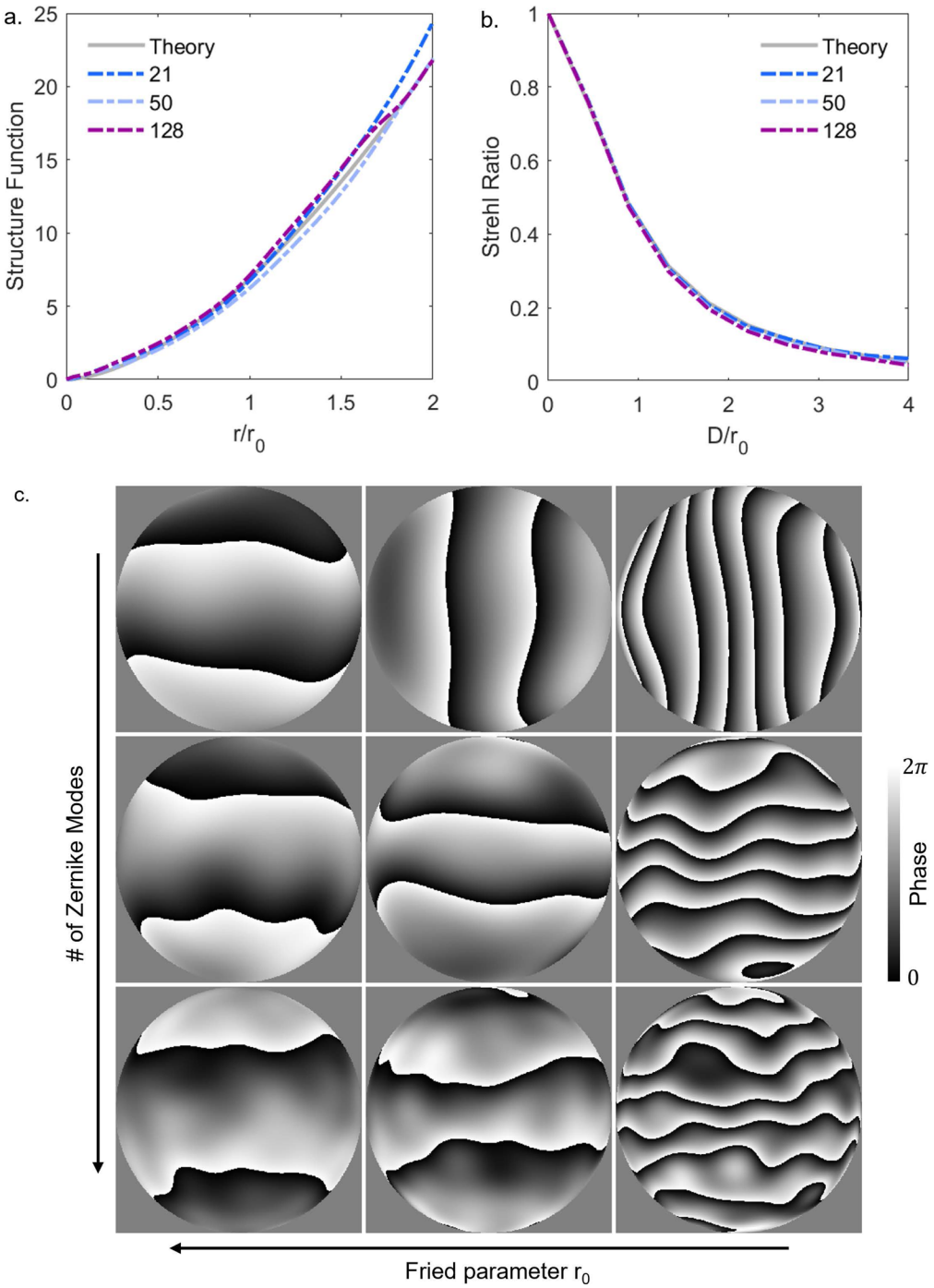
Sampling Noll coefficients. (a) The Noll covariance matrix $C = \langle a_j a_j^* \rangle$ for the first 21 modes according to the Noll ordering convention. (b) The Noll coefficients a_j are determined by first sampling the Karhunen–Loèv coefficients b_j from a normal distribution with mean 0 and variance $\langle a_j a_j^* \rangle$. This vector is multiplied by the unitary matrix U obtained from the SVD of the Noll covariance matrix to obtain the Noll weighting coefficients. (c) The turbulence phase screen is obtained by summing all the Zernike polynomials weighted by their respective Noll coefficient.

with Eq. (3.4). The results of both these tests are shown in Figs. 10(a) and 10(b), respectively, for $N = 21, 50$, and 128 Zernike modes. We see excellent agreement with the theory in both cases. For the Strehl ratio, there is barely any improvement in the measured Strehl ratio. We see slight improvement in the structure function for higher numbers of Zernike modes, especially in the regime of longer-range correlations. Several Zernike phase screens for various turbulence strengths and maximum number of Zernike modes N are shown in Fig. 10(c). We see that for increased turbulence strengths (characterize by a smaller Fried parameter r_0) there are more and more rapid spatial variations in the phase profile. This corresponds with the fact that larger turbulence strengths should have more rapidly varying spatial phase variations. We also see that an increased number of maximum Zernike modes leads to more rapid, smaller, and smoother variations in the phase profile.

6. STRUCTURING LIGHT WITH COMPUTER-GENERATED HOLOGRAMS

Terrestrial and satellite FSOC has become extremely prominent in recent years driven by a need for higher data-transfer rates and the potential to bridge the digital divide in many areas around the world in a manner that is cheap and license free. Here, structured light has begun to shine as methods of mode-division and space-division multiplexing have shown their ability to increase the efficiency and reliability of FSOC systems. As such, it is vital to investigate the effects of atmospheric turbulence on these structured modes to determine their viability and performance for real-world applications. In this section, we give a brief overview of two common forms of spatially structured

Figure 10



Noll phase screens. (a) The numerically calculated structure function $\mathcal{D}_\Theta(r)$ of Noll phase screens calculated for a maximum number of Zernike modes $N = 21, 50$, and 128 (dashed lines) compared with the analytical expression (solid line). (b) The numerically calculated Strehl ratio SR of plane waves aberrated with Noll phase screens calculated for a maximum number of Zernike modes $N = 21$, 50, and 128 in the far-field (dashed lines) compared with the analytical expression (solid line). (c) A collage of Noll phase screens with each row showing screens with increasing turbulence strength $D/r_0 = 2$, 3.3, and 10. Each screen has the same aperture size of $D = 1$ mm and decreasing values of r_0. The columns indicating an increasing number of the maximum number of Zernike modes $N = 21$, 50, and 128.

light: Laguerre–Gaussian (LG) and Hermite–Gaussian (HG) beams. We describe their structure and properties and describe how their scaling should be treated when propagating them over large distances. We then move on to describe how we can generate these beams in a laboratory setting. This is done through the use of either refractive or diffracting holograms which can be used to impart a spatially varying phase and amplitude profile onto an incident beam from a laser source.

6.1. Paraxial Spatial Modes of Light

HG and LG beams are known to be eigenmodes of free space. This means that they are able to propagate through free space (vacuum) without changing their spatial profile. They are solutions to the paraxial Helmholtz equation (4.13) when there are no refractive index fluctuations, i.e., $\delta n(\mathbf{r}) = 0$.

In order to solve the paraxial Helmholtz equation, we have to make some assumptions to simplify our field $U(x, y, z)$. If one assumes the field $U(x, y, z)$ has Cartesian symmetry, it is most convenient to make the following separation of variables ansatz $U(x, y, z) = X(x, z)Y(y, z)$, and so rewrite the paraxial Helmholtz equation as

$$\left(\frac{\partial^2}{\partial x^2} + \frac{\partial^2}{\partial y^2} + 2ik\frac{\partial}{\partial z}\right) U = 0. \tag{6.1}$$

The solutions to Eq. (6.1) are known as HG modes and are given by

$$HG_n^m(x, y, z) = \underbrace{\sqrt{\frac{2^{1-n-m}}{w^2(z)\pi n!m!}}}_{\text{A}} \underbrace{H_n\left(\frac{\sqrt{2}x}{w(z)}\right) H_m\left(\frac{\sqrt{2}y}{w(z)}\right)}_{\text{B}} \underbrace{e^{-\frac{r^2}{w^2(z)}}}_{\text{C}} \underbrace{e^{ik\frac{r^2}{2R(z)}}}_{\text{D}} \underbrace{e^{i(m+n+1)\psi(z)}}_{\text{E}}. \tag{6.2}$$

Factor A is a normalization factor such that $\langle HG_{n'}^{m'} | HG_{n^m} \rangle = 1$ for $n = n'$ and $m = m'$ and is zero otherwise. The beam waist/spot size given by

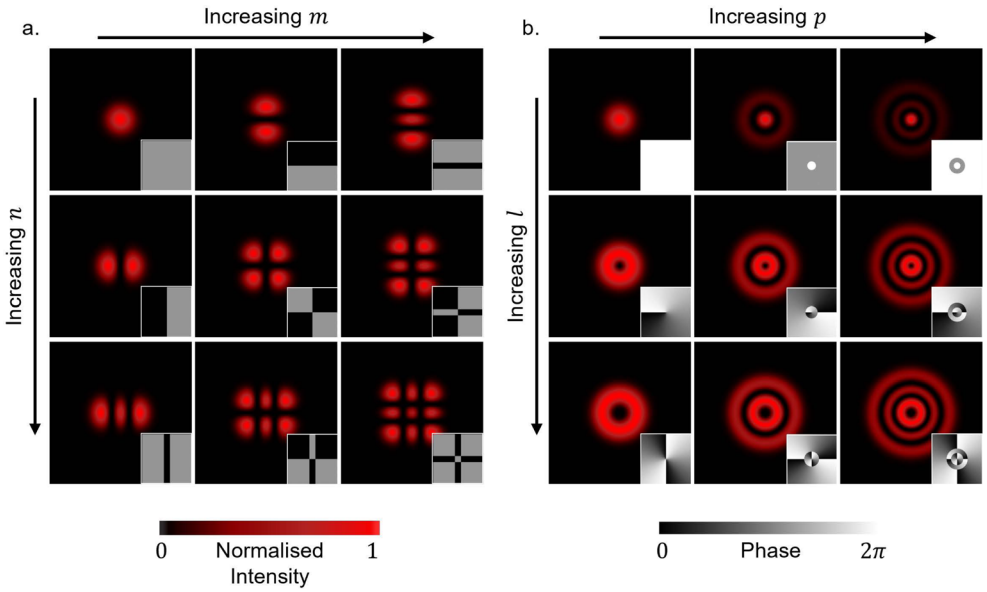
$$w(z) = w_0\sqrt{1 + \left(\frac{z}{z_R}\right)^2}, \tag{6.3}$$

representing the beam waist as a function of propagation distance and $w_0 = w(0)$. The Rayleigh range $z_R = \frac{1}{2}kw_0^2$ is the distance at which the beam area has exactly doubled. The variables n and m represent the horizontal and vertical indices, respectively, and uniquely specify each HG mode. They can be any nonnegative integer and can be interpreted visually as the number of intensity fringes in the x and y directions, respectively. The total mode order is given as $M = m + n + 1$. Factor B represents the spatial profile in the x and y directions define by Hermite polynomials H_j of order j and factor C describes the Gaussian envelope. Factor D describes how the radius of curvature of the wavefront $R(z) = z\left[1 + \left(\frac{z_R}{z}\right)^2\right]$ changes in propagation. Factor E describes the effect of the Gouy phase shift factor $(m + n + 1)\psi(z) = (m + n + 1)\arctan(z/z_R)$ which additionally depends on the mode order M. Figure 11(a) shows the intensity and phase profiles of various HG beams.

If one assumes the solution to the paraxial Helmholtz equations to instead have cylindrical symmetry, one may also the use a different separation of variables ansatz, $U(r, \phi, z) = R(r, z)\Phi(\phi, z)$. In this case, we may rewrite the equation as

$$\left(\frac{1}{r}\frac{\partial}{\partial r} + \frac{\partial^2}{\partial r^2} + \frac{1}{r^2}\frac{\partial^2}{\partial \phi^2} + 2ik\frac{\partial}{\partial z}\right) U = 0. \tag{6.4}$$

Figure 11



HG and LG beams. The intensity (main images) and phase (insets) profiles of various (a) HG and (b) LG beams. All have a beam waist of $w_0 = 0.5$ mm. The rows show increasing horizontal index $n = 0, 1, 2$ for the HG modes and increasing radial index $p = 0, 1, 2$ for the LG modes. The columns show an increase in the vertical index $m = 0, 1, 2$ for the HG modes and an increase in the topological charge $l = 0, 1, 2$ for the LG modes.

Solutions to Eq. (6.4) are known as LG modes and are given by

$$LG_p^l(x,y,z) = \underbrace{\sqrt{\frac{2p!}{w^2(z)\pi(p+|l|)!}}}_{\text{A}} \underbrace{\left(\frac{r\sqrt{2}}{w(z)}\right)^{|l|}}_{\text{B}} \underbrace{L_p^{|l|}\left(\frac{2r^2}{w^2(z)}\right)}_{\text{C}} \underbrace{e^{-\frac{r^2}{w^2(z)}}}_{D} \underbrace{e^{ik\frac{r^2}{2R(z)}}}_{\text{E}} \underbrace{e^{il\phi}}_{\text{F}} \underbrace{e^{i(2p+|l|+1)\xi(z)}}_{\text{G}}. \tag{6.5}$$

Factor A represents the mode normalization such that $\langle LG_{p'}^{l'}|LG_{p^L}\rangle = 1$ with all the variables representing the same as before. The variables p and l uniquely index each LG mode. The radial order is controlled by the p index which can have any nonnegative integer value. For values of $l = 0$, the number of rings in the LG mode is equal to p. For nonzero values of l, the number of rings in the mode is equal to $p + 1$. Factors B and C control the radial behavior of the mode along with the Gaussian envelope in Factor D. Here $L_p^{|l|}$ is the associated Laguerre polynomial, with its argument being $2r^2/w^2(z)$. Factor E represents how the radius of curvature of the wavefront changes in propagation. Factor F indicates the spiral phase of LG beams. The topological charge is controlled by l which can take any integer value, positive or negative. This topological charge results from the spiral phase front which wraps around the central axis l times per wavelength. It controls the mode's OAM such that each photon has an OAM of $l\hbar$. Factor G describes the effect of the Gouy phase $(2p + |l| + 1)\psi = (2p + |l| + 1)\arctan(z/z_R)$ which additionally depends on the mode order $M = (2p + |l| + 1)$. Figure 11(b) shows the intensity and phase profiles of various LG beams.

6.2. Divergence and Scaling of Paraxial Beams

It is important to note that the scale parameter $w(z)$ is not the beam radius of the HG or LG mode, rather, it is the size of the embedded Gaussian mode. To illustrate the point we will consider without any loss of generality the beam radius at $z = 0$ (i.e.,

$w(0) = w_0$), and use the LG modes that carry OAM as an example. The second moment radius of the OAM mode is given by $W_l = w_0\sqrt{1+|l|}$, whereas the radius of the ring of light is given by $r_l = w_0\sqrt{|l|/2}$. Clearly the size of the beam increases with mode order. The divergence, in turn, is given by $\theta_l = \theta_0\sqrt{1+|l|}$, where θ_0 is the divergence of the Gaussian beam. We see that if the LG modes are all given the same scale parameter w_0, then they will all differ in size and divergence. In contrast, they will all have the same Rayleigh length: $z_R = \pi W_l^2/(M^2\lambda) = \pi w_0^2/\lambda$. But since the sizes differ, they will experience differing degrees of turbulence by virtue of the factor D/r_0. If the sizes are to be kept constant, then each mode should have an adjusted initial beam size of $\tilde{w}_0 = w_0/\sqrt{1+|l|}$; now all beams will have the same size and experience the same turbulence, but at the cost of orthogonality: LG modes of differing sizes are not orthogonal. They also all have differing Rayleigh lengths, so will diffract differently. The message is that care should be exercised to determine what the study aims to achieve and to ensure that the light is correctly structured for the task.

6.3. Beam Shaping with an LCoS-SLM

The first type of beam-shaping device we consider is a liquid crystal on silicon (LCoS-) SLM or simply SLM. Several methods for SLM hologram generation are given in Ref. [79] and the primary method used in this work is outlined in this section. We wish to shape paraxial light beams in the transverse plane and so our hologram is treated as a single-phase element with a uniform (and very thin) thickness and a phase profile that varies only in the transverse plane. We also make two assumptions about the incident field. The first is that it is composed of monochromatic light. The fields being shaped in this work are generated by a laser of wavelength 633 nm and a spectral width of between 1 and 2 nm, making this a reasonable assumption. The second is that the incident field is uniformly polarized and aligned with the birefringent axes of the liquid crystals. Thus, the birefringence of the crystals is used only as a means to vary the phase spatially in the transverse plane and the effects on other polarizations can be ignored. In order to shape light into a desired field $U(x,y)$, one must apply a transmission function $T(x,y)$ onto some incident field $V(x,y)$

$$U(x,y) = T(x,y)V(x,y). \tag{6.6}$$

For simplicity, we assume the incident field to be a plane wave $V = e^{i(\mathbf{k}\cdot\mathbf{r}-\omega t)}$. This is reasonably achievable in the lab using common expansion and collimation techniques. This allows us to focus solely on the profile of the output field $U(x,y)$. We want our complex amplitude modulation scheme to return a field with a chosen amplitude and phase profile:

$$U(x,y) = A(x,y)e^{i\phi(x,y)}. \tag{6.7}$$

However, this is not trivial as the SLM is a refractive optical element and may only impart a phase factor onto the incident field. This phase must then be a function of the desired amplitude and phase profile of our output field and so the transmission function must be of the form

$$T(x,y) = e^{iH(A,\phi)}, \tag{6.8}$$

where H is our hologram phase. Using the third type of hologram generation in Ref. [79], we obtain the following equation for the hologram phase:

$$H(A,\phi) = J_1^{-1}(A(x,y))\sin[\phi(x,y) + 2\pi(G_x x + G_y y)]. \tag{6.9}$$

Here, J_1^{-1} is the reciprocal of the first-order Bessel function of the first kind and G_x and G_y are horizontal and vertical spatial frequencies used to create a phase grating. The grating is necessary as SLMs are not perfectly efficient with this technique and, thus,

a means of separating out the modulated light from the unmodulated light is required. Experimentally captured images of HG and LG beam and the SLM holograms used to generate them are shown in Figs. 12(a) and 12(c), respectively.

6.4. Beam Shaping with a DMD

A DMD consists of small screen made up of thousands of micrometer-scale mirrors. Each mirror can be independently controlled to direct light either toward or away from a desired direction. DMDs can then be used as diffractive optical elements in contrast to SLMs, have an amplitude only transmission function. To find this transmission function, we again assume that our incident field is that of a plane wave and aim to create an output field with the chosen amplitude and phase profile,

$$U(x, y) = A(x, y)e^{i\phi(x,y)}. \tag{6.10}$$

For simplicity, we express the transmission function of the DMD in one dimension as follows:

$$T(x) = \sum_{n=-\infty}^{\infty} \text{rect}\left(\frac{x - (n + p)x_0}{wx_0}\right). \tag{6.11}$$

Here, the mirrors' position, width and period are set by the parameters p, w, and x_0, respectively, and rect(x) is that rectangle function defined as

$$\text{rect}(x) = \begin{cases} 1, & \text{for} |x| \leq \frac{1}{2}, \\ 0, & \text{otherwise.} \end{cases} \tag{6.12}$$

One can expand this as a Fourier series and will eventually find the final expression for the DMD hologram to be [23]

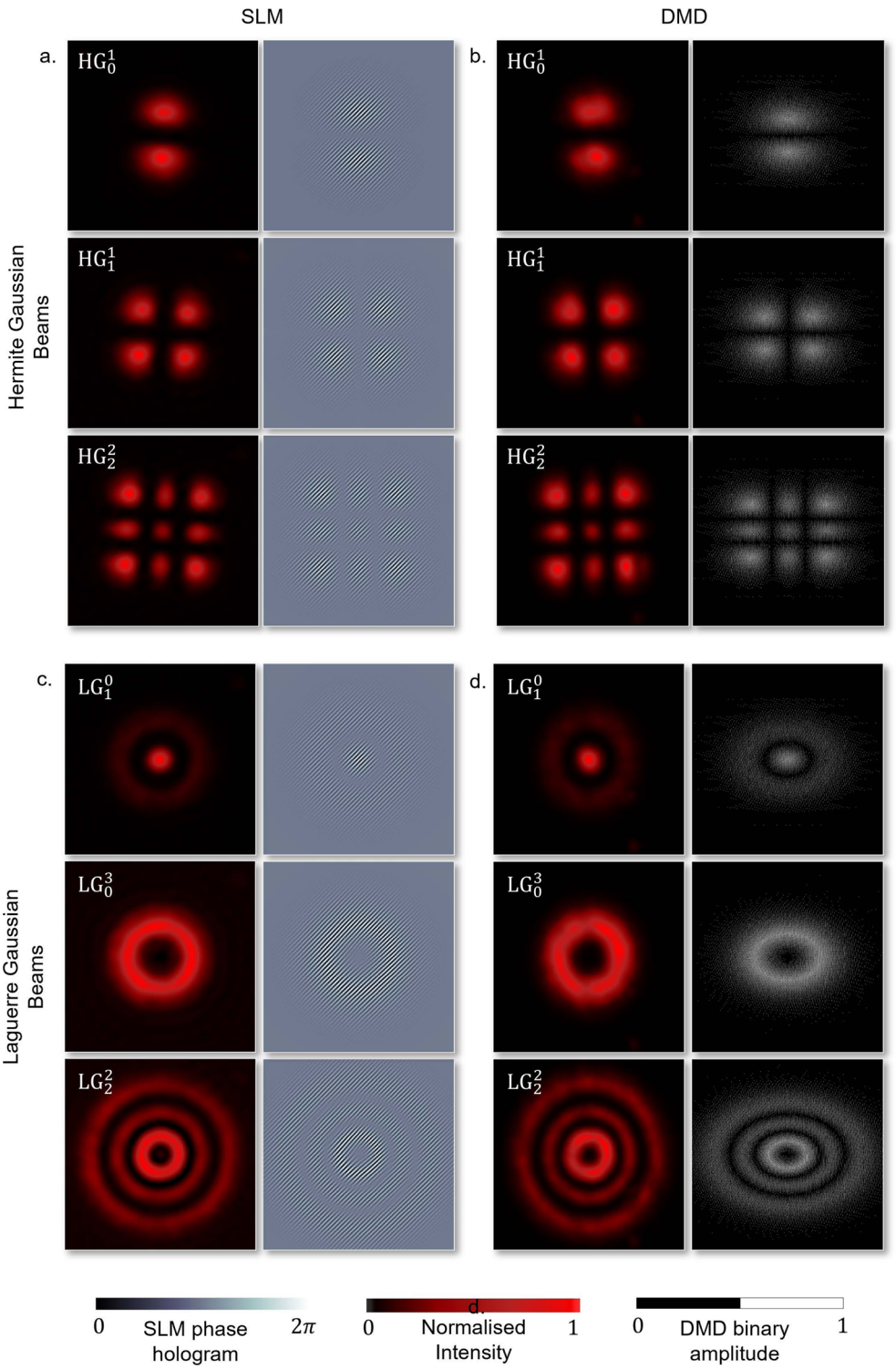
$$T(x, y) = \frac{1}{2} + \frac{1}{2}\text{sign}(\cos(2\pi(G_x x + G_y y)\pi p(x, y)) - \cos(\pi w(x, y)). \tag{6.13}$$

It is important to note that DMDs have two diffraction processes occurring simultaneously due to the presence of two sets of gratings. One is due to the programmed grating in the hologram and the other is due to the space between the micro-mirrors themselves, as they do not perfectly fill the space that they occupy. More details on beam shaping with DMDs can be found in Refs. [22,23]. Experimentally captured images of HG and LG beam and the DMD holograms used to generate them are shown in Figs. 12(b) and 12(d), respectively. The DMD holograms are slightly elongated in the horizontal direction. This has to be done as the diffraction angle of the DMD is around 12°. This angle is quite large and leads to an artificial shortening of the hologram along the horizontal direction. Thus, the encoded hologram has to be elongated to compensate for this.

7. EXPERIMENTAL IMPLEMENTATION

We now know how to numerically simulate atmospheric turbulence, how to define structured light modes and how to generate these modes experimentally using either an SLM or DMD. Now we combine these concepts to experimentally simulate a turbulent channel on an optical bench. We begin by reviewing the Fresnel scaling procedure. This will allow us to accurately relate the results we obtain with our optical bench setup to a real-world turbulent channel and vice versa. We then move onto how to construct a basic near-field mode generation setup, which will allow us to experimentally simulate the effects of turbulence for a weakly turbulent channel using a single phase screen and measuring the beam in the near-field/image plane. Instructions on how to easily modify this setup to measure the far-field of this same beam are also given. We

Figure 12



Creating structured light with digital holograms. (a) Experimental images of selected HG beams generated with the use of an SLM and the respective digital SLM phase hologram used to generate them. (b) Experimental images of selected HG beams generated with the use of a DMD and the respective binary amplitude DMD hologram used to generate them. (c) Experimental images of selected LG beams generated with the use of an SLM and the respective digital SLM phase hologram used to generate them. (d) Experimental images of selected LG beams generated with the use of a DMD and the respective binary amplitude DMD hologram used to generate them.

show how to construct a bench setup with multiple phase screens. This allows us to experimentally simulate a variety of turbulent channels with strengths ranging from the weak to the strong regime. We then end this section with a brief discussion on how to experimentally verify the strength of the constructed unit cell.

7.1. Fresnel Scaling

In general, most turbulent channels of interest are very long, from the order of several hundred meters to several kilometers. Distances in a laboratory setting are highly restricted, creating a challenge to accurately replicate real-world channels on an optical bench. However, there exists a scaling procedure [80,81] which allows one to create equivalent channels by scaling the propagation length and turbulence strength appropriately.

To see how this scaling procedure works, we begin with the Fresnel integral for the full (real-world) channel of length L,

$$\mathrm{V}(\mathbf{y}, L) = \frac{\exp(ikL)}{i\lambda L} \int \mathrm{U}(\mathbf{x}) \exp\left(\frac{i\pi}{\lambda L}\|\mathbf{x}-\mathbf{y}\|^2\right) \mathrm{d}^2\mathbf{x}, \tag{7.1}$$

where $\mathbf{x}$ are the input plane coordinates, $\mathbf{y}$ is the output plane coordinates, λ is the wavelength, $k = 2\pi/\lambda$ is the wavenumber, and $\|\cdot\|$ is the Euclidean vector norm. We then apply the following scaling parameters: $\mathbf{y}_{\mathrm{lab}} = \alpha_y \mathbf{y}$, $\mathbf{x}_{\mathrm{lab}} = \alpha_x \mathbf{x}$ and $L_{\mathrm{lab}} = \alpha_z L$, where $\mathbf{y}_{\mathrm{lab}}$ and $\mathbf{x}_{\mathrm{lab}}$ are the coordinates used in the experiment. The diffraction integral becomes

$$\mathrm{V}\left(\mathbf{y}_{\mathrm{lab}}/\alpha_y\right) = \frac{\exp(ikL_{\mathrm{lab}}/\alpha_z)}{i\alpha_x^2\lambda L_{\mathrm{lab}}} \int \mathrm{U}\left(\frac{\mathbf{x}_{\mathrm{lab}}}{\alpha_x}\right) \exp\left(\frac{i\pi\alpha_z}{\lambda L_{\mathrm{lab}}}\left\|\frac{\mathbf{y}_{\mathrm{lab}}}{\alpha_y} - \frac{\mathbf{x}_{\mathrm{lab}}}{\alpha_x}\right\|^2\right) \mathrm{d}^2\mathbf{x}_{\mathrm{lab}}. \tag{7.2}$$

To keep the diffraction equivalent with these scaled coordinates we require the Fresnel number

$$F = \frac{\pi D_i D_f}{4\lambda L} \tag{7.3}$$

to be the same in both the full and scaled-down cases, where D_i and D_f are the aperture diameters in the initial and final planes, respectively. This sets

$$\alpha_x \alpha_y = \alpha_z, \tag{7.4}$$

and the diffraction integral becomes

$$\begin{aligned} &\frac{\exp\left(ikL'\left(1-\frac{1}{\alpha_z}\right)\right)}{\alpha_r} \mathrm{V}\left(\frac{\mathbf{y}_{\mathrm{lab}}}{\alpha_y}\right) = \exp\left(-\frac{i\pi y_{\mathrm{lab}}^2}{\lambda f_y}\right) \frac{\exp(ikL')}{i\lambda L'} \times \\ &\int \mathrm{U}\left(\frac{\mathbf{x}_{\mathrm{lab}}}{\alpha_x}\right) \exp\left(-\frac{\pi(x_{\mathrm{lab}})^2}{\lambda f_x}\right) \exp\left(\frac{i\pi}{\lambda L'}\|\mathbf{x}_{\mathrm{lab}} - \mathbf{y}_{\mathrm{lab}}\|\right) \mathrm{d}^2\mathbf{x}_{\mathrm{lab}}, \end{aligned} \tag{7.5}$$

where

$$f_y = \frac{L'}{1-\alpha_x/\alpha_y}, \tag{7.6}$$

$$f_x = \frac{L'}{1-\alpha_y/\alpha_x}. \tag{7.7}$$

Setting $\alpha_y = \alpha_x$ means that the final and initial planes have the same size in the laboratory setting and $f_{x,y} \to \infty$ and the final Fresnel integral, ignoring constant phase

factors which arise due to scaling, becomes

$$\mathrm{V}\left(\mathbf{y}_{\mathrm{lab}}/\alpha_y\right) = \frac{\alpha_y \exp(ikL')}{i\lambda L'} \int \mathrm{U}\left(\frac{\mathbf{x}_{\mathrm{lab}}}{\alpha_x}\right) \exp\left(\frac{i\pi}{\lambda L'}\|\mathbf{x}_{\mathrm{lab}} - \mathbf{y}_{\mathrm{lab}}\|\right) \mathrm{d}^2\mathbf{x}_{\mathrm{lab}}, \tag{7.8}$$

which is simply a scaled form of Eq. (7.1). From this we see that we can mimic the vacuum propagation dynamics of much larger channels by appropriately scaling the coordinates in which we define our fields according to Eq. (7.4).

We also need to ensure that the turbulence phase distortions in the scaled down laboratory channel are equivalent to those in the real-world channel. To do this we begin by looking the definition of the Fried parameter in Eq. (3.1) and the Rytov variance in Eq. (3.2). If we rearrange Eq. (3.1) to isolate C_n^2 and then substitute this into Eq. (3.2), we obtain the following:

$$\sigma_R^2 = \frac{C}{k^{5/6}} \left(\frac{\sqrt{L}}{r_0}\right)^{5/3}, \tag{7.9}$$

where we have written all the numerical constants as C, k is the wavenumber, L is the length of the channel, and r_0 is the Fried parameter. With our Fresnel scaling procedure from before, we scale the propagation distance by some factor α_z. However, this change in length will, in turn, affect the Rytov variance σ_R^2 according to Eq. (7.9). To maintain the same perturbation strength and Rytov variance, we must scale the Fried parameter of the real-world channel r_0 down to some new value for the laboratory phase screens $r_{0,\mathrm{lab}}$. We see from Eq. (7.9) that if we keep everything else constant, we have a square proportionality relationship between the Fried parameter and propagation path length, $r_0^2 \propto L$. Therefore, if we scale the propagation distance by some factor α_z, then we must scale the Fried parameter by $\sqrt{\alpha_z}$ as follows:

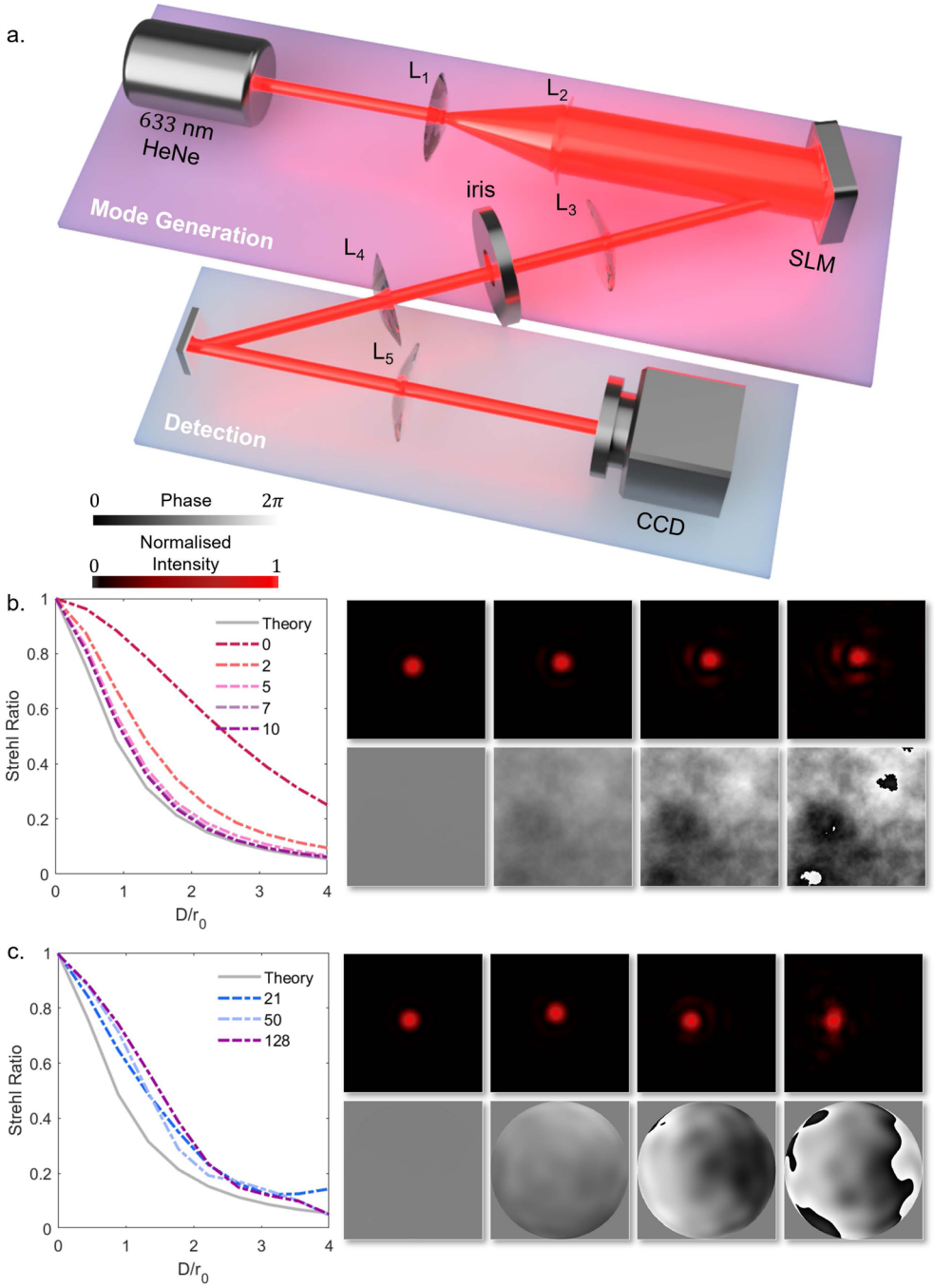
$$L_{\mathrm{lab}} = \alpha_z L \quad \Leftrightarrow \quad r_{0,\mathrm{lab}} = \sqrt{\alpha_z}\, r_0. \tag{7.10}$$

Using this, we are able replicate both the propagation dynamics and perturbation strengths of real-world turbulent channels at a much smaller scale which more easily lends itself to a laboratory/benchtop implementation. For example, let us examine the scaling of a channel of length $L = 100$ m with the Rytov variances $\sigma_R^2 = 0.5$, 1.0, and 1.5 and Fried parameters of $r_0 = 0.9$, 1.2, and 1.8 mm, respectively. Each unit cell will have a length of 33.3 m if we use three screens. To scale down this channel so that each unit cell is 1 m in the lab, our longitudinal scaling factor will be $\alpha_z = 0.03$. If we assume $\alpha_x = \alpha_y$, then we have $\alpha_x = \sqrt{0.03} \approx 0.173$. The lab Fried parameters will then be $r_{0,\mathrm{lab}} = 0.081$, 0.11, and 0.16 mm, respectively.

7.2. Experimental Setup

Our experimental setup for replicating atmospheric turbulence is shown in Fig. 13(a) and is conceptually divided into two stages: the generation stage and the detection stage. We begin in the generation stage with a He–Ne laser beam with wavelength $\lambda = 633$ nm. This beam has a typical Gaussian profile and beam waist on the order of less than 0.5 mm. The beam-shaping techniques discussed in Sections 6.3 and 6.4 both assume an incident plane wave onto the beam shaping device. Thus, our first task is to expand and collimate the laser beam so that it approximates a plane wave across the face of the SLM or DMD. This was done using a 10× objective lens L_1 to expand the beam, and then a second lens L_2 with a focal length $f_2 = 300$ mm to collimate it. The strengths of expanding and collimating lenses were chosen such that the collimated beam overfilled the screen of the SLM and ensured even illumination across the screen of the SLM. Different lenses might be needed depending on the size of the incident beam and SLM or DMD screen being used.

Figure 13



Single-phase-screen experiment. (a) To simulate atmospheric turbulence with a single phase screen in the lab, one must first expand and collimate a laser beam. We may impinge this beam onto an SLM or DMD in order to perform some beam shaping or to simply apply the turbulent phase. The modulated light can then be filtered out using a $4f$ imaging system. One may then view the aberrated beam in the near-field by placing the camera after the imaging system or view it in the far-field by placing a Fourier transforming lens after the imaging system. Plots showing the experimentally measured Strehl ratio for (b) Fourier and (c) Noll phase screens done using the single-phase-screen setup. The results are shown for an average of 100 phase screens for each turbulence strength. We see the trends match well with the numerically simulated plots. The right-hand side panels show examples of Fourier and Noll phase screens with increasing Fried parameters r_0 and the corresponding experimentally measured intensity profiles of an aberrated plane wave viewed in the far-field.

The now collimated beam was then incident on the screen of a PLUTO-VIS HoloEye SLM. The SLM screen is then encoded with a desired hologram generated using a complex amplitude modulation scheme discussed in Section 6.3. If a DMD is to be used, the encoding scheme discussed in Section 6.4 should be used instead. Such schemes were chosen as they allow for the shaping of both the phase and amplitude of our field in a single step, making it possible for us to investigate the effects of the turbulence phase perturbations on a variety of beam types including plane waves, Gaussian beams, and higher-order LG and HG modes to name a few. The nature of complex amplitude modulation results in multiple diffraction orders. Our chosen encoding schemes both place the desired field in the 1st diffraction order of the SLM or DMD. The remaining orders were then removed by making use of a $4f$ spatial filtering and imaging system consisting of a pinhole aperture or iris placed between two lenses L_3 and L_4, both with a focal length of $f_3 = f_4 = 250$ mm. Lens L_3 is placed a distance f_3 from the screen of the SLM and lens L_4 is placed a distance $d = f_3 + f_4$ from lens L_3. The iris should always be placed one focal length (a distance f_3) after the first lens L_3. The focal lengths of these lenses can be changed depending on several considerations including the desired magnification of the beam and available space on the optical bench.

The detection stage of the experiment may have different configurations depending on the desired set of measurements. If one wants to simply examine the near-field effects of atmospheric turbulence, one may simply place the camera in the focal plane of lens L_4 (i.e., the camera is a distance f_4 from lens L_4). However, since single-phase-screen turbulence is a phase-only effect, one will only be able to retrieve little information from these near-field measurements without the use of an interferometer or other phase retrieval technique. One may examine the propagation dynamics of weakly turbulent channels by making use of the Fresnel scaling procedure mentioned previously in Section 7.1. It is important to remember that if one wishes to simulate a channel with laboratory length L_{lab}, the camera must be placed a distance $f_4 + L_{\text{lab}}$ after lens L_4. This will allow one to simulate a variety of turbulent channels with varying perturbation strengths within the weak regime. Finally, if one wishes to examine the far-field effects of weak turbulence, one simply needs to add in a final lens L_5 a distance $f_4 + f_5$ from lens L_4. If the camera is then placed one focal length after L_5, intensity measurements in the far-field can be obtained.

The far-field configuration was constructed in order to experimentally verify the Fourier and Noll phase screens that were discussed in previous sections. Since the theoretical form of the Strehl ratio in Eq. (3.4) is given for the effects atmospheric turbulence of a plane wave in the far-field, it provides the perfect metric for the experimental validation of our phase screens. Since our incident beam on the SLM is already an approximate plane wave due to the expansion and collimation of the first two lenses, we may simply encode the various phase screens onto the SLM and measure the corresponding intensities on the camera. This test was carried out for both types of phase screens and the results are shown in Fig. 13(b) for the Fourier phase screens and in Fig. 13(c) for the Noll phase screens. The Strehl ratio test results show good agreement with the numerical results from Figs. 6 and 10. We see that for the Fourier screens we have very good agreement with the theoretical plot for subharmonics above 5 and for the Noll screens we have a good match to the theoretical plot for all of the number of Zernike polynomials applied. Thus, we may be confident in the ability of our Fourier and Noll phase screens to accurately replicate the effects of atmospheric turbulence on the optical bench setup.

Next to each graph in Figs. 13(b) and 13(c) we show far-field intensity measurements for a plane wave under the influence various turbulent phase screens used in performing

the Strehl ratio test. We see that under the influence of no turbulence, the far-field intensity is simply a round spot. This is to be expected as the Fourier transform of a pure plane wave (which consists of a single frequency) should be a single point in Fourier space. As we increased the strength of the turbulence, we see that the round spot becomes increasingly aberrated. This is due to the addition of higher and higher spatial frequencies from the Fourier and Noll phase screens. Therefore, with a higher turbulence strength we see what we expect: larger perturbations to the far-field intensity.

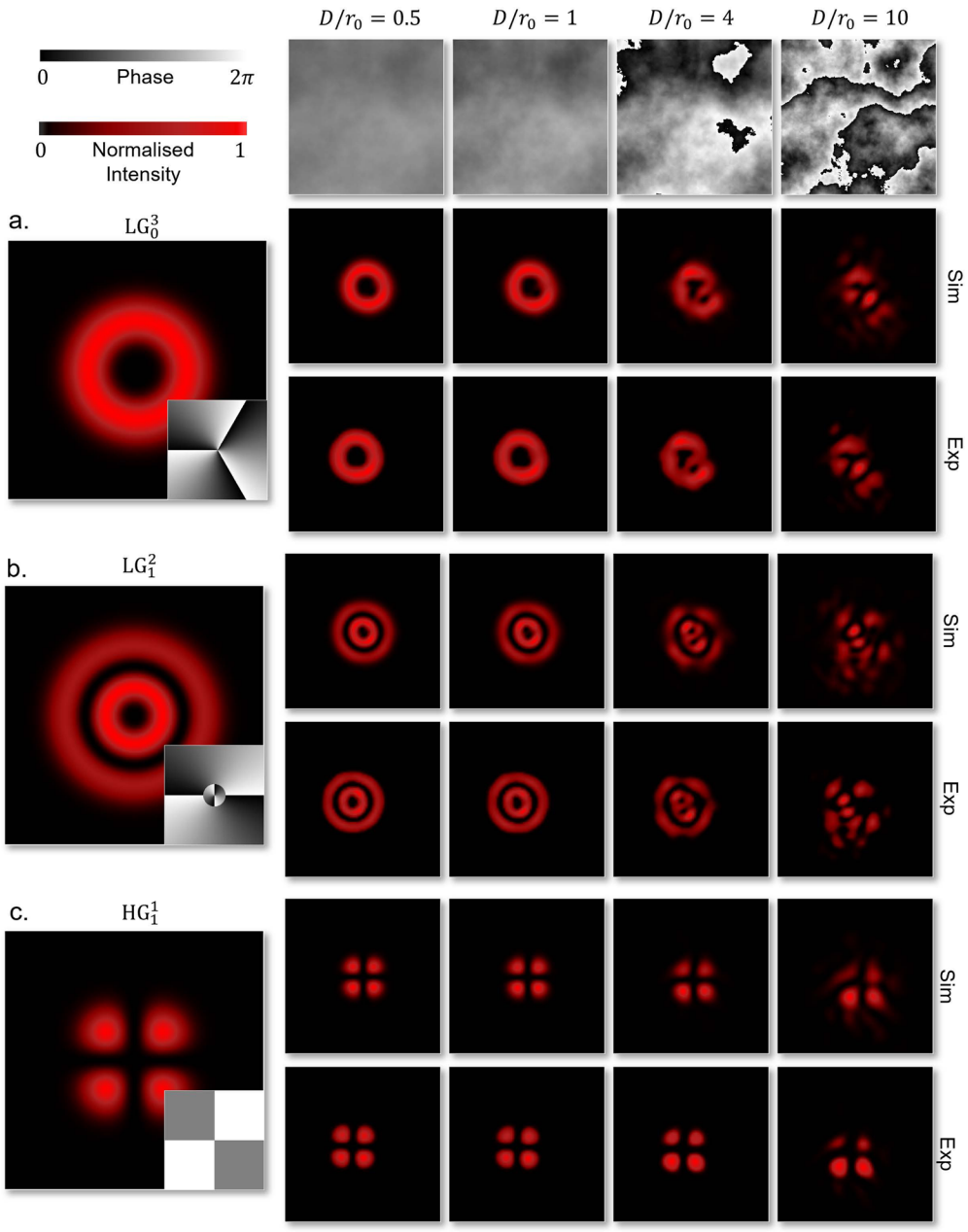
Figure 14 shows the numerical and experimental far-field effects of turbulence on various structured light beams using Fourier phase screens. The setup used to obtain the experimental intensity measurements is the same as shown in Fig. 13(a). We show the effects explicitly for the beams LG_0^3, LG_2^1, and HG_1^1. The effects are shown for turbulence strengths $D/r_0 = 0.5, 1, 4$, and 10. We see that for each beam, the extent of the intensity perturbations in the far-field increases as the strength of the turbulence increases. The same results are shown in Fig. 15 for Noll phase screens using the same structured light beams for comparison. We see again that an increase in the turbulence strength results in a more aberrated intensity profile in the far-field. We also see that for both the Fourier phase screens and the Noll phase screens, the experimentally measured, aberrated intensity profiles agree very well with the numerically simulated, aberrated intensity profiles. This shows that the use of both numerical wave-optic simulations and the use of an experimental optical bench setup both provide adequate and complementary ways of investigating the effects of atmospheric turbulence on structured light beams.

7.3. Experimentally Simulating a Thick Atmospheric Medium

Now that we are confident with experimentally simulating weak atmospheric turbulence using a single phase screen, we move onto strongly turbulent and extended turbulent channels. In order to achieve this, we make use of the multiple-phase-screen approach we discussed in Section 4.3. In numerical simulation, it is possible to use as many turbulence phase screens as the memory and processing power of the computer can handle. In the experimental context, the number of phase screens is restricted by the number of optics available to the user. Therefore, before one embarks on an experimental investigation, one must consider if the equipment available will be sufficient to simulate the desired channel and turbulence strengths. As we show in this section, it is possible to make efficient use of devices such as SLMs and DMDs by dividing the screen in half or into thirds and bouncing off of each division thus increasing the number of phase screens while using the same number of optical elements. The increased number of bounces also increases the difficulty of the alignment process and, thus, time and accuracy considerations are also important when deciding what channels one wishes to simulate. The geometry of the optical setup will also be tied to the Fresnel scaling and Rytov scaling procedures discussed previously.

We are able to accurately replicate weak, medium, and strong turbulence in a 100 m channel (with Rytov variances of $\sigma_R^2 = 0.5$, 1.0, and 2, respectively) using only three phase screens. The experimental setup for this is shown in Fig. 16(a) and can be broken up into three stages: the mode generation stage, the turbulence replicator stage, and the detection stage. The mode generation stage is the same as shown in Fig. 13(a). The turbulence replicator stage follows directly from the generation stage with the beam propagating a distance $f_4 + \Delta z_{\mathrm{lab}}$ after lens L_4 before impinging onto one half of the screen of a second SLM (where $L_{\mathrm{lab}} = N\Delta z_{\mathrm{lab}}$). The beam then propagates a distance Δz_{lab} before impinging on the other half the second SLM's screen with the help of a mirror. The beam then propagates a final distance $\frac{1}{2}\Delta z_{\mathrm{lab}}$ before it reaches the camera to take intensity measurements. A turbulence phase screen can be encoded onto the first

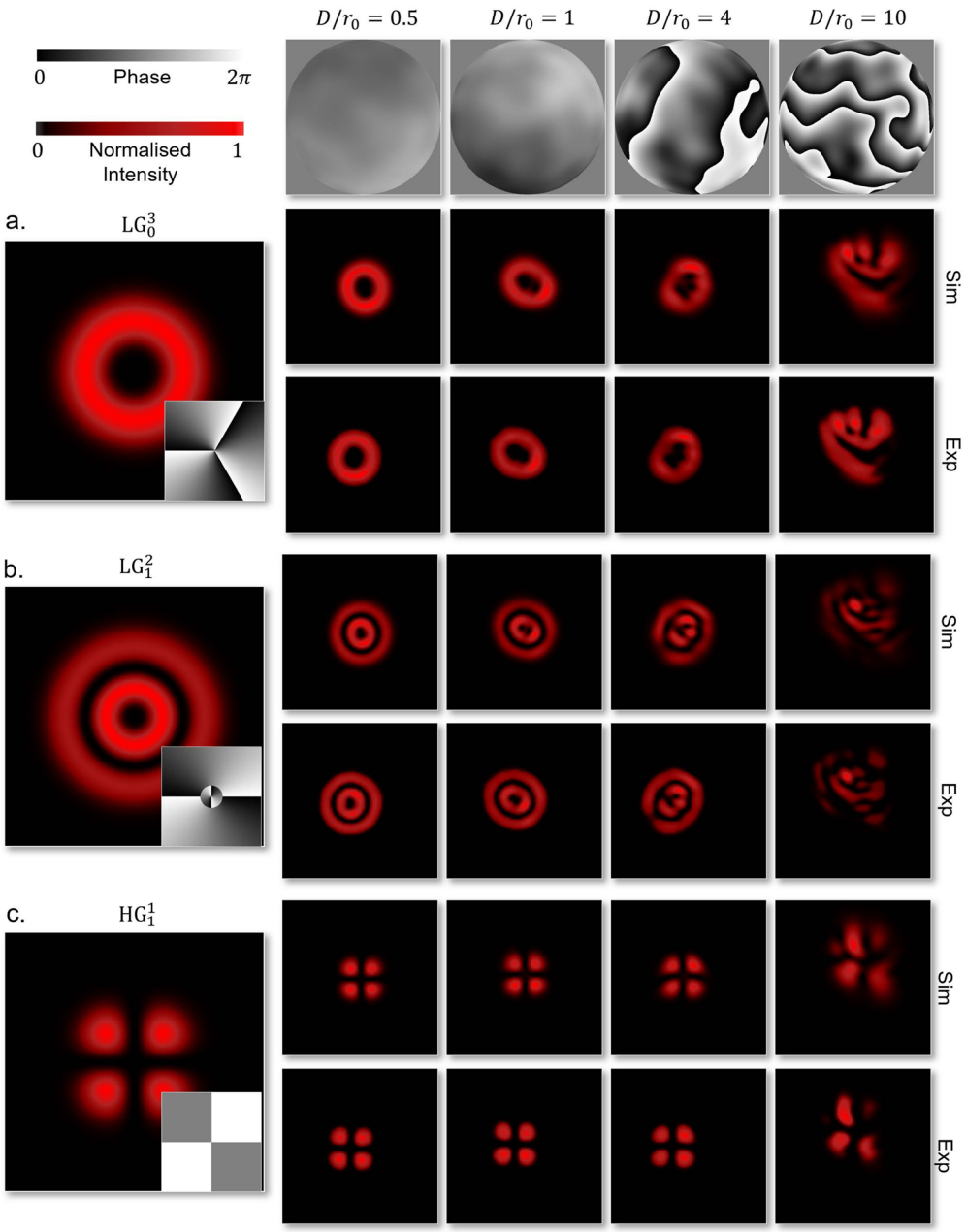
Figure 14



Beams through Fourier phase screens. Here we show the behavior of various structured light beams in the far-field after being aberrated by Fourier turbulence phase screens. We show this both in numerical simulation and in experiment for (a) LG_3^0, (b) LG_1^2, and (c) HG_1^1 with turbulence strengths $D/r_0 = 0.5$, 1, 4, and 10 where D is the aperture size and r_0 is the Fried parameter. The experimental results were obtained using the setup described in Fig. 13.

SLM along with the desired complex light field (numerically propagated by a distance Δz_{lab}) to simulate the first half-segment in our split-step approach. Turbulence phase screens can then also be programmed onto each half of the second SLM screen to simulate the second and third segment of the channel. Each unit cell was 1 m in length for a total of 3 m channel in the lab. The Fresnel number of the channel was 1.7.

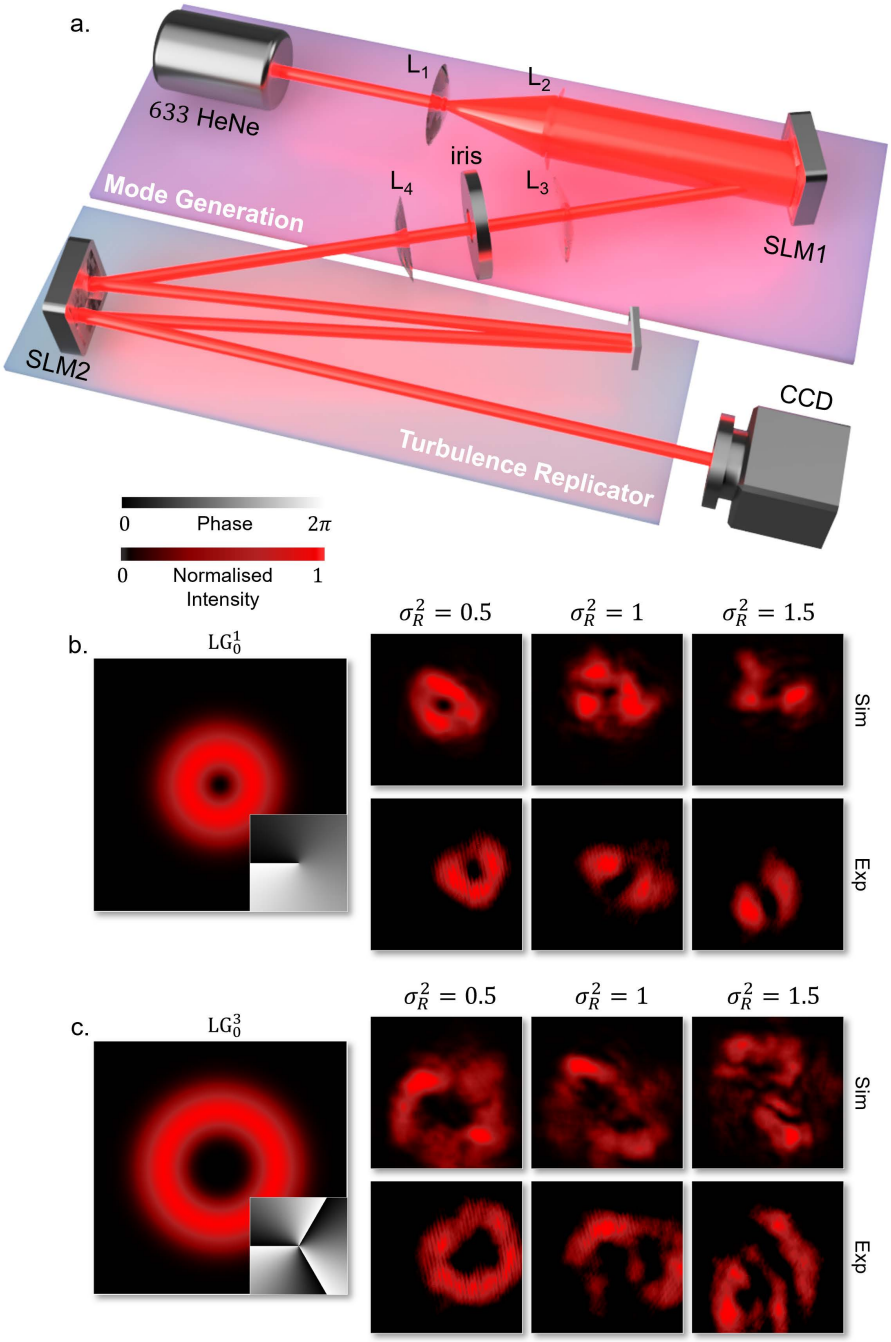
Figure 15



Beams through Noll phase screens. Here we show the behavior of various structured light beams in the far-field after being aberrated by Noll turbulence phase screens. We show this both in numerical simulation and in experiment for (a) LG_0^3, (b) LG_1^2, and (c) HG_1^1 with turbulence strengths $D/r_0 = 0.5$, 1, 4, and 10 where D is the aperture size and r_0 is the Fried parameter. The experimental results were obtained using the setup described in Fig. 13.

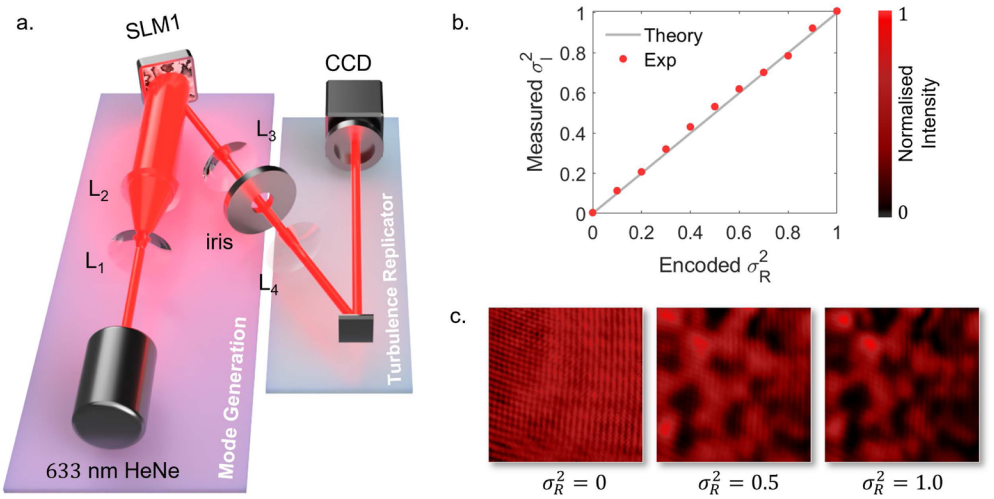
In Figs. 16(b) and 16(c) we show numerical and experimental results of structured light beams propagating through weak, medium, and strong turbulence using the split-step method. Results are shown for an LG_1^0 and LG_3^0 beams, respectively. One can see that the greater the turbulence strength (quantified by the Rytov variance), the more significant the perturbation to the structured light mode in both the numerical and experimental cases. It is difficult to determine how these results compare with

Figure 16



Experimental thick medium. (a) We simulate a thick atmospheric medium by using the same mode generation setup as in Fig. 13. After the $4f$ spatial filter, we allow for a distance of propagation equal to the length of one scaled down unit cell Δz before impinging the beam on one half of a second SLM, upon which a second phase screen can be encoded. We then allow the beam to propagate a distance Δz before it impinges on the second half of the second SLM. upon which the third and final phase screen is encoded. The beam then propagates a final distance $\frac{1}{2}\Delta z$ before hitting the detector. We show the simulated and experimental intensity profiles of (b) a LG_0^1 beam and (c) a LG_0^3 beam after passing through channels with Rytov variances equal to $\sigma_R^2 = 0.5$, 1, and 1.5.

Figure 17



Experimental Rytov variance verification. (a) To experimentally verify the Rytov variance of a unit cell, we first expand and collimate a laser beam using a telescope system. This creates an approximate plane wave. The beam then impinges onto an SLM that is encoded with a turbulence phase screen calculated with the necessary Fried parameter r_0 for the desired Rytov variance σ_R^2 and unit cell length L_{lab}. The beam is then sent through a $4f$ spatial filter system to isolate the 1st diffraction order of the SLM. The camera is then placed a distance $L_{\text{lab}}/2$ after the $4f$ spatial filter to propagate through the second half of the unit cell. (b) Plot showing the encoded Rytov variance of the channel/unit cell σ_R^2 versus the experimentally measured scintillation index σ_I^2. (c) Experimentally captured intensity images of the plane wave after passing through the experimentally simulated channel for various turbulence strengths $\sigma_R^2 = 0$, 0.5, and 1.0.

those from real-world atmospheric turbulence. There are very few investigations in the literature making qualitative and quantitative comparisons between simulated and real-world channels. This leaves room for future work on making these comparisons and validating our current models and spectra for simulating turbulence.

We are able to verify that the unit cell we construct in the laboratory is inducing an accurate perturbation strength σ_R^2 by experimentally performing the same procedure as described in Fig. 4. Figure 17(a) shows the details of the experimental setup. The setup is the same as in Fig. 16(a); however, we place the camera at the end of the first unit cell, a distance $f_4 + L_{\text{lab}}/2$ after L_4. This is so we can measure the beam after propagating through only one unit cell. Because the beam impinging onto the SLM is a significantly expanded and collimated Gaussian beam, it can be treated as a plane wave. Thus, we only encode the turbulence phase screen onto the SLM so that the plane wave will pick up the turbulent phase and then reflect off the SLM. It then passes through the $4f$ spatial filter, before propagating a distance $L_{\text{lab}}/2$ through the second half of the unit cell to the camera to be measured. By using a plane wave, we are able to measure its scintillation index σ_I^2 given by Eq. (3.5) and easily relate it to the unit cell's Rytov variance σ_R^2. Figure 17(b) shows the theoretical relationship between σ_I^2 and σ_R^2 (gray line) and the encoded σ_R^2 versus the experimentally measured σ_I^2 (red dots). The range of Rytov variances encoded encapsulates the limits of the weak scintillation regime and the range of strengths in which the single-phase-screen approximation holds. We see that there is excellent agreement between theory and experiment, thus indicating that we are in the weak scintillation regime and that the encoded turbulence strengths

are accurately realized experimentally. Figure 17(c) shows three experimental images of the intensity of the plane wave after propagating through three unit cells of varying turbulence strengths $\sigma_R^2 = 0.0$, 0.5, and 1.0. As expected, we see that the stronger the turbulence strength, the more variation there is in the final intensity of the beam.

8. TIME-VARYING TURBULENCE

So far, we have generated static phase screens, each representing a turbulent channel frozen in time. However, it is sometimes of interest to examine the behavior of light through a turbulent channel as it evolves over a period of time. The approach to modeling this behavior depends on the regime one wishes to investigate. If one is interested in time steps greater than the coherence time of the turbulent channel τ_0 (also called the Greenwood frequency in some contexts and is typically in the range of 10–100 ms), one may simply use a new phase screen for each time step. This is because by definition the time between each step is greater than the correlation time and so the phase perturbations at time t_1 are not correlated to the perturbations at time t_2 and, thus, should be modeled using completely uncorrelated phase screens. There are very interesting dynamics that one might wish to investigate on time scales or time steps smaller than the coherence time τ_0. In these cases we need to devise a method for generating a sequence of turbulent phase screens that change according to the behavior of the medium. It turns out that these changes are simply shifts in position proportional to the wind velocity during that time step.

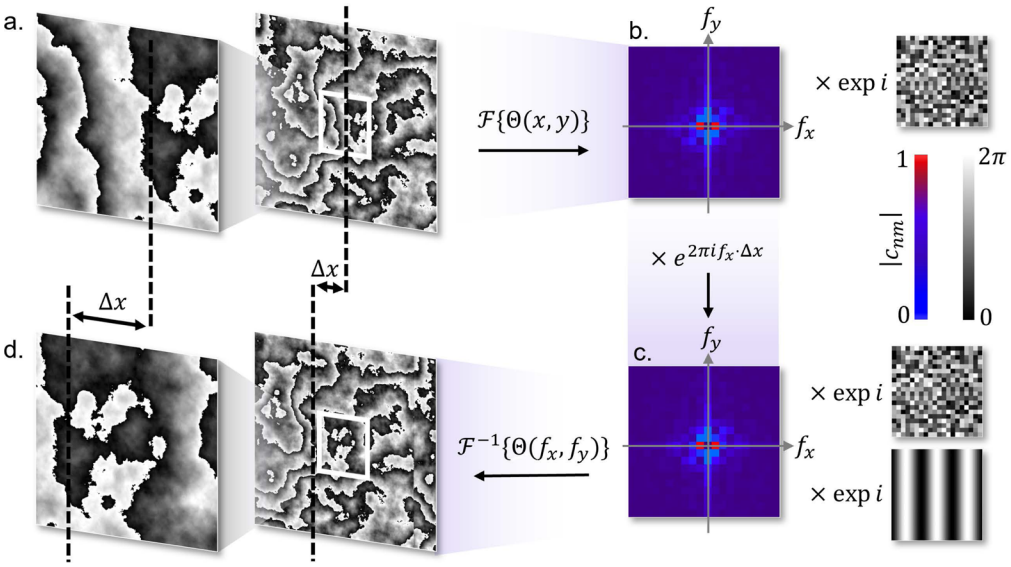
Let us assume that we wish to simulate time-varying turbulence in a channel with a resolution of $N \times N$ and a pixel spacing $\delta x = \delta y$ in the transverse plane. We first generate a single, large, static, turbulence phase screen with the same pixel spacing but at a much larger resolution. This large screen will be shifted around according to our velocity calculations to generate each iteration of our smaller, time-varying phase screens. We take the central $N \times N$ pixels of our large screen and save this as our first screen in the sequence of time-varying phase screens. We then shift the larger screen so we can crop out the next smaller screen in the sequence. One's first instinct might be to simply take the wind speed, multiply by the size of the time step δt, and shift the screen the corresponding distance $\Delta x = v\delta t$ in the appropriate direction. However, this is not always possible due to the discrete nature in which we define the phase screen in the spatial domain. Sometimes we find that $\Delta x \neq n\delta x$ (for some integer n) or that $\Delta x < \delta x$. In these cases it would not be possible to accurately shift the screen. To circumvent this issue and to ensure we always shift our screen the correct distance, we can make use of the Fourier shift theorem, which states that

$$\mathcal{F}[f(x - \Delta x)] = e^{2\pi i f_x \Delta x} \mathcal{F}[f(x)]. \tag{8.1}$$

The procedure for implementing this is shown in Fig. 18. In Fig. 18(a) we crop out the central region of our large turbulent screen. We then take the Fourier transform of our screen and multiply it by the phase shift factor $e^{2\pi i f_x \Delta x}$ as shown in Figs. 18(b) and 18(c). Finally, we take the inverse Fourier transform of this new field, as shown in Fig. 18(d) to retrieve our shifted large turbulence phase screen in the spatial domain. We crop out the central $N \times N$ region to define the new phase screen in our sequence of time-varying phase screens. This process is then repeated in a loop for as many time steps as needed, with each new iteration using the shifted large phase screen from the previous iteration.

While one may choose to use to the same value for the wind speed through the entire simulation of the time-varying phase screens, we see from Kolmogorov's original statement of his theory that the velocity in a turbulent medium is not constant and undergoes various fluctuations. If the velocity was constant, we would not have a

Figure 18



Time-varying phase screens. (a) In order to generate time-varying turbulence we begin with a phase screen that is much larger than the sending and receiving apertures of the system. We cut out a small region the size of the system aperture in the center of this larger phase screen and use this as the first time-varying phase screen. (b) To obtain the next time-varying phase screen, we Fourier transform our large phase screen into the spatial frequency domain which, in general, will have real and imaginary components. (c) We make use of the Fourier shift theorem and multiply our Fourier transformed large phase screen by a "shifting phase" proportional to the wind velocity and time step duration. (d) We then inverse Fourier transform the large phase screen with the additional shifted phase to recover a new large phase screen, which is a position-translated version of the initial large phase screen. We then cut out a small region in the center of this new large phase screen the same size as the system aperture and use this as our second time-varying phase screen. This process is then repeated as many times as necessary to obtain the desired number of time-varying turbulence phase screens.

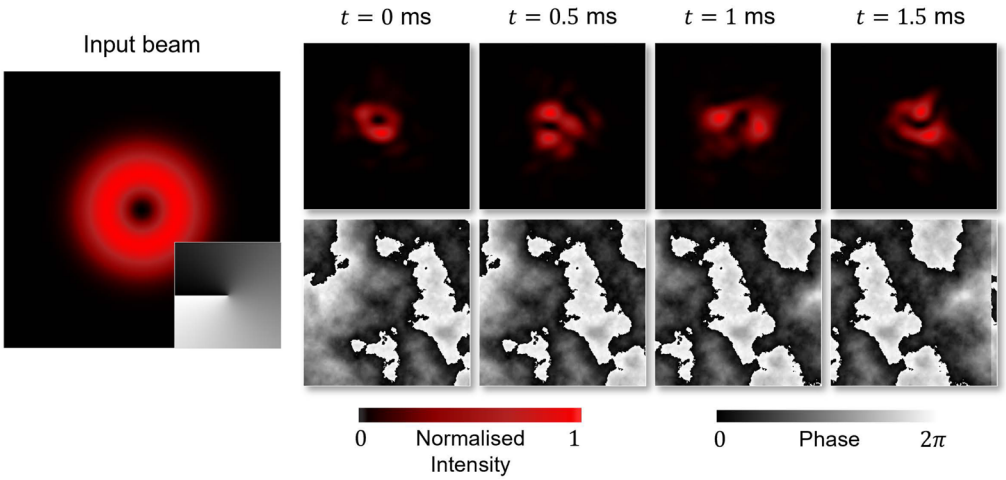
turbulent medium to begin with. Thus it would be more appropriate to specify a mean velocity v_{mean} and variance in the velocity σ_v^2 and then sample the velocity at each time step from a normal distribution with mean v_{mean} and variance σ_v^2.

Simulated results of a LG beam with beam waist $w_0 = 1.5$ mm, azimuthal index $l = 1$, and $p = 0$ propagating through time-varying turbulence are shown in Fig. 19 at times $t = 0$, 0.5, 1, and 1.5 ms. The Fried parameter for the channel was $r_0 = 1.58$ mm and the propagation distance was $z = 10z_R \approx 112$ m, where z_R is the Rayleigh range of the beam. These time-varying phase screens can be implemented using the same experimental setups as discussed in the previous section in order to experimentally investigate the properties of time varying channel in a controlled setting.

9. EIGENMODES OF ATMOSPHERIC TURBULENCE

We have now developed the tools to accurately model the effects of atmospheric turbulence both numerically and in the laboratory. We have seen that with these techniques we are able to accurately reproduce the distortion and aberrations induced when light propagates through a turbulent channel. We have seen the effects this has on structured light beams in particular, severely aberrating the amplitude and

Figure 19



Beams through time-varying turbulence. Here we show the far-field evolution of a LG_0^1 beam under the effect of simulated time-varying turbulence. The length of each time step is 0.5 ms, the turbulence strength is $D/r_0 = 8.1$, and the beam waist is $w_0 = 1.5$ mm.

phase profiles of the beams. These effects are detrimental for the implementation of structured light in various settings and applications including for sensing, detection and ranging, defence, and communication, both classical and quantum.

The problem is that we have found the solutions to the wave equation without any perturbation (vacuum) and then propagated these modes in a perturbing system: atmospheric turbulence. Now, in this section, we aim to calculate the modes of the perturbing medium itself, i.e., the paraxial modes of structured light that will remain unaffected by the refractive index fluctuations of the medium. These are known as eigenmodes of the medium and are specially constructed such that, to them, the medium appears to be transparent. These modes can be calculated for channels of arbitrary length and perturbation strength and their robustness have been both numerically tested and experimentally validated [52]. This approach works remarkably well for atmospheric turbulence and can even be generalized and extended to other kinds of aberrated channels.

9.1. Mathematically Defining Eigenmodes of Turbulence

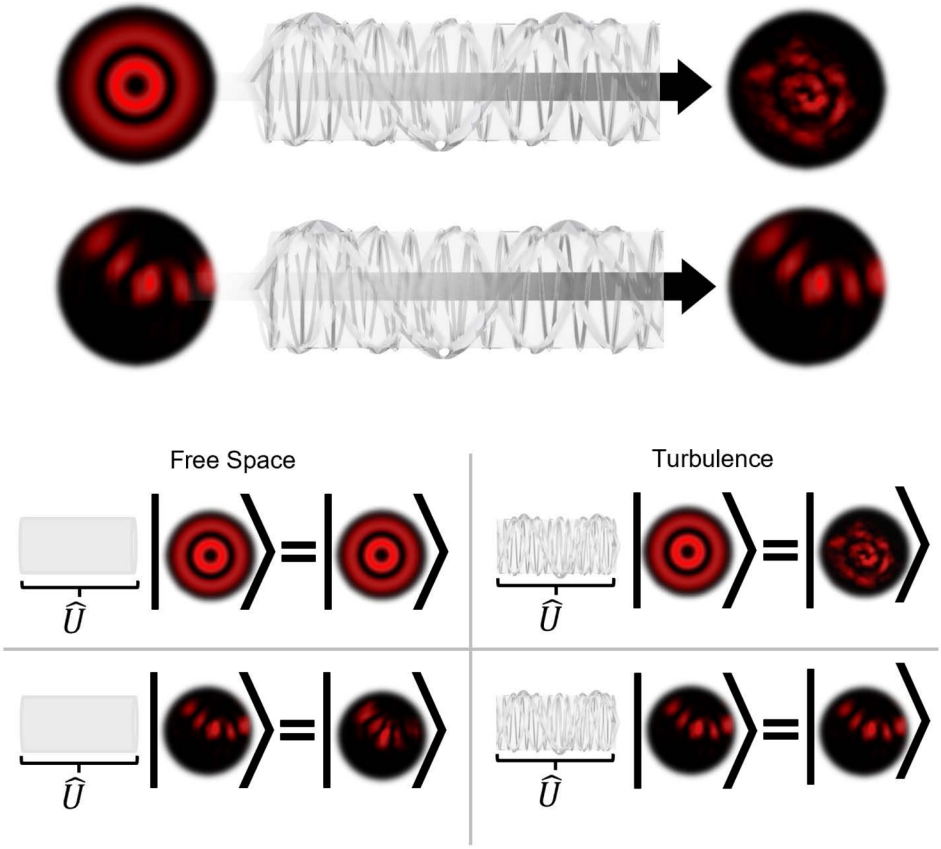
We illustrate the idea behind the eigenmode notion in Fig. 20. We begin with some structured light field that passes through an extended medium of arbitrary length and perturbation strengths. We interchangeably refer to this medium as the channel. Typical forms of structured light such as LG and HG will pass through a perfectly uniform medium unchanged but beams will pass through the turbulent channel and exit severely distorted. Conversely, when eigenmodes of the channel propagate through the channel they exit unchanged, but will become distorted when they propagate through vacuum or some other uniform medium.

To obtain the eigenmodes, we treat our distorted channel as a linear operator $\hat{U}$ that acts on a given input complex light field and returns a complex output field,

$$\hat{U}u_{\mathrm{in}} = u_{\mathrm{out}}. \tag{9.1}$$

We show this operator and the input and output field in the right-hand side panels of Figure 20. We make some assumptions about our channel and the operator. Namely,

Figure 20



Propagation through turbulence. Most common forms of structured light (such as LG modes) become distorted when propagating through free space due to the effects of atmospheric turbulence, whereas an eigenmode of atmospheric turbulence will remain unchanged when propagating through the same channel, as shown in the left panels. In contrast, the eigenmodes of turbulence will not be the eigenmodes of pristine free space, as shown on the right panels.

that the channel and, thus, the operator is unitary and that the aperture of our transmitter and receiver are large enough to collect and send the number of eigenmodes we wish to use. The number of modes a system can accommodate may be calculated by approximating the free-space limit of the system $N_{\max} \approx A_t A_r/(\lambda^2 L^2)$ where A_t and A_r are the transmitter and receiver aperture areas separated by a distance L for light of wavelength λ. Equation (9.1) can be recast as an eigenvector problem by insisting that $u_{\text{in}} = u_{\text{out}} = |\gamma\rangle$ so that

$$\hat{U} = \sum_i s_i |\gamma_i\rangle\langle\gamma_i|. \tag{9.2}$$

In order to obtain the eigenvectors $|\gamma_i\rangle$, we need to recast the operator as a transmission matrix whose elements U_{ij} map the input basis states to the output basis states, i.e., $u_i = \sum_j U_{ij} u_j$. In this approach we use the pixel basis both at the input and the output plane to express the eigenmodes. We make this choice because of the known form of the free-space Green's function, which is defined in position basis. However, one is not limited to only this choice and can use any orthogonal basis to define and/or reconstruct the channel. For example, we may shift our channel matrix in the position basis U and express it some other orthogonal basis via $A = PUQ^\dagger$, where P and Q the unitary matrices that perform the change of basis.

9.2. Numerical Simulations

In order to obtain the operator for our turbulent channel, we divide it up according to our split-step approach for a thick medium as described in Fig. 3 and Eq. (4.18). This technique is excellent because without access to a real-world channel, one may still construct a realistic operator for a turbulent channel and test this numerically and in the lab. We do have a mathematical expressions for the operator of each segment/unit cell, given by Eq. (4.17). However, the propagation operator is in a differential form and, thus, not easily used in modeling propagation. We instead use the fact that we are in the weak regime where turbulence is simply a phase perturbation (i.e., for some unperturbed spatially varying complex field V, $V_{\text{turb}} = Ve^{i\theta}$) and make use of the Huygens–Fresnel diffraction integral which provides a closed-form analytical expression for the free-space propagation of a field,

$$V(\mathbf{x}', z) = T\mathrm{V} \equiv \int \mathrm{d}^2\mathbf{x}\; g(\mathbf{x}, \mathbf{x}'; \Delta z) \exp(i\Theta)\mathrm{V}(\mathbf{x}, 0), \tag{9.3}$$

where

$$g(\mathbf{x}, \mathbf{x}'; \Delta z) = \frac{1}{i\lambda\Delta z} \exp\left(\frac{i\pi}{\lambda\Delta z}\|\mathbf{x} - \mathbf{x}'\|^2\right) \tag{9.4}$$

is the paraxial free-space Green's function, T is the turbulence operator, $\mathbf{x}$ represents the input plane coordinates, and $\mathbf{x}'$ represents the output plane coordinates. Because we will be simulating turbulence numerically using either the Fourier phase screens or Noll phase screens discussed earlier, we must also discretize our input and output planes. We discretize them into grids each with $N \times N$ points and label the coordinates as $\mathbf{x} \equiv (x_\alpha, y_\beta)$ and $\mathbf{x}' \equiv (x_\mu, y_\nu)$, so that T is given by

$$T_{\mu\nu\alpha\beta} = \frac{1}{i\lambda\Delta z} \exp\left(\frac{i\pi}{\lambda\Delta z}\left(x_\mu - x_\alpha\right)^2\right) \exp\left(\frac{i\pi}{\lambda\Delta z}\left(y_\nu - y_\beta\right)^2\right) \exp\left(i\Theta(x_\alpha, y_\beta)\right). \tag{9.5}$$

Note that T is a four-dimensional tensor as we are mapping from a two-dimensional input space to a two-dimensional output space. A state E with elements $\mathrm{E}_{\mu\nu} \equiv \mathrm{E}(x_\mu, y_\nu)$ is an eigenmode of this operator if it is a solution to the tensor eigenvalue equation

$$T_{\mu\nu\alpha\beta}\mathrm{E}^n_{\alpha\beta} = \gamma_n \mathrm{E}^n_{\mu\nu}, \tag{9.6}$$

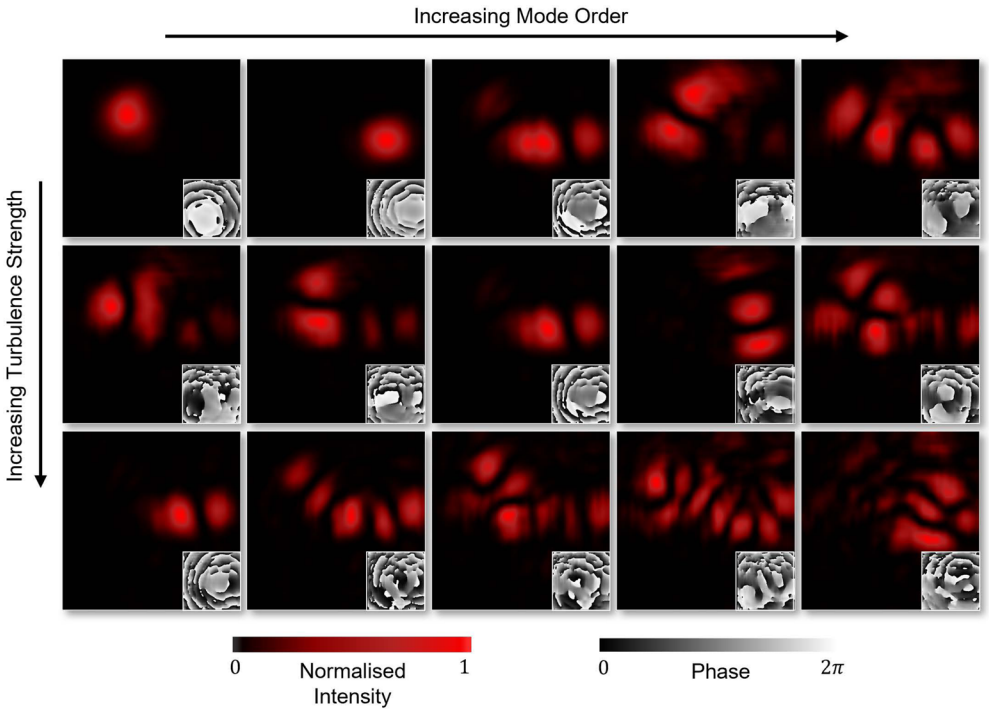
where the eigenvalue of the nth eigenvector is given by γ_n and we implicitly sum over repeated indices. Tensor equations are not easy to work with directly and we wish to rewrite this in a more familiar form such as a matrix equation. To achieve this, we define a mapping ρ which takes in the discrete indices of the input grid (α, β) and output grid (μ, ν) and "counts" them one column at a time. More explicitly, the mapping gives $\rho(1,1) = 1, \ldots, \rho(N,1) = N$, $\rho(1,2) = N+1$ up to $\rho(N,N) = N^2$. We may then rewrite Eq. (9.6) as

$$\gamma_n \mathrm{E}^n_i = T_{ij}\mathrm{E}^n_j, \tag{9.7}$$

where we have used $\rho(\alpha, \beta) = j$ and $\rho(\mu, \nu) = i$. Since this is a normal eigenvalue matrix equation, it can be easily solved using a menagerie of numerical routines to ultimately find the eigenmodes of the channel.

Examples of the intensity and phase of the eigenmodes are shown in Fig. 21 for various examples of turbulence. Here the first five eigenmode solutions are shown in the left column, increasing from left to right, with the rows corresponding to the turbulence strength, increasing from top to bottom. Although these are complex forms of structured light, as eigenmodes of turbulence they should be invariant after propagation through a turbulent atmosphere. To test this, we propagate OAM carrying LG modes and the eigenmodes through various scenarios of turbulence over a 100-m

Figure 21

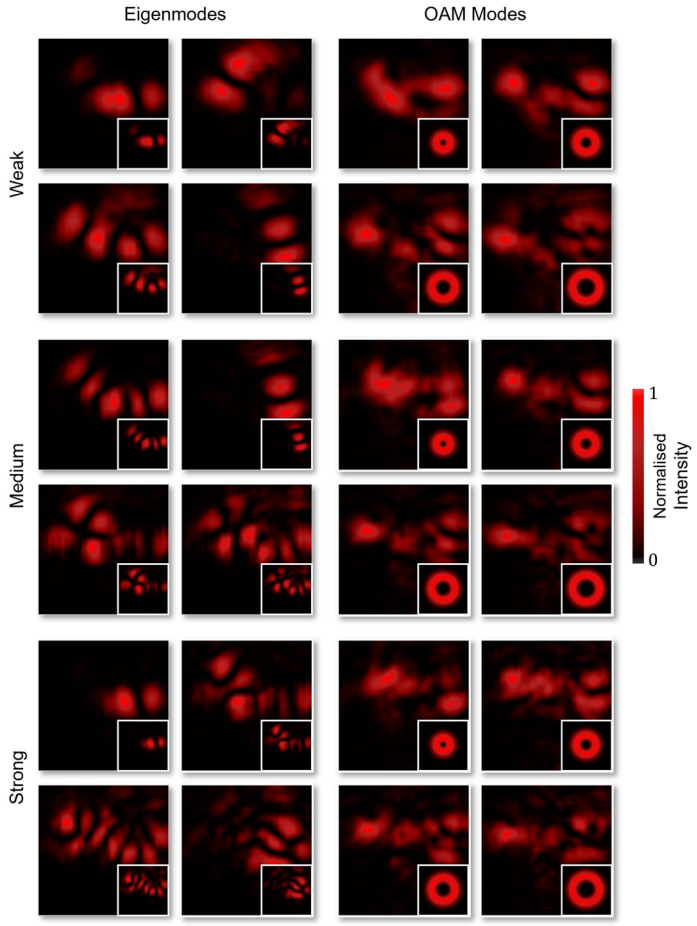


Eigenmodes of turbulence. The numerically calculated eigenmodes of turbulence, showing the first five modes (columns) as a function of turbulence strength (rows). The insets show the phase profile. All eigenmodes were calculated for a total propagation path of 100 m through weak, medium, and strong turbulence as defined by the Rytov variance (σ_R^2) and Fried parameter (r_0). The first row shows eigenmodes of weak turbulence with $\sigma_R^2 = 0.5$ and $r_0 = 1.8$ mm. The middle row shows eigenmodes of medium turbulence with $\sigma_R^2 = 1$ and $r_0 = 1.2$ mm. The last row shows eigenmodes of strong turbulence with $\sigma_R^2 = 1.5$ and $r_0 = 0.91$ mm.

path length, with the results shown in Fig. 22. OAM modes were selected as they are very popular forms of structured light used in free-space studies. Their popularity, however, is not commensurate with their robustness in turbulence, as their phase profiles are sensitive to atmospheric distortions. We see that while the OAM modes are distorted (as expected), the eigenmodes are robust. This can be quantified by performing a modal analysis [82] at the end of the turbulent channel, as would be the case in optical communication at the receiver. In Fig. 23 we see that while the cross talk is substantial for OAM modes when propagated through turbulence, evident from the many off diagonal terms, the eigenmode cross-talk matrix remains diagonal after the same channel, for minimal cross talk.

We perform the experiment using the same procedure as outlined in the earlier sections. The results of OAM and the eigenmodes for weak, medium, and strong turbulence are shown in Fig. 24. The collage shows the final measured eigenmodes after the channel, with the insets showing the initial mode as prepared prior to the channel. The robustness of the eigenmodes is clearly evident, in contrast to the highly distorted OAM modes. While there are slight intensity changes for the eigenmodes of turbulence, these are extremely small in comparison with the intensity fluctuations experienced by the OAM modes. The level of distortion in the eigenmodes does seem more profound for the weak turbulence case. However, each turbulence strength constitutes a different realization of turbulence and so this cannot be taken as a general trend until a large

Figure 22

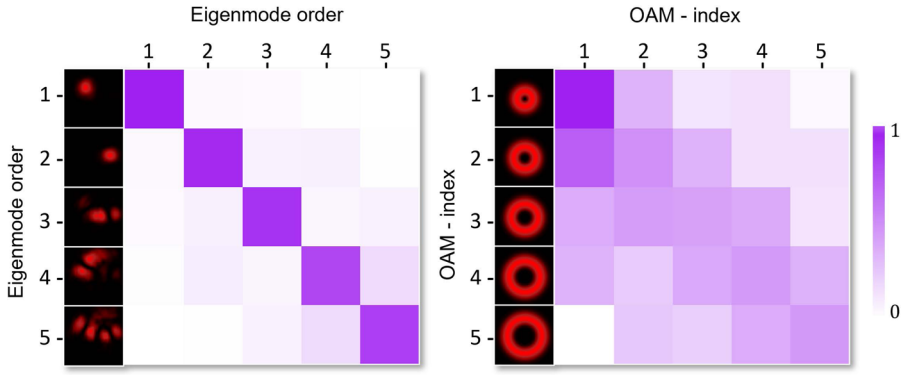


Invariance of eigenmodes under numerical propagation through turbulence. The eigenmodes (left) and LG modes (right) after numerical propagation through weak, medium and strong turbulence through a channel equivalent to propagating over a distance of 100 m. The insets shows the modes before experiencing turbulence. The numerical simulations used the split-step method with three unit cells each consisting of a turbulence screen with a given r_0 followed by 33.33 m of propagation. Three unit cells were chosen to most closely match the experimental conditions implemented earlier. Weak turbulence was characterized by $\sigma_R^2 = 0.5$ and $r_0 = 1.8$ mm, medium turbulence by $\sigma_R^2 = 1$ and $r_0 = 1.2$ mm and strong turbulence by $\sigma_R^2 = 1.5$ and $r_0 = 0.91$ mm.

number of eigenmodes for various realizations of turbulence have been generated and analyzed.

We have outlined how to find the eigenmodes of a turbulent path, and demonstrated it with a laboratory-based split-step example both numerically and experimentally. These modes are eigenmodes in their truest sense, i.e., they are fixed under the action of the channel. Importantly, our approach works even when the medium is long and the aberration strong, a regime where traditional adaptive optics often fails (beyond a Rytov variance of order 1) [83,84]. By their nature and construction, the eigenmodes are robust only to a specific channel. For applications in real-world contexts in which turbulence is dynamic and rapidly changing, the modes should propagate through the medium faster than the channel's coherence time. For typical channels, this is of the order of 10–100 ms, which is significantly slower than the nanoseconds taken for light to propagate several kilometers. The beams will thus see the medium as frozen and

Figure 23



Cross-talk-free transmission. Simulated cross-talk matrices for OAM modes $\ell \in [0, 4]$ (right) and eigenmodes (left) with insets showing the intensity of the beams. The eigenmodes are unchanged and remain orthogonal, whereas the OAM modes scatter into each other. Turbulence results shown are for $D/r_0 = 2$ with a total path length of 100 m and a beam waist parameter for the OAM beams of $w_0 = 6.67$ mm.

remain robust for a sufficient period of time to transmit information. Investigations on similar modes have shown that they perform better than adaptive optics solutions [51]. The more challenging limitation is the amount of time needed to probe the channel, construct the channel matrix, and then use it to calculate the eigenmodes. This presents a significant but not insurmountable engineering challenge. Channel tomographies can be performed rapidly using the technique of modal decomposition [82]. Devices such as digital holograms on DMDs, diffractive optical elements, or metasurfaces could also allow for rapid or single-shot projective measurements, especially if used in combination with fast photodiodes to quickly probe the channel. This is already helped by the existence of techniques that rapidly measure the atmosphere and its effects on optical beams [83]. This problem also lends itself to a machine learning approach, where training predictive networks on previous measurements may allow for a system to anticipate the evolution of the eigenmodes as the channel itself is dynamically changing. Rapid probing and measurement of complex channels is not unique to the application of eigenmodes and it will assuredly benefit from knowledge generated in and spur progress in these related fields.

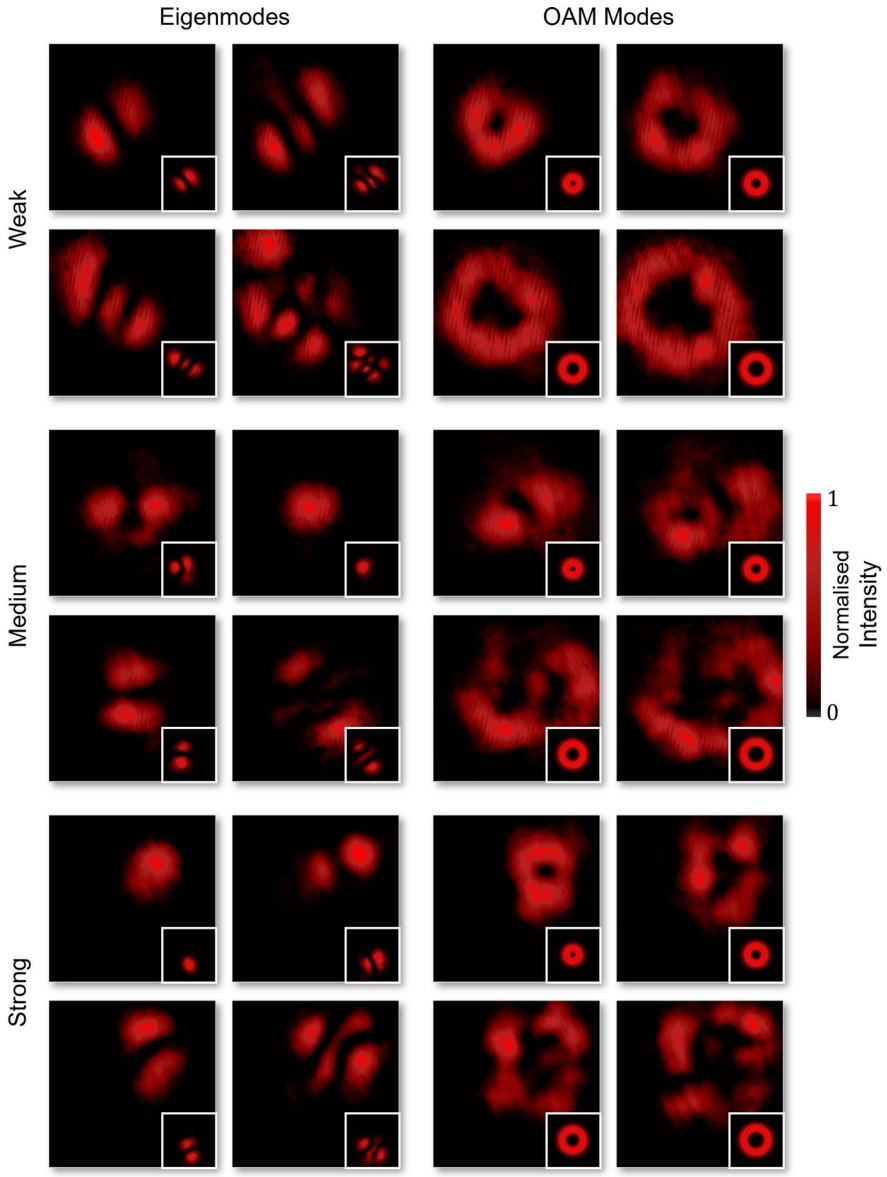
10. EXTENSION TO OTHER MEDIA AND REGIMES

Thus far, we have concentrated on the application of digital tools to the propagation of classical light through atmospheric turbulence, but they may be transformed beyond turbulence to other complex media, beyond classical to quantum, and beyond fundamental studies to applications. We show how the tutorial can be extrapolated using topical complex light in complex media examples as shown in Fig. 25 [85–90].

10.1. General Complex Light in Random Media

Turbulence can be considered a particular example of a random medium, with its stochastic nature described by some statistics and the strength of the perturbation given by a correlation length, r_0, as detailed in the previous sections. The impact on the propagating structured light is given by the dimensionless parameter D/r_0, with larger values corresponding to higher expected level of optical distortion. We can generalize this to arbitrary random media by replacing r_0 by an equivalent correlation length, l_0, defined as the (transverse) distance traveled for the phase changes to become uncorrelated. Just such an example is shown in Fig. 26. Here a normal distribution

Figure 24

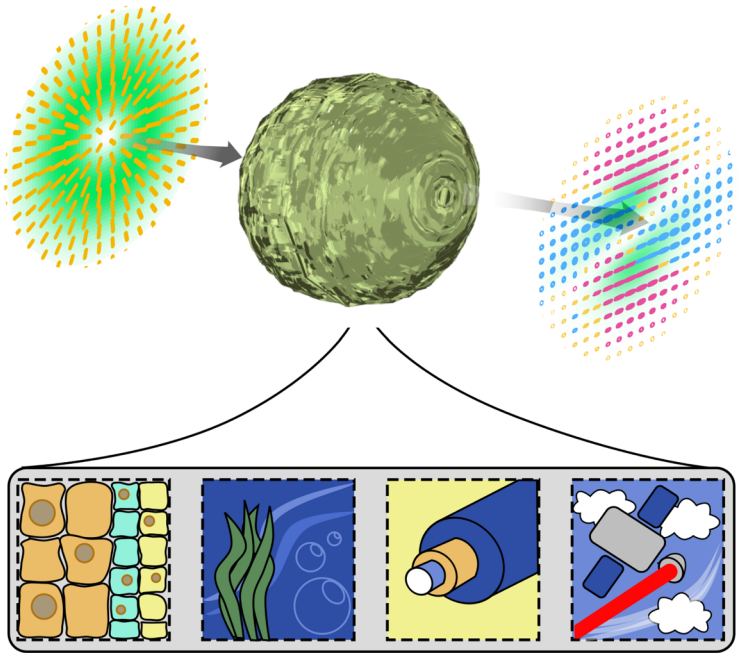


Experimental eigenmodes. In the left column we see the measured intensities of the eigenmodes of turbulence after propagating through the experimental setup. The results show eigenmodes of weak, medium, and strong turbulence. In the right column we see the measured intensities of OAM modes after propagating through the same experimental setup with the same turbulence phase screens for comparison. The insets show the initial input mode. Weak turbulence was characterized by $\sigma_R^2 = 0.5$ and $r_0 = 1.8$ mm, medium turbulence by $\sigma_R^2 = 1$ and $r_0 = 1.2$ mm and strong turbulence by $\sigma_R^2 = 1.5$ and $r_0 = 0.91$ mm.

is used for the statistics, a common model for general random processes, from which random phases are drawn, illustrated as colors, e.g., red, purple, and blue for phases ϕ_1, ϕ_2, and ϕ_3. The three random phase panels show increasing perturbation strength, with examples for $D/l_0 = 2$, 3, and 10.

The notion of a correlation length can also be extended to the light, to account for arbitrary complex light forms beyond the eigenmode examples already given. One such definition might be the average distance between the points in the beam cross section

Figure 25



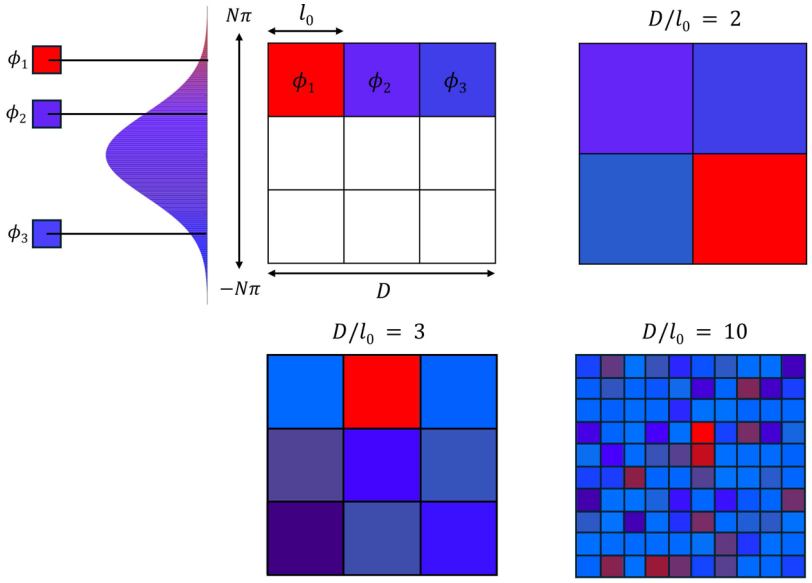
Extension to complex media. The tutorial's content can be extended beyond just free-space optics to other forms of complex media, including turbid (scattering media), underwater paths and optical fibre. The tutorial lends itself not only to the digital implementation of the medium but also arbitrary complex light, shown here as vectorial light passing through a complex medium and emerging distorted.

that has a phase difference of $\pi/2$, motivated by the fact that this is half way between completely in phase and completely out of phase [91]. Let us call this distance η. It has recently been shown that the ratio of the two correlation lengths, η/l_0, defines the modal scattering behavior of complex light in random complex media [92]. The implication is that the digital approaches outlined in this tutorial can immediately be translated to other random media and arbitrary structured light. When the medium and the beam are digitally prepared, complete control over η/l_0 is achieved and, hence, the outcomes can be understood in a more generalized sense. For instance, consider the example of a scattering medium. Although real scattering media are readily available and, thus, experiments are easy to realize [93–95], a digital approach would aid reproducibility and make the strength of the scattering more controllable.

10.2. Underwater Wireless Optical Communication

The study of light's propagation through underwater channels is closely related to the phenomenon of atmospheric turbulence. It has seen a surge of interest in recent years, driven by the need for greater communication speeds and data transfer rates, especially with the imminent development and implementation of 6G wireless networks [96,97]. Currently, underwater communications are dominated by the use of acoustic waves, which are able to propagate hundreds of kilometers with relatively low attenuation [98]. However, acoustic waves have a limited data transfer rates (of the order of kilobits per second) and high latency, limiting the surrounding infrastructure and technologies which have far greater speeds [99]. It is here where optical wavelengths have shown promise, with the ability to reach gigabit per second speeds in free space and in some atmospheric demonstrations [100]. However, optical wavelengths are not ideal for underwater propagation as they experience high attenuation even

Figure 26



Correlation lengths in random media. The tutorial's methodology of generating digital turbulence can be extended to other forms of complex media. Such digitization only requires knowledge of the medium's statistics and the notion of a correlation length. Here it is illustrated with Gaussian statistics to create random phase masks that have a phase range of $\phi \in \{-N\pi, N\pi\}$ and a phase correlation length of l_0 over an aperture of diameter D. The strength of the perturbation is given as D/l_0, in direct analogy with D/r_0 for turbulence.

over several meters and are severely affected by refractive index distortions in the medium [101]. It is clear already that acoustic wave communications systems will be an integral part of underwater wireless communication channels for the foreseeable future, but they can be supplemented over short distances with optical systems to great effect. Such applications include communications with and between manned and unmanned underwater vehicles, seafloor sensors, and submarines and could possibly be implemented to facilitate communications between submerged vehicles/sensors and aerial targets such as drones or aircraft [102].

There are several factors that hinder the implementation of optical wavelengths in underwater channels. The most prominent is absorption by the medium itself and by suspended particles. The molecular vibrations of water absorb strongly in the near-infrared and infrared regions of the electromagnetic spectrum while electron transitions absorb highly in the ultraviolet region. This leaves a limited optical wavelength range of about 400–540 nm with minimal absorption [103]. As with atmospheric turbulence, underwater channels also experience distortions in the form of temperature-induced refractive index fluctuations. Temperature fluctuations in underwater channels follow different statistical properties to that of atmospheric turbulence, mainly due to waters higher viscosity and density when compared with air. In addition, refractive index fluctuations are also induced by variations in the concentration of dissolved salts, which locally change the density of the medium [104,105]. Both temperature and salinity need to be considered when modeling underwater optical turbulence. The final major factor is scattering. In addition to suspended particulates, most underwater channels coincide with active ecosystems, inhabited by lifeforms of various sizes and properties ranging from the macroscopic (e.g., fish, crustaceans, and seaweed) to the microscopic (e.g., bacteria and plankton). While macroscopic

organisms will not necessarily be a constant hindrance on the time scales of interest in communication, microscopic organism, in addition to suspend inorganic particulates, will be constant cause of scattering, and due to the presence of chlorophyll in organisms such as phytoplankton, will also cause significant absorption in the blue and red regions of the visible spectrum [106].

Studies have looked at successfully implementing many of the traditional encoding schemes developed for FSOCs. These include the use of wavelength division multiplexing [107] and multiple-input multiple-output (MIMO) systems for space division multiplexing, with multiple transmitters and receivers [108]. The literature for spatial modes in underwater applications is sparse when compared with that for atmospheric turbulence. The successful multiplexing of OAM modes for underwater wireless optical communication has reached data transfer rates of 40 Gbit/s over 1.2 m [109] and multiple degrees of freedom have been combined, including wavelength, OAM, and polarization to achieve a 10 Gbit/s data transfer speed over 2.96 m [110].

Few strides have been made in manipulating the spatial degree of freedom to compensate for the losses in the underwater channel. Numerical routines have been implemented at the beam generation stage to compensate for the channel's distortion [111], while specially tailored Bessel–Gaussian beams have been utilized for more robust transport through underwater channels when compared to regular Gaussian beams [112]. Recent work has shown that the properties of metasurfaces can also be leveraged to efficiently shape light to improve focusing for more robust transport at multiple wavelengths achieving data transfer speed of up to 20 Gbit/s [113].

There remains significant room for advancement not only in our understanding of underwater turbulence and attenuation, but also in our ability to overcome its deleterious effects. The tools provided in this tutorial provide an excellent starting point to simulate and investigate this phenomenon. Statistical quantities, namely the power spectral density, for the refractive index fluctuations in water have different analytical expressions when compared with that of the atmosphere, however, it can be used with the same phase screen generation techniques detailed in this tutorial, allowing for a numerical or controlled, benchtop experimental simulation of an underwater channel. There are several spectra that can be used, depending on the particular type of application or conditions one wishes to simulate. Currently, the most common makes use of the Nikishov model which take into account the effects of both temperature and salinity [114]. Alternative spectra include the Li spectrum, which make provisions for unstable stratification in ocean layers [115] and the oceanic turbulence optical power spectrum which includes the average temperature, average salinity, and wavelength of the light used [116]. To make use of these spectra for phase screens, one need only swap out the Kolmogorov spectrum for atmospheric turbulence in the expressions here. In addition, if the attenuation factors for the particular environment and wavelengths are known, they can also be implemented numerically after measurements have been done or incorporated into the SLM encoding with the complex amplitude modulation scheme. Digital approaches will also allow for investigations into channels of considerable length (due to the Fresnel scaling procedure detailed here), which has significant benefit over current studies which have used water tanks with propagation lengths of only a 1–3 m [109,110,113].

Underwater wireless optical communication remains a vital area of research with important applications in the near future. The use of structured light in this field is still in its infancy, with many aspects still to investigate and uncover. We believe this tutorial provides all the necessary experimental tools to begin more in-depth and robust research into the benefits and pitfalls of structured light in this burgeoning field.

10.3. Machine Learning

Atmospheric turbulence is a severe optical aberration with a highly complex spatial structure that evolves rapidly over time. Compensating for and overcoming this distortion presents a significant practical challenge requiring one to probe or measure the distortion and compute corrections within a very short window of time and still allow for the transfer of information. Despite this, several computational techniques have shown the ability to mitigate some of the deleterious effects caused by a turbulent atmosphere. In the context of structured light in free space, these include the use of the Shack–Hartman algorithm paired with adaptive optics to measure and post-correct for the distortion [117–119] and the use of iterative numerical routines such as the Gerchberg–Saxton algorithm to perform phase retrieval and correction [120]. These approaches are, however, limited to correcting for the phase aberrations and cannot compensate fully for the amplitude perturbations present in transmitted modes. This then leaves the door open for more powerful computational tools which can successfully identify distorted modes or compensate for real-world atmospheric turbulence.

The ability of machine learning to efficiently and reliably recognize and classify images has highlighted it as a promising tool to overcome current limitations in FSOC with structured modes. Machine learning tools were used in some of the first demonstrations of the efficacy of OAM for FSOC. This includes communication over 3 km in Vienna with an average error of $\approx 1.7\%$ [13] and communications over 143 km in the Canary Islands with an average error rate of $\approx 8.33\%$ [121]. These demonstrations made use of an unsupervised learning approach known as self-organized maps. Here the network starts out with a finite number of connected but randomly distributed neurons in a high-dimensional space. Specified regions in this space are assigned to possible properties of the input data. The neurons are trained on sample input data and neurons are moved closer toward or further away from the specified regions such that neurons closer to the specified regions will activate when the input data have properties that are closely related to the properties that have been assigned to the region. After many iterations, one observes clumps of neurons in each of these specified regions leading to a map of self-organized neurons. One may then feed this network real data and classify them rapidly depending on which neurons in the network activate. These networks were initially used as they are easy to train and implement but require significant computational time and resources if one needs to resolve finer details and features.

Since these initial demonstrations, more sophisticated forms of machine learning have been developed. The most prominent of which for FSOC is deep learning (DL). Deep neural networks (DNNs) are functions that map some input $\mathbf{x}$ to some output $\mathbf{y}$. The function itself consists of a finite number of linear mappings W_i followed by a nonlinear function f_i such that the final process follows the relation

$$\mathbf{y} = f_N(\cdots f_2(f_1(\mathbf{x}^T W_1)W_2)\cdots W_N). \tag{10.1}$$

These generally take the form of the multilayer perceptron (MLP) architecture which encodes each pair of mapping functions W_i and f_i into a layer of nodes (also called perceptrons) and then maps the output of each perceptron in the ith layer to the inputs of the perceptrons in the $i+1$th layer. These models have not been used in this form for structured light detection and compensation but have been shown to improve the quality of imaging in astronomical observations through turbulence [122,123], correcting aberrations for the Hubble Space Telescope [124] and to improve the implementation of a high-pass filter for FSOC [125]. MLPs may have large numbers of perceptrons in each layer and can be upward of 10–20 layers deep leading to a large number of connections. This makes them very difficult to train each as perceptron's

weight needs to be carefully tuned and, once trained, the perceptrons are only sensitive to features in the input data if they occur consistently in the same place. This lack of spatial equivalence means MLPs on their own struggle with image recognition and computer vision tasks and makes them unsuitable as is for use with structured modes.

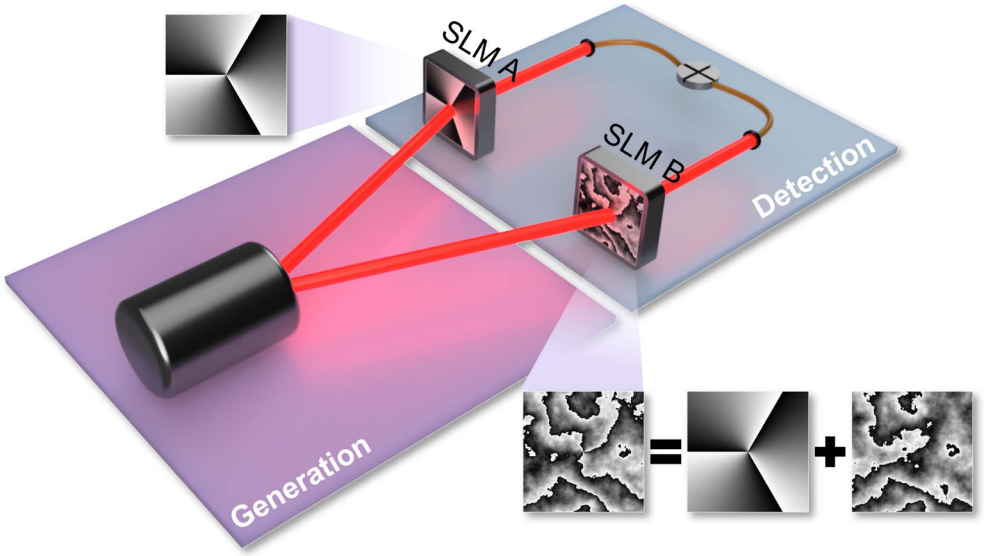
The issues with DNNs like MLPs have largely been overcome with the introduction of convolutional neural networks (CNNs). These have a similar architecture to that of MLPs, but precede the perceptron layers with what are known as convolutional layers. The convolutional layers do not interface with the elements of the input data individually and instead convolve the input signal with a kernel. This allows the network to identify features and properties of the input data regardless of their location and is thus a more effective tool for image recognition and classification. CNNs may have multiple convolutional layers to check for various features and can follow these with just one or multiple perceptron layers. They have been used with great effect in nonstructured light applications such as wavefront sensing [126,127], telescope correction [128], adaptive optics [129], and channel monitoring [130]. CNNs have shown great success in identifying and demultiplexing OAM modes that been distorted by turbulence [131–133] enabling effective adaptive demodulation for various encoding schemes using structured light [134,135] and allowing for the compensation and correction of aberration in perturbed OAM modes [136–138]. Despite the immense interest, many of these schemes are yet to be tested in real-world FSOC links.

This tutorial provides all necessary tools one needs to accurately simulate turbulence and in so doing allows one to develop authentic training data to provide current and burgeoning machine learning algorithms. In addition, it also allows one to construct numerical and experimental simulators which one may use to test the effectiveness of the developed machine learning models. The use of machine learning extends even to other complex media such as underwater channels [139] and allows for the compensation of other degrees of freedom in structured light such as the polarization [140] which can also be extended and simulated using the approaches detailed in this tutorial.

10.4. Quantum Implementation

The tutorial's content are immediately applicable to the quantum realm, and indeed almost all studies that exploit quantum structured light do so with a digital implementation [141,142]. A highly simplified version of such a quantum experiment is shown in Fig. 27, highlighting the salient differences between quantum and classical. In the classical scenarios outlined thus far in the tutorial, the structured light is created by SLMs, passed through a digital version of the medium, and then detected. In the quantum realm there are some differences. Let us assume that we are dealing with two entangled photons, one sent to SLM A and the other to SLM B. The spatial structure of each mode is usually determined by the measurement process, i.e., what modes were "measured" on the two SLMs. For instance, if the SLMs were programmed for OAM then the entanglement would be expressed in the OAM basis, if measure for HG modes, then the entanglement is expressed in the HG basis. By selecting a mode to measure, it is as if this mode was created at the source and is therefore the mode under consideration in the tests. This is called post-selecting in the measurement process. Each SLM can also be encoded with the perturbation, for instance, turbulence. But now one has several options for implementation. If only one SLM is encoded with the medium then it appears as if only one photon passed through the medium; this is called a one-sided quantum channel. An example of a real-world case would be quantum key distribution, where one photon is measured in the sender's lab (Alice) and the other is sent across the channel to the receiver, Bob. Here only one photon experiences the noisy medium. The programming of the medium on the SLM follows

Figure 27



Quantum implementation. So far in this tutorial, the spatial structure on the classical mode was imprinted at the generation step, the light was passed through a medium implemented digitally with SLMs, and then finally detected with cameras. In the quantum realm with two entangled photons, as depicted here, it is common to post-select a particular spatial structure in the detection step, as if the detection is the generation. The digital implementation of the medium can be implemented in several ways: both photons can experience the same medium, each can experience conditions different to the other, or just one can experience the medium, all programmed on the two SLMs, one for each photon. The photons are measured by single photon detectors and counted in coincidence. The illustration shows the post-selection of OAM modes (of topological order three) in a one-sided turbulence channel.

exactly the same rules as before. The spatial modes on each SLM determine what is tested, perhaps OAM on both photons (as if they both were OAM photons) or maybe OAM on one and HG on the other. It is also possible to have the medium digitally implemented for both photons by programming both SLMs. The two could have the same conditions (correlated media) or not (uncorrelated or partially correlated). This is called a two-sided channel, and an example might be two-photon imaging through turbid systems. The point is that all the content of the tutorial can be applied directly to the quantum realm, arguably with even more flexibility than in the classical case.

Exactly such tools have already been applied successfully in prior studies. For example, one-sided turbulence has been demonstrated experimentally in the laboratory with polarization qubits [143], with OAM quantum states to show entanglement decay [144,145], and later extended to high-dimensional quantum states with OAM [146]. Although digital approaches with SLMs are usually associated with spatial modes, they can also be used to mimic polarization channels [147] and momentum channels [148] for quantum states. The same digital approach can be used in the undoing of the channel, for adaptive optics compensation. This has been done for turbulence [149] and other complex media [88–90], where the correction on photon A can fix the error of photon B by virtue of entanglement [150]. Finally, the digital tools presented here can be used to blend classical and quantum studies of turbulence [145].

11. DISCUSSION AND CONCLUDING REMARKS

Throughout this tutorial we have concentrated on the core toolkit of creating structured light and accurately simulating atmospheric turbulence. We anticipate that the tutorial will aid the fast extrapolation to other turbulence models, e.g., the von Karman and Tartatrskii models which are relevant in situation when the inner and outer scales of atmospheric turbulence must be considered [30,32] and the oceanic power spectrum which is important for modeling similar effects in salt water [114,151,152]. Similarly, the tools outlined here can be deployed to study various families of structured light in turbulence, e.g., including Bessel–Gaussian [14,153–163], HG [164–166], LG [167–171], and Ince–Gaussian [172] beams. Because the atmosphere is not birefringent, the simulation of the medium will also hold true for vectorial light, a topic of immense interest to the community [173–179]. Where these tools might also play an important role as a test bed for various forms of correction of the effects of turbulence, including modal diversity [180], traditional adaptive optics [117–119], simulating beam broadening and energy variations [66,181,182], vectorial adaptive tools [183], iterative routines [120], and even DL models [136]. The search for completely invariant forms of light to atmospheric turbulence [15,18,52] likewise hinges on such tools. These topics and future studies should benefit from this tutorial. The tutorial will also be useful to the studies that do not seek modal invariance but rather modal change, for instance, selecting structured light that will be highly sensitive to the medium under study and utilizing it as a probe, where modal scattering is used to infer information on the medium, a topic that is receiving significant attention of late [184].

In conclusion, in this tutorial we have outlined how to get started with digitally implementing structured light in atmospheric turbulence, both as numerical studies (digitally on a computer) and experimental realization (on digital devices). Laboratory test beds are crucial to unravel the complexities of the topic prior to real-world studies, and to test real-world instrumentation under controlled conditions. We have unpacked the basic theory, how to numerically simulated turbulence, how to create computer-generated holograms that simulate atmospheric conditions, and shown how to test whether the implementation is correct or not. We covered points seldom outlined in technical works, including how to execute time-varying turbulence and how to include long-path and strong turbulence correctly. Throughout the tutorial we have highlighted the approach with the use of structured light, touching on popular families and their digital creation. We hope it will be useful to both newcomers to the field and experts alike.

APPENDIX A. DERIVATION OF THE KOLMOGOROV POWER LAWS

The atmosphere is a highly turbulent medium and, thus, very difficult to describe using typical fluid mechanics approaches such as the Navier–Stokes equations. In 1941, Andrey Kolmogorov proposed a statistical treatment of fluids with high Reynolds numbers. The Reynolds number is used to quantify and characterize how turbulent a particular medium is and is given by [183]

$$Re = \frac{\rho v L}{\mu} \tag{A1}$$

where ρ is the density of the liquid, v is the speed of the fluid flow, L is the characteristic linear dimension, and μ is the viscosity. Media with low Reynolds numbers are considered close to smooth/laminar flows and media with high Reynolds numbers are considered turbulent flow.

In Kolmogorov's theory of turbulence, proposed by Andrey Kolmogorov in the 1940s [25], we study the flow of energy through the system. We begin at *outer length scale*

L_0, at which energy is being injected into the system, driving the turbulent flow. The exact value of L_0 corresponds to the length at which two points in the system are still correlated. At any scale larger than L_0, the system will appear to have laminar flow. The injected energy cascades down to smaller length scales in the form of turbulent eddies. Here, the particles that make up the medium lose energy due to inelastic collisions with other particles, leading to the formation of smaller and smaller eddies and the downward energy cascade. This energy loss will be captured by the energy dissipation rate ϵ. This process continues until the *inner length scale* l_0 is reached. At this scale the kinetic energy of the particles has become small enough that the viscosity μ of the medium becomes significant. The viscosity quantifies the effects of the friction created by the attractive forces between molecules in the medium. Thus, in this regime, the potential energy between the molecules becomes comparable to their kinetic energies. Since we are dealing with a fluid medium, we use the kinematic viscosity $\eta = \mu/\rho$, which normalizes out the volume and mass considerations to capture only the effect of the attractive and repulsive forces. The range of length scales between L_0 and l_0 is known as the *inertial subrange*.

We can quantify the *inner length scale* l_0, also known as the *Kolmogorov micro-scale*, through the use of dimensional analysis. At this scale, the flow is dictated by two parameters: the energy dissipation rate ϵ, quantifying the behavior due to the kinetic energy, and the kinematic viscosity η, quantifying the behavior due to the potential energy. The units of both are $[\epsilon] = \mathrm{m}^2\,\mathrm{s}^{-3}$ and $[\eta] = \mathrm{m}^2\,\mathrm{s}^{-1}$. Combining both of these allows us to find a characteristic length scale l_0 and a characteristic time scale t_0, given by

$$l_0 = \left(\frac{\eta^3}{\epsilon}\right)^{\frac{1}{4}}, \tag{A2}$$

$$t_0 = \left(\frac{\eta}{\epsilon}\right)^{\frac{1}{2}}. \tag{A3}$$

The Kolmogorov model is powerful as it allows us to quantify the fluctuation in the medium within the inertial subrange. We know that the energy changes as we move from larger eddies to smaller eddies. Thus, we can relate the velocity fluctuations δv to the length scale of the eddies we are interested in l. From these two quantities, we can determine a time scale at which these fluctuations occur,

$$\tau = \frac{l}{\delta v}. \tag{A4}$$

The turbulent kinetic energy E, the kinetic energy per unit mass in the medium must by definition be given by

$$E = \frac{1}{2}\delta v^2. \tag{A5}$$

As the same kinds of particles are colliding at all length scale, we may assume that the loss in kinetic energy due the inelastic collisions is the same at all length scales and, thus, the energy dissipation rate is constant within our inertial subrange. By combining Eqs. (A4) and (A5), we then have

$$\begin{aligned} \epsilon &= \frac{E}{\tau} \\ &= \frac{1}{2}\delta v^2 \frac{\delta v}{l} \\ &= \frac{1}{2}\frac{\delta v^3}{l} \\ \Rightarrow \delta v &= C_v l^{\frac{1}{3}},\ C_v = (2\epsilon)^{\frac{1}{3}}, \end{aligned} \tag{A6}$$

where C_v is known as the velocity structure constant. We may also examine the behavior of the fluctuations outside the inertial subrange. For scales above the outer scale L_0, we see laminar flow and so $\delta v = 0$ for $l \gg L_0$. For scales below the inner scale/micro-scale l_0, we consider an arbitrary length scale l_1 such that $l_0 > l_1$. The larger l_0 is compared with l_1, the more time it takes for energy to cascade down from l_0 to l_1. Consequently, there is lower energy and smaller velocity fluctuations. Thus, we see an inverse relationship between l_0 and δv in this regime. We may then adapt this into Eq. (A6) as follows:

$$\delta v = C_v l_0^{-\frac{2}{3}} l, \tag{A7}$$

where the extra factor of $l^{\frac{2}{3}}$ is brought in to keep everything dimensionally consistent. We therefore have

$$\delta v = \begin{cases} C_v l^{\frac{1}{3}}, & \text{for } L_0 > l > l_0, \\ C_v l_0^{-\frac{2}{3}} l, & \text{for } l_0 > l. \end{cases} \tag{A8}$$

We are also able to find relationships between the length scales and the energy. We must first define a spatial frequency or wavenumber such that $\kappa = l^{-1}$. We then define an energy spectrum $g(\kappa)$ such that the turbulent kinetic energy in the range from κ to $\kappa + \mathrm{d}\kappa$ is given by

$$E = g(\kappa)\,\mathrm{d}\kappa. \tag{A9}$$

Combining this with Eqs. (A5) and (A8) gives us the following:

$$\begin{aligned} g(\kappa)\mathrm{d}\kappa &= C_v \kappa^{-\frac{2}{3}} \\ \Rightarrow g(\kappa) &= C_v \kappa^{-\frac{5}{3}}. \end{aligned} \tag{A10}$$

From this, we are able to easily calculate the energy at any particular length scale.

APPENDIX B. STATISTICS FOR RANDOM PROCESSES

The theory of turbulence presented in this work is one based off of statistics. Using the assumptions proposed by Kolomogorov and others, we are able to derive analytical expressions for several statistical quantities that describe the behavior of atmospheric turbulence. In this appendix, we give a brief overview of the various statistical quantities of interest which we use to construct our model of turbulence. For a more in-depth discussion of these quantities, we refer the reader to Chapter 2 of Ref. [32].

We look at a random process described by $x(t)$. The variable x is measured n number of times at times $t_1, \ldots, t_n$. We assume that the process is wide-sense stationary meaning that the mean and the moments of the variable remain constant for the duration of our measurements. This is a reasonable assumption to make for refractive index fluctuations in turbulence as the mean value of the refractive index does not change even over long time scales and the moments such as the variance remain constant as long as we look at time scales comparable with the Greenwood frequency. The assumption of a wide-sense stationary process results in many of the statistical quantities being invariant to time translation and thus we may write them as in terms of $\tau = t_2 - t_1$.

We may define the expectation value of a random process $x(t)$ (also sometimes called the ensemble average) as follows:

$$\langle x(t) \rangle = m(t) = \int_{-\infty}^{\infty} x p_x(x, t)\,\mathrm{d}x, \tag{B1}$$

where $p_x(x, t)$ the probability distribution function of the process $x(t)$. The variance of the process is given by

$$\sigma_x^2(t) = \langle x^2(t) \rangle - m^2(t) = \int_{-\infty}^{\infty} (x(t) - m(t))^2 p_x(x, t)\,\mathrm{d}x. \tag{B2}$$

These relations are true for any process, however, they remain constant for a wise-sense stationary process.

The autocorrelation function (or just correlation function) for a stationary random process $x(t)$ is given by

$$\begin{aligned} &\mathcal{R}_x(t_1, t_2) = \langle x(t_1)x(t_2)\rangle = \int_{-\infty}^{\infty}\int_{-\infty}^{\infty} x_1 x_2 p_x(x_1, x_2; t_1, t_2)\,\mathrm{d}x_1\,\mathrm{d}x_2, \\ &\Rightarrow \mathcal{R}_x(\tau) = \langle x(t)x(t+\tau)\rangle. \end{aligned} \tag{B3}$$

The autocovariance function (or simply covariance function) is given by

$$\begin{aligned} \mathcal{B}_x(t_1, t_2) &= \langle (x(t_1) - \langle x(t_1)\rangle)(x(t_2) - \langle x(t_2)\rangle)\rangle \\ &= \langle x(t_1)x(t_2)\rangle - m(t_1)m(t_2) \\ \mathcal{B}_x(\tau) &= \langle x(t)x(t+\tau)\rangle - m(0)m(\tau) \\ &= \langle x(t)x(t+\tau)\rangle - m^2 \\ &= \mathcal{R}_x(\tau) - m^2. \end{aligned} \tag{B4}$$

Turbulence is usually modeled as a small fluctuation from a mean value. We may model such a random process as

$$x(t) = m(t) + \delta x(t), \tag{B5}$$

where $x(t)$ is the variable of interest, $m(t)$ is the mean of that variable. and $\delta x(t)$ is how far that variable deviates from the mean at a time t. We define a special function for this process known as a structure function which is given by

$$\begin{aligned} \mathcal{D}_x(t_1, t_2) &= \langle [x(t_1) - x(t_2)]^2\rangle \\ &= [m(t_1) - m(t_2)]^2 - \langle [\delta x(t_1) - \delta x(t_2)]\rangle. \end{aligned} \tag{B6}$$

We assume that for our process, the mean does not significantly change over time and so we have $m(t_1) \approx m(t_2)$ for small enough time period and so the structure function simplifies to

$$\mathcal{D}_x(t_1, t_2) \approx \langle [\delta x(t_1) - \delta x_1(t_2)]^2\rangle. \tag{B7}$$

The moments of a stationary process are constant over time by definition and so we can easily relate the structure function and the covariance function as follows:

$$\begin{aligned} \mathcal{D}_x(\tau) &= \langle [x(t+\tau) - x(t)]^2\rangle \\ &= \langle x^2(t+\tau)\rangle - 2\langle x(t+\tau)x(t)\rangle + \langle x^2(t)\rangle \\ &= \langle x^2(t)\rangle - 2\langle x(t+\tau)x(t)\rangle + \langle x^2(t)\rangle \\ &= 2\langle x^2(t)\rangle - 2\langle x(t+\tau)x(t)\rangle \\ &= 2\left[\langle x^2(t)\rangle - m^2 - \langle x(t+\tau)x(t)\rangle + m^2\right] \\ &= 2\left[\mathcal{B}(0) - \mathcal{B}(\tau)\right]. \end{aligned} \tag{B8}$$

It is sometimes useful to examine a process in the frequency domain instead of the time domain. To do this we define a quantity known as the power spectral density,

which is the Fourier transform of the covariance function,

$$\Phi_x(\omega) = \int \mathcal{B}_x(t) e^{2\pi i \omega t}\, \mathrm{d}t, \Leftrightarrow \mathcal{B}_x(t) = \int \Phi_x(\omega) e^{-2\pi i \omega t}\, \mathrm{d}\omega.$$

If the random variable of interest is real valued, then both the covariance function $\mathcal{B}_x(t)$ and the power spectral density $\Phi_x(\omega)$ are real and we may write,

$$\Phi_x(\omega) = \int \mathcal{B}_x(t) \cos(2\pi\omega t)\, \mathrm{d}t. \tag{B9}$$

This is the case with turbulence as the refractive index fluctuations are real-valued quantities.

Using Eq. (B8), we may relate the structure function to the power spectral density as follows:

$$\mathcal{D}_x(t) = 2 \int \Phi(\omega)(1 - \cos(2\pi\omega t))\, \mathrm{d}\omega. \tag{B10}$$

ACKNOWLEDGMENTS

Cade Peters would like to thank Asher Klug for all of his guidance and assistance when first introducing him to this field, Dr. Giacomo Sorelli for his insights and for making us aware of the method of generating time-varying phase screens, and Professor Enrique "Kiko" Galvez for his insights and helpful suggestions.

DISCLOSURES

The authors declare no conflicts of interest.

DATA AVAILABILITY

Data underlying the results presented in this paper are not publicly available at this time but may be obtained from the authors upon reasonable request. MATLAB code for the generation of the Fourier and Noll phase screens, time-varying phase screens, Zernike polynomials, DMD holograms, SLM holograms, and angular spectrum propagation may be found at Ref. [185].

REFERENCES

1. A. Forbes, M. de Oliveira, and M. R. Dennis, "Structured light," Nat. Photonics **15**, 253–262 (2021).
2. A. Forbes, "Structured light: tailored for purpose," Opt. Photon. News **31**, 24–31 (2020).
3. C. Rosales-Guzmán, B. Ndagano, and A. Forbes, "A review of complex vector light fields and their applications," J. Opt. **20**, 123001 (2018).
4. S. Franke-Arnold, "30 years of orbital angular momentum of light," Nat. Rev. Phys. **4**, 361 (2022).
5. E. Otte, C. Alpmann, and C. Denz, "Polarization singularity explosions in tailored light fields," Laser Photonics Rev. **12**, 1700200 (2018).
6. C. He, Y. Shen, and A. Forbes, "Towards higher-dimensional structured light," Light: Sci. Appl. **11**, 205 (2022).
7. Y. Shen, X. Wang, Z. Xie, *et al.*, "Optical vortices 30 years on: OAM manipulation from topological charge to multiple singularities," Light: Sci. Appl. **8**, 90 (2019).
8. M. Padgett and R. Bowman, "Tweezers with a twist," Nat. Photonics **5**, 343–348 (2011).

9. A. Trichili, M. A. Cox, B. S. Ooi, *et al.*, "Roadmap to free space optics," J. Opt. Soc. Am. B **37**, A184–A201 (2020).
10. A. E. Willner, K. Pang, H. Song, *et al.*, "Orbital angular momentum of light for communications," Appl. Phys. Rev. **8**, 041312 (2021).
11. B. Ndagano, I. Nape, M. A. Cox, *et al.*, "Creation and detection of vector vortex modes for classical and quantum communication," J. Lightwave Technol. **36**, 292–301 (2017).
12. M. Erhard, R. Fickler, M. Krenn, *et al.*, "Twisted photons: new quantum perspectives in high dimensions," Light: Sci. Appl. **7**, 17146 (2018).
13. M. Krenn, R. Fickler, M. Fink, *et al.*, "Communication with spatially modulated light through turbulent air across Vienna," New J. Phys. **16**, 113028 (2014).
14. N. Mphuthi, L. Gailele, I. Litvin, *et al.*, "Free-space optical communication link with shape-invariant orbital angular momentum Bessel beams," Appl. Opt. **58**, 4258–4264 (2019).
15. C. Peters, M. Cox, A. Drozdov, *et al.*, "The invariance and distortion of vectorial light across a real-world free space link," Appl. Phys. Lett. **123**(2), 021103 (2023).
16. A. Sit, F. Bouchard, R. Fickler, *et al.*, "High-dimensional intracity quantum cryptography with structured photons," Optica **4**, 1006–1010 (2017).
17. M. P. Lavery, C. Peuntinger, K. Günthner, *et al.*, "Free-space propagation of high-dimensional structured optical fields in an urban environment," Sci. Adv. **3**, e1700552 (2017).
18. I. Nape, K. Singh, A. Klug, *et al.*, "Revealing the invariance of vectorial structured light in complex media," Nat. Photonics **16**, 538–546 (2022).
19. Z. Zhu, M. Janasik, A. Fyffe, *et al.*, "Compensation-free high-dimensional free-space optical communication using turbulence-resilient vector beams," Nat. Commun. **12**, 1666 (2021).
20. O. Keskin, L. Jolissaint, and C. Bradley, "Hot-air optical turbulence generator for the testing of adaptive optics systems: principles and characterization," Appl. Opt. **45**, 4888–4897 (2006).
21. N. A. Ferlic, S. Avramov-Zamurovic, O. O'Malley, *et al.*, "Randomness of optical turbulence generated by Rayleigh–Bénard convection using intensity statistics," J. Opt. Soc. Am. A **41**, B85–B94 (2024).
22. S. Scholes, R. Kara, J. Pinnell, *et al.*, "Structured light with digital micromirror devices: a guide to best practice," Opt. Eng. **59**, 041202 (2019).
23. L. Perumal and A. Forbes, "Broadband structured light using digital micro-mirror devices (DMDs): a tutorial," J. Opt. **25**, 074003 (2023).
24. Y. Yang, A. Forbes, and L. Cao, "A review of liquid crystal spatial light modulators: devices and applications," Opto-Electronic Science **2**, 230026 (2023).
25. A. N. Kolmogorov, "The local structure of turbulence in incompressible viscous fluid for very large Reynolds numbers," Proc. R. Soc. Lond. A **434**, 9–13 (1991).
26. A. N. Kolmogorov, "Dissipation of energy in the locally isotropic turbulence," Proc. R. Soc. Lond. A **434**, 15–17 (1991).
27. A. Oboukhov, "Structure of the temperature field in turbulent flows," Isv. Geogr. Geophys. Ser. **13**, 58–69 (1949).
28. S. Corrsin, "On the spectrum of isotropic temperature fluctuations in an isotropic turbulence," J. Appl. Phys. **22**, 469–473 (1951).
29. L. F. Richardson, *Weather Prediction by Numerical Process* (University Press, 1922).
30. V. I. Tatarskii, "The effects of the turbulent atmosphere on wave propagation," *Jerusalem: Israel Program for Scientific Translations, 1971* (1971).
31. J. C. Owens, "Optical refractive index of air: dependence on pressure, temperature and composition," Appl. Opt. **6**, 51–59 (1967).

32. L. C. Andrews, *Laser Beam Propagation through Random Media*, 2nd ed. (SPIE Press, 2005).
33. T.-i. Wang, G. Ochs, and S. Clifford, "A saturation-resistant optical scintillometer to measure C_n^2," J. Opt. Soc. Am. **68**, 334–338 (1978).
34. L. C. Andrews and M. K. Beason, *Laser Beam Propagation in Random Media: New and Advanced Topics* (SPIE, 2023).
35. J. Kaimal, *Atmospheric Boundary Layer Flows: Their Structure and Measurement*, Vol. 289 (Oxford University Press, 1994).
36. L. C. Andrews, R. L. Phillips, and C. Y. Hopen, *Laser Beam Scintillation with Applications*, Vol. 99 (SPIE Press, 2001).
37. D. L. Fried, "Optical resolution through a randomly inhomogeneous medium for very long and very short exposures," J. Opt. Soc. Am. **56**, 1372–1379 (1966).
38. D. P. Greenwood, "Bandwidth specification for adaptive optics systems," J. Opt. Soc. Am. **67**, 390–393 (1977).
39. M. A. Cox, N. Mphuthi, I. Nape, *et al.*, "Structured light in turbulence," IEEE J. Sel. Top. Quantum Electron. **27**, 1–21 (2020).
40. L. C. Andrews, R. L. Phillips, C. Y. Hopen, *et al.*, "Theory of optical scintillation," J. Opt. Soc. Am. A **16**, 1417–1429 (1999).
41. S. Avramov-Zamurovic, N. A. Ferlic, and K. P. Judd, "The impact of underwater optical turbulence generated by Rayleigh-Bénard convection on structured laser light propagation," SSRN (2024).
42. A. Tunick, "Statistical analysis of optical turbulence intensity over a 2.33 km propagation path," Opt. Express **15**, 3619–3628 (2007).
43. M. Beason, G. Potvin, D. Sprung, *et al.*, "Comparative analysis of C_n^2 estimation methods for sonic anemometer data," Appl. Opt. **63**, E94–E106 (2024).
44. J. A. Anguita, M. A. Neifeld, and B. V. Vasic, "Turbulence-induced channel crosstalk in an orbital angular momentum-multiplexed free-space optical link," Appl. Opt. **47**, 2414–2429 (2008).
45. L. Zhang, F. Shen, B. Lan, *et al.*, "Mode-dependent crosstalk and detection probability of orbital angular momentum of optical vortex beam through atmospheric turbulence," J. Opt. **22**, 075607 (2020).
46. B. Rodenburg, M. P. Lavery, M. Malik, *et al.*, "Influence of atmospheric turbulence on states of light carrying orbital angular momentum," arXiv (2012).
47. M. Malik, M. O'Sullivan, B. Rodenburg, *et al.*, "Influence of atmospheric turbulence on optical communications using orbital angular momentum for encoding," Opt. Express **20**, 13195–13200 (2012).
48. G. A. Tyler and R. W. Boyd, "Influence of atmospheric turbulence on the propagation of quantum states of light carrying orbital angular momentum," Opt. Lett. **34**, 142–144 (2009).
49. C. Paterson, "Atmospheric turbulence and orbital angular momentum of single photons for optical communication," Phys. Rev. Lett. **94**, 153901 (2005).
50. C. Gopaul and R. Andrews, "The effect of atmospheric turbulence on entangled orbital angular momentum states," New J. Phys. **9**, 94 (2007).
51. D. Bachmann, M. Isoard, V. Shatokhin, *et al.*, "Highly-transmitting modes of light in dynamic atmospheric turbulence," arXiv (2022).
52. A. Klug, C. Peters, and A. Forbes, "Robust structured light in atmospheric turbulence," Adv. Photonics **5**, 016006 (2023).
53. Y. Wang, P. Zhang, H. Zhao, *et al.*, "Investigation of urban low-altitude long-range atmospheric links for FSO coherent communication," Opt. Commun. **574**, 131068 (2025).
54. S. Bendersky, N. S. Kopeika, and N. Blaunstein, "Atmospheric optical turbulence over land in middle east coastal environments: prediction modeling and measurements," Appl. Opt. **43**, 4070–4079 (2004).

55. F. S. Vetelino, B. Clare, K. Corbett, *et al.*, "Characterizing the propagation path in moderate to strong optical turbulence," Appl. Opt. **45**, 3534–3543 (2006).
56. S. Gladysz, M. Segel, C. Eisele, *et al.*, "Estimation of turbulence strength, anisotropy, outer scale and spectral slope from an led array," in *Laser Communication and Propagation through the Atmosphere and Oceans IV*, Vol. 9614 (SPIE, 2015), p. 961402.
57. R. Pernice, A. Andò, M. Cardinale, *et al.*, "Indoor free space optics link under the weak turbulence regime: measurements and model validation," IET Commun. **9**, 62–70 (2015).
58. C. Burgess and C. Westgate, "Experimental validation of a phase screen propagation model for nanosecond laser pulses travelling through turbulent atmospheres," in *Technologies for Optical Countermeasures XIV*, Vol. 10435 (SPIE, 2017), pp. 52–63.
59. D. J. Griffiths, *Introduction to Electrodynamics* (Pearson, 2013).
60. J. A. Fleck, J. Morris, and M. Feit, "Time-dependent propagation of high energy laser beams through the atmosphere," Appl. Phys. **10**, 129–160 (1976).
61. V. P. Lukin and B. V. Fortes, *Adaptive Beaming and Imaging in the Turbulent Atmosphere*, Vol. 109 (SPIE Press, 2002).
62. J. D. Schmidt, *Numerical Simulation of Optical Wave Propagation with Examples in Matlab* (SPIE, 2010).
63. J. Martin and S. M. Flatté, "Intensity images and statistics from numerical simulation of wave propagation in 3-D random media," Appl. Opt. **27**, 2111–2126 (1988).
64. R. Rao, "Statistics of the fractal structure and phase singularity of a plane light wave propagation in atmospheric turbulence," Appl. Opt. **47**, 269–276 (2008).
65. J. P. Bos and M. C. Roggemann, "Technique for simulating anisoplanatic image formation over long horizontal paths," Opt. Eng. **51**, 101704 (2012).
66. X. Xiao, D. G. Voelz, I. Toselli, *et al.*, "Gaussian beam propagation in anisotropic turbulence along horizontal links: theory, simulation, and laboratory implementation," Appl. Opt. **55**, 4079–4084 (2016).
67. R. C. Hardie, J. D. Power, D. A. LeMaster, *et al.*, "Simulation of anisoplanatic imaging through optical turbulence using numerical wave propagation with new validation analysis," Opt. Eng. **56**, 1 (2017).
68. X. Xiao and D. Voelz, "On-axis probability density function and fade behavior of partially coherent beams propagating through turbulence," Appl. Opt. **48**, 167–175 (2009).
69. G. Sorelli, N. Leonhard, V. N. Shatokhin, *et al.*, "Entanglement protection of high-dimensional states by adaptive optics," New J. Phys. **21**, 023003 (2019).
70. D. Bachmann, M. Isoard, V. Shatokhin, *et al.*, "Highly transmitting modes of light in dynamic atmospheric turbulence," Phys. Rev. Lett. **130**, 073801 (2023).
71. J. D. Phillips, M. E. Goda, and J. Schmidt, "Atmospheric turbulence simulation using liquid crystal spatial light modulators," in *Advanced Wavefront Control: Methods, Devices, and Applications III*, Vol. 5894 (SPIE, 2005), pp. 57–67.
72. E. M. Johansson and D. T. Gavel, "Simulation of stellar speckle imaging," in *Amplitude and Intensity Spatial Interferometry II*, Vol. 2200 (SPIE, 1994), pp. 372–383.
73. J. D. Schmidt, *Numerical Simulation of Optical Wave Propagation With Examples in MATLAB*, 1st ed. (SPIE Press, 2010).
74. R. G. Lane, A. Glindemann, and J. C. Dainty, "Simulation of a Kolmogorov phase screen," Waves in Random Media **2**, 209–224 (1992).
75. B. J. Herman and L. A. Strugala, "Method for inclusion of low-frequency contributions in numerical representation of atmospheric turbulence," in *Propagation of High-Energy Laser Beams Through the Earth's Atmosphere*, Vol. 1221 P. B.

Ulrich and L. E. Wilson, eds., International Society for Optics and Photonics (SPIE, 1990), pp. 183–192.
76. R. J. Noll, "Zernike polynomials and atmospheric turbulence," J. Opt. Soc. Am. **66**, 207–211 (1976).
77. N. A. Roddier, "Atmospheric wavefront simulation using Zernike polynomials," Opt. Eng. **29**, 1174–1180 (1990).
78. M. Born and E. Wolf, *Principles of Optics: Electromagnetic Theory of Propagation, Interference and Diffraction of Light* (Elsevier, 2013).
79. V. Arrizón, U. Ruiz, R. Carrada, *et al.*, "Pixelated phase computer holograms for the accurate encoding of scalar complex fields," J. Opt. Soc. Am. A **24**, 3500–3507 (2007).
80. B. Rodenburg, M. Mirhosseini, M. Malik, *et al.*, "Simulating thick atmospheric turbulence in the lab with application to orbital angular momentum communication," New J. Phys. **16**, 033020 (2014).
81. Y. Ren, H. Huang, G. Xie, *et al.*, "Atmospheric turbulence effects on the performance of a free space optical link employing orbital angular momentum multiplexing," Opt. Lett. **38**, 4062–4065 (2013).
82. J. Pinnell, I. Nape, B. Sephton, *et al.*, "Modal analysis of structured light with spatial light modulators: a practical tutorial," J. Opt. Soc. Am. A **37**, C146–C160 (2020).
83. D. Lechner, A. Zepp, M. Eichhorn, *et al.*, "Adaptable Shack–Hartmann wavefront sensor with diffractive lenslet arrays to mitigate the effects of scintillation," Opt. Express **28**, 36188–36205 (2020).
84. J. D. Barchers, D. L. Fried, and D. J. Link, "Evaluation of the performance of Hartmann sensors in strong scintillation," Appl. Opt. **41**, 1012–1021 (2002).
85. L. G. Wright, F. O. Wu, D. N. Christodoulides, *et al.*, "Physics of highly multimode nonlinear optical systems," Nat. Phys. **18**, 1018–1030 (2022).
86. H. Cao, A. P. Mosk, and S. Rotter, "Shaping the propagation of light in complex media," Nat. Phys. **18**, 994–1007 (2022).
87. J. Bertolotti and O. Katz, "Imaging in complex media," Nat. Phys. **18**, 1008–1017 (2022).
88. S. Gigan, O. Katz, H. B. De Aguiar, *et al.*, "Roadmap on wavefront shaping and deep imaging in complex media," J. Phys. Photonics **4**, 042501 (2022).
89. O. Lib and Y. Bromberg, "Quantum light in complex media and its applications," Nat. Phys. **18**, 986–993 (2022).
90. B. Courme, P. Cameron, D. Faccio, *et al.*, "Manipulation and certification of high-dimensional entanglement through a scattering medium," PRX Quantum **4**, 010308 (2023).
91. N. D. Leonhard, V. N. Shatokhin, and A. Buchleitner, "Universal entanglement decay of photonic-orbital-angular-momentum qubit states in atmospheric turbulence," Phys. Rev. A **91**, 012345 (2015).
92. D. Bachmann, A. Klug, M. Isoard, *et al.*, "Universal crosstalk of twisted light in random media," Phys. Rev. Lett. **132**, 063801 (2024).
93. A. Z. Genack, Y. Huang, A. Maor, *et al.*, "Velocities of transmission eigenchannels and diffusion," Nat. Commun. **15**, 2606 (2024).
94. H. Zhang, Q. Wang, M. Fink, *et al.*, "Optimizing multi-user indoor sound communications with acoustic reconfigurable metasurfaces," Nat. Commun. **15**, 1270 (2024).
95. R. Ma, K. H. Luo, S. Pokharel, *et al.*, "Orbital-angular-momentum-dependent speckles for spatial mode sorting and demultiplexing," Optica **11**, 595–605 (2024).
96. N. Chi, Y. Zhou, Y. Wei, *et al.*, "Visible light communication in 6G: advances, challenges, and prospects," IEEE Veh. Technol. Mag. **15**, 93–102 (2020).

97. M. Z. Chowdhury, M. Shahjalal, M. K. Hasan, *et al.*, "The role of optical wireless communication technologies in 5G/6G and IoT solutions: prospects, directions, and challenges," Appl. Sci. **9**, 4367 (2019).
98. D. B. Kilfoyle and A. B. Baggeroer, "The state of the art in underwater acoustic telemetry," IEEE J. Oceanic Eng. **25**, 4–27 (2000).
99. H. Kaushal and G. Kaddoum, "Underwater optical wireless communication," IEEE Access **4**, 1518–1547 (2016).
100. Y. Li, W. Mo, S. Zhu, *et al.*, "Optical fiber communication conference," in *National Fiber Optic Engineers Conference* (2017).
101. Y. Baykal, Y. Ata, and M. C. Gökçe, "Underwater turbulence, its effects on optical wireless communication and imaging: a review," Opt. Laser Technol. **156**, 108624 (2022).
102. L.-K. Chen, Y. Shao, and Y. Di, "Underwater and water-air optical wireless communication," J. Lightwave Technol. **40**, 1440–1452 (2022).
103. R. C. Smith and K. S. Baker, "Optical properties of the clearest natural waters (200–800 nm)," Appl. Opt. **20**, 177–184 (1981).
104. S. A. Thorpe, *The Turbulent Ocean* (Cambridge University Press, 2005).
105. S. A. Thorpe, *An Introduction to Ocean Turbulence*, Vol. 10 (Cambridge University Press Cambridge, 2007).
106. W. Liu, D. Zou, Z. Xu, *et al.*, "Non-line-of-sight scattering channel modeling for underwater optical wireless communication," in *2015 IEEE International Conference on Cyber Technology in Automation, Control, and Intelligent Systems (CYBER)* (IEEE, 2015), pp. 1265–1268.
107. F. Hu, G. Li, P. Zou, *et al.*, "20.09-Gbit/s underwater WDM-VLC transmission based on a single Si/GaAs-substrate multichromatic LED array chip," in *2020 Optical fiber communications conference and exhibition (OFC)* (IEEE, 2020), pp. 1–3.
108. M. V. Jamali, P. Nabavi, and J. A. Salehi, "MIMO underwater visible light communications: comprehensive channel study, performance analysis, and multiple-symbol detection," IEEE Trans. Veh. Technol. **67**, 8223–8237 (2018).
109. Y. Ren, L. Li, Z. Wang, *et al.*, "Orbital angular momentum-based space division multiplexing for high-capacity underwater optical communications," Sci. Rep. **6**, 33306 (2016).
110. J. Baghdady, K. Miller, J. Kelly, *et al.*, "Underwater optical communication link using wavelength division multiplexing, polarization division multiplexing and orbital angular momentum multiplexing," in *Frontiers in Optics* (Optica Publishing Group, 2016), pp. FTh4E–4.
111. J. Nie, L. Tian, F. Zhang, *et al.*, "Parametric hologram optimization for enhanced underwater wireless optical communication," Opt. Express **30**, 23967–23977 (2022).
112. M. Khodadadi Karahroudi, S. A. Moosavi, A. Mobashery, *et al.*, "Performance evaluation of perfect optical vortices transmission in an underwater optical communication system," Appl. Opt. **57**, 9148–9154 (2018).
113. J. Hu, Z. Guo, J. Shi, *et al.*, "A metasurface-based full-color circular auto-focusing Airy beam transmitter for stable high-speed underwater wireless optical communications," Nat. Commun. **15**, 2944 (2024).
114. V. V. Nikishov and V. I. Nikishov, "Spectrum of turbulent fluctuations of the sea-water refraction index," Inter. J. Fluid Mech. Res. **27**, 82–98 (2000).
115. Y. Li, Y. Zhang, and Y. Zhu, "Oceanic spectrum of unstable stratification turbulence with outer scale and scintillation index of Gaussian-beam wave," Opt. Express **27**, 7656–7672 (2019).

116. J.-R. Yao, M. Elamassie, and O. Korotkova, "Spatial power spectrum of natural water turbulence with any average temperature, salinity concentration, and light wavelength," J. Opt. Soc. Am. A **37**, 1614–1621 (2020).
117. R. K. Tyson, "Bit-error rate for free-space adaptive optics laser communications," J. Opt. Soc. Am. A **19**, 753–758 (2002).
118. S. Zhao, J. Leach, L. Gong, *et al.*, "Aberration corrections for free-space optical communications in atmosphere turbulence using orbital angular momentum states," Opt. Express **20**, 452–461 (2012).
119. Y. Ren, G. Xie, H. Huang, *et al.*, "Adaptive-optics-based simultaneous pre-and post-turbulence compensation of multiple orbital-angular-momentum beams in a bidirectional free-space optical link," Optica **1**, 376–382 (2014).
120. M. Li, Y. Li, and J. Han, "Gerchberg–Saxton algorithm based phase correction in optical wireless communication," Phys. Commun. **25**, 323–327 (2017).
121. M. Krenn, J. Handsteiner, M. Fink, *et al.*, "Twisted light transmission over 143 km," Proc. Natl. Acad. Sci. **113**, 13648–13653 (2016).
122. J. R. P. Angel, P. Wizinowich, M. Lloyd-Hart, *et al.*, "Adaptive optics for array telescopes using neural-network techniques," Nature **348**, 221–224 (1990).
123. D. Sandler, T. Barrett, D. Palmer, *et al.*, "Use of a neural network to control an adaptive optics system for an astronomical telescope," Nature **351**, 300–302 (1991).
124. T. K. Barrett and D. G. Sandler, "Artificial neural network for the determination of Hubble Space Telescope aberration from stellar images," Appl. Opt. **32**, 1720–1727 (1993).
125. Y. Gao, Q.-W. Jing, M.-F. Liu, *et al.*, "Deep learning-assisted high-pass-filter-based fixed-threshold decision for free-space optical communications," in *Photonics*, Vol. 11 (MDPI, 2024), p. 599.
126. S. W. Paine and J. R. Fienup, "Machine learning for improved image-based wavefront sensing," Opt. Lett. **43**, 1235–1238 (2018).
127. Y. Xu, D. He, Q. Wang, *et al.*, "An improved method of measuring wavefront aberration based on image with machine learning in free space optical communication," Sensors **19**, 3665 (2019).
128. K. Huang, T. Hu, J. Cai, *et al.*, "Artificial intelligence in astronomical optical telescopes: present status and future perspectives," Universe **10**, 210 (2024).
129. Y. Guo, L. Zhong, L. Min, *et al.*, "Adaptive optics based on machine learning: a review," Opto-Electron. Adv. **5**, 200082 (2022).
130. M. A. Esmail, W. S. Saif, A. M. Ragheb, *et al.*, "Free space optic channel monitoring using machine learning," Opt. Express **29**, 10967–10981 (2021).
131. T. Doster and A. T. Watnik, "Machine learning approach to OAM beam demultiplexing via convolutional neural networks," Appl. Opt. **56**, 3386–3396 (2017).
132. R. Sun, L. Guo, M. Cheng, *et al.*, "Identifying orbital angular momentum modes in turbulence with high accuracy via machine learning," J. Opt. **21**, 075703 (2019).
133. S. Cai, Z. Li, Z. Zhong, *et al.*, "Deep-learning-based recognition of composite vortex beams through long-distance and moderate-to-strong atmospheric turbulence," Phys. Rev. A **110**, 013508 (2024).
134. J. Li, M. Zhang, D. Wang, *et al.*, "Joint atmospheric turbulence detection and adaptive demodulation technique using the CNN for the OAM-FSO communication," Opt. Express **26**, 10494–10508 (2018).
135. Q. Tian, Z. Li, K. Hu, *et al.*, "Turbo-coded 16-ary OAM shift keying FSO communication system combining the CNN-based adaptive demodulator," Opt. Express **26**, 27849–27864 (2018).

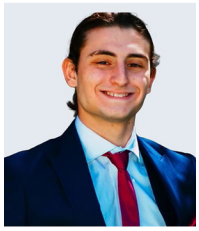
136. J. Liu, P. Wang, X. Zhang, *et al.*, "Deep learning based atmospheric turbulence compensation for orbital angular momentum beam distortion and communication," Opt. Express **27**, 16671–16688 (2019).
137. Y. Zhai, S. Fu, J. Zhang, *et al.*, "Turbulence aberration correction for vector vortex beams using deep neural networks on experimental data," Opt. Express **28**, 7515–7527 (2020).
138. W. Xiong, P. Wang, M. Cheng, *et al.*, "Convolutional neural network based atmospheric turbulence compensation for optical orbital angular momentum multiplexing," J. Lightwave Technol. **38**, 1712–1721 (2020).
139. X. Cui, X. Yin, H. Chang, *et al.*, "Experimental study of machine-learning-based orbital angular momentum shift keying decoders in optical underwater channels," Opt. Commun. **452**, 116–123 (2019).
140. D. Pierangeli, G. Volpe, and C. Conti, "Deep learning enabled transmission of full-Stokes polarization images through complex media," Laser Photonics Rev. **18**, 2400626 (2024).
141. I. Nape, B. Sephton, P. Ornelas, *et al.*, "Quantum structured light in high dimensions," APL Photonics **8**(5), 051101 (2023).
142. A. Forbes and I. Nape, "Quantum mechanics with patterns of light: progress in high dimensional and multidimensional entanglement with structured light," AVS Quantum Science **1**, 011701 (2019).
143. S. P. Phehlukwayo, M. L. Umuhire, Y. Ismail, *et al.*, "Influence of coincidence detection of a biphoton state through free-space atmospheric turbulence using a partially spatially coherent pump," Phys. Rev. A **102**, 033732 (2020).
144. A. H. Ibrahim, F. S. Roux, M. McLaren, *et al.*, "Orbital-angular-momentum entanglement in turbulence," Phys. Rev. A **88**, 012312 (2013).
145. B. Ndagano, B. Perez-Garcia, F. S. Roux, *et al.*, "Characterizing quantum channels with non-separable states of classical light," Nat. Phys. **13**, 397–402 (2017).
146. Y. Zhang, S. Prabhakar, A. H. Ibrahim, *et al.*, "Experimentally observed decay of high-dimensional entanglement through turbulence," Phys. Rev. A **94**, 032310 (2016).
147. G. B. Lemos, J. De Almeida, S. Walborn, *et al.*, "Characterization of a spatial light modulator as a polarization quantum channel," Phys. Rev. A **89**, 042119 (2014).
148. B. Marques, A. Matoso, W. Pimenta, *et al.*, "Experimental simulation of decoherence in photonics qudits," Sci. Rep. **5**, 16049 (2015).
149. J. Zhao, Y. Zhou, B. Braverman, *et al.*, "Performance of real-time adaptive optics compensation in a turbulent channel with high-dimensional spatial-mode encoding," Opt. Express **28**, 15376–15391 (2020).
150. N. H. Valencia, S. Goel, W. McCutcheon, *et al.*, "Unscrambling entanglement through a complex medium," Nat. Phys. **16**, 1112–1116 (2020).
151. B. Ruddick and J. Turner, "The vertical length scale of double-diffusive intrusions," Deep-Sea Res., Part A **26**, 903–913 (1979).
152. O. Korotkova, "Light propagation in a turbulent ocean," in *Progress in Optics*, Vol. 64 (Elsevier, 2019), pp. 1–43.
153. N. Mphuthi, R. Botha, and A. Forbes, "Are Bessel beams resilient to aberrations and turbulence?" J. Opt. Soc. Am. A **35**, 1021–1027 (2018).
154. I. P. Lukin, "Mean intensity of vortex Bessel beams propagating in turbulent atmosphere," Appl. Opt. **53**, 3287–3293 (2014).
155. C. Bao-Suan and P. Ji-Xiong, "Propagation of Gauss–Bessel beams in turbulent atmosphere," Chin. Phys. B **18**, 1033–1039 (2009).
156. K. Zhu, G. Zhou, X. Li, *et al.*, "Propagation of Bessel–Gaussian beams with optical vortices in turbulent atmosphere," Opt. Express **16**, 21315–21320 (2008).

157. W. Nelson, J. Palastro, C. Davis, *et al.*, "Propagation of Bessel and Airy beams through atmospheric turbulence," J. Opt. Soc. Am. A **31**, 603–609 (2014).
158. N. Ahmed, Z. Zhao, L. Li, *et al.*, "Mode-division-multiplexing of multiple Bessel-Gaussian beams carrying orbital-angular-momentum for obstruction-tolerant free-space optical and millimetre-wave communication links," Sci. Rep. **6**, 22082 (2016).
159. M. Cheng, L. Guo, J. Li, *et al.*, "Channel capacity of the OAM-based free-space optical communication links with Bessel–Gauss beams in turbulent ocean," IEEE Photonics J. **8**, 1–11 (2016).
160. T. Doster and A. T. Watnik, "Laguerre–Gauss and Bessel–Gauss beams propagation through turbulence: analysis of channel efficiency," Appl. Opt. **55**, 10239–10246 (2016).
161. R. J. Watkins, K. Dai, G. White, *et al.*, "Experimental probing of turbulence using a continuous spectrum of asymmetric OAM beams," Opt. Express **28**, 924–935 (2020).
162. C. Vetter, R. Steinkopf, K. Bergner, *et al.*, "Realization of free-space long-distance self-healing Bessel beams," Laser Photonics Rev. **13**, 1900103 (2019).
163. Y. Yuan, T. Lei, Z. Li, *et al.*, "Beam wander relieved orbital angular momentum communication in turbulent atmosphere using Bessel beams," Sci. Rep. **7**, 1–7 (2017).
164. M. A. Cox, L. Maqondo, R. Kara, *et al.*, "The resilience of Hermite– and Laguerre–Gaussian modes in turbulence," J. Lightwave Technol. **37**, 3911–3917 (2019).
165. B. Ndagano, N. Mphuthi, G. Milione, *et al.*, "Comparing mode-crosstalk and mode-dependent loss of laterally displaced orbital angular momentum and Hermite–Gaussian modes for free-space optical communication," Opt. Lett. **42**, 4175 (2017).
166. S. Restuccia, D. Giovannini, G. Gibson, *et al.*, "Comparing the information capacity of Laguerre–Gaussian and Hermite–Gaussian modal sets in a finite-aperture system," Opt. Express **24**, 27127 (2016).
167. A. Trichili, C. Rosales-Guzmán, A. Dudley, *et al.*, "Optical communication beyond orbital angular momentum," Sci. Rep. **6**, 27674 (2016).
168. N. Zhao, X. Li, G. Li, *et al.*, "Capacity limits of spatially multiplexed free-space communication," Nat. Photonics **9**, 822–826 (2015).
169. Y. Zhou, M. Mirhosseini, S. Oliver, *et al.*, "Using all transverse degrees of freedom in quantum communications based on a generic mode sorter," Opt. Express **27**, 10383–10394 (2019).
170. G. Xie, Y. Ren, Y. Yan, *et al.*, "Experimental demonstration of a 200-Gbit/s free-space optical link by multiplexing Laguerre–Gaussian beams with different radial indices," Opt. Lett. **41**, 3447–3450 (2016).
171. L. Li, G. Xie, Y. Yan, *et al.*, "Power loss mitigation of orbital-angular-momentum-multiplexed free-space optical links using nonzero radial index Laguerre–Gaussian beams," J. Opt. Soc. Am. B **34**, 1–6 (2017).
172. W. Cheng, J. W. Haus, and Q. Zhan, "Propagation of vector vortex beams through a turbulent atmosphere," Opt. Express **17**, 17829–17836 (2009).
173. Y. Cai, Q. Lin, H. T. Eyyuboğlu, *et al.*, "Average irradiance and polarization properties of a radially or azimuthally polarized beam in a turbulent atmosphere," Opt. Express **16**, 7665–7673 (2008).
174. M. A. Cox, C. Rosales-Guzmán, M. P. J. Lavery, *et al.*, "On the resilience of scalar and vector vortex modes in turbulence," Opt. Express **24**, 18105–18113 (2016).

175. P. Lochab, P. Senthilkumaran, and K. Khare, "Designer vector beams maintaining a robust intensity profile on propagation through turbulence," Phys. Rev. A **98**, 023831 (2018).
176. Y. Gu, O. Korotkova, and G. Gbur, "Scintillation of nonuniformly polarized beams in atmospheric turbulence," Opt. Lett. **34**, 2261–2263 (2009).
177. P. Ji-Xiong, W. Tao, L. Hui-Chuan, *et al.*, "Propagation of cylindrical vector beams in a turbulent atmosphere," Chin. Phys. B **19**, 089201 (2010).
178. T. Wang and J. Pu, "Propagation of non-uniformly polarized beams in a turbulent atmosphere," Opt. Commun. **281**, 3617–3622 (2008).
179. M. A. Cox, L. Cheng, C. Rosales-Guzmán, *et al.*, "Modal diversity for robust free-space optical communications," Phys. Rev. Appl. **10**, 024020 (2018).
180. V. Banakh and I. Smalikho, "Fluctuations of energy density of short-pulse optical radiation in the turbulent atmosphere," Opt. Express **22**, 22285–22297 (2014).
181. M. W. Hyde IV, S. Basu, and J. D. Schmidt, "Two-dimensional simulation of optical wave propagation through atmospheric turbulence," Opt. Lett. **40**, 233–236 (2015).
182. C. He, J. Wang, Q. Hu, *et al.*, "Vectorial adaptive optics: correction of polarization and phase," in *Adaptive Optics and Wavefront Control for Biological Systems VI*, Vol. 11248 (International Society for Optics and Photonics, 2020), p. 1124808.
183. M. Cheng, W. Jiang, L. Guo, *et al.*, "Metrology with a twist: probing and sensing with vortex light," Light: Sci. Appl. **14**, 4 (2025).
184. O. Reynolds, "XXIX. an experimental investigation of the circumstances which determine whether the motion of water shall be direct or sinuous, and of the law of resistance in parallel channels," Phil. Trans. R. Soc. London **174**, 935–982 (1883).
185. C. R. Peters, "SLTurbulence," GitHub, (2024), https://github.com/CadeRPhysics/SLTurbulence.



Cade Ribeiro Peters joined the Structured Light Lab at the University of the Witwatersrand (South Africa) in 2022 as a Master's student. Staying to pursue a PhD in Physics, his research interests range from investigating the behavior of complex states of light in perturbing media and exploring the boundary between quantum and classical light.



Vasilios Cocotos is a Master's student at the University of the Witwatersrand (South Africa) with a background in astronomy and astrophysics, who transitioned into the field of optics. Their research focuses on atmospheric turbulence and advanced beam-shaping techniques, exploring the interaction of light with complex environments.



Andrew Forbes has at various times in his career found himself as teacher, janitor, secretary, receptionist, web-master, systems engineer, sales rep, manager, director, and sometimes a scientist. He is presently a Distinguished Professor within the School of Physics at the University of the Witwatersrand (South Africa) where in 2015 he established a new laboratory for structured light. He is active in promoting photonics in Africa, a founding member of the Photonics Initiative of South Africa, and initiator of South Africa's Quantum

Roadmap. He is a Fellow of SPIE, the OSA (now Optica), the SAIP, and an elected member of the Academy of Science of South Africa.